

DETERMINING AERODYNAMIC PROPERTIES OF
SPORTS BALLS IN SITU

By

JEFFREY RYAN KENSRUD

A thesis submitted in partial fulfillment of
the requirements for the degree of

MASTER OF SCIENCE IN MECHANICAL ENGINEERING

WASHINGTON STATE UNIVERSITY
Department of Mechanical and Materials Engineering

AUGUST 2010

To the Faculty of Washington State University:

The members of the Committee appointed to examine the thesis of JEFFREY RYAN

KENSRUD find it satisfactory and recommend that it be accepted.

Lloyd V Smith, Ph.D., Chair

Prashanta Dutta, Ph.D.

Konstantin Matveev, Ph.D.

ACKNOWLEDGMENT

I would like to thank Dr. Lloyd Smith and his Sports Science Laboratory for making this research possible. I would like to Dr. Prashanta Dutta for his insight and advice related to the fluids portion of my research. I would like to thank Dr. Konstantin Matveev for being on my committee. I would like to thank Gabe Boruff and WSU Baseball for the use of their pitching machine.

I would then like to thank my parents, especially my mom, for all her encouragement and support during my entire educational career. If it weren't for her I wouldn't have had this opportunity.

I would like to also thank my colleagues Warren Faber, Jason Martin, and Tim Graciano. Thanks to everyone in the lab, Andy, Peter, Anthony, Chris, and T.J. My experience in the lab will be remembered.

Thank you Bri for your patience and support.

DETERMINING AERODYNAMIC PROPERTIES OF SPORTS BALLS IN SITU

Abstract

by Jeffrey R. Kensrud, M.S.
Washington State University
August 2010

Chair: Lloyd V. Smith

Understanding the aerodynamic properties of the ball can lead to better predicting the path of a ball's flight. Two important factors in the ball's trajectory are the aerodynamic lift and drag. Lift and drag vary with the ball's geometry, roughness, and translational and rotational speed.

A numerical 3-D model was developed in Gambit and analyzed in Fluent. Results were inconsistent with experimental findings and determined unsuccessful.

Wind tunnels may have measurable differences with ball drag occurring in play. The following considers lift and drag measurements from a ball propelled through static air in a laboratory setting. Measurements of aerodynamic properties in situ were similar to those made in wind tunnels. Smooth spheres, for instance, had a 10% reduction in drag through a low Reynolds region, comparable to wind tunnel results.

Drag was observed for eight different ball types. Drag depended on the ball speed, rotation, roughness, and orientation. A so-called drag crisis was observed in some magnitude for all balls. A pronounced drag crisis was observed on a smooth sphere, golf ball, and flat seamed baseballs and softballs. As stitch height increased, drag increased. Orientation and rotation of the ball reduced the drag crisis.

Lift was measured on three types of baseballs. All three balls showed a similar bilinear increase in lift with increasing spin. Results here showed higher lift than previous work.

Scatter in measured lift and drag was larger for stitched balls than smooth or dimpled balls. Lift and drag were shown to be sensitive to seam height and orientation (which is difficult to control experimentally). This observed sensitivity may explain the disparity in lift and drag data found in literature.

Table of Contents

DETERMINING AERODYNAMIC PROPERTIES OF	i
SPORTS BALLS IN SITU	i
<i>ACKNOWLEDGMENT</i>	iii
Abstract	iv
Table of Contents	vi
<i>Dedication</i>	viii
List of Figures	ix
Chapter I – The Evolution and Flight of the Baseball	1
1.1 Section 1.1 – Introduction	1
Chapter II– Literature Review	4
2.1 Section 2.1 – Background: The Flight of the Baseball	4
2.2 Section 2.2 – Overview of Boundary Layer Behavior	5
2.3 Section 2.3 – Lift and drag studies on balls, spheres, and other objects	10
2.4 Section 2.4 – Reverse Magnus Effect	29
2.5 Section 2.5 – Numerical lift and drag analysis	31
2.6 Section 2.6 – Concluding Remarks	33
Chapter III – Numerical Determination of Lift and Drag	35
3.1 Section 3.1 – Numerical Model Introduction	35
3.2 Section 3.2 – Geometry and Meshing	35
3.3 Section 3.3 – Boundary Conditions and Solver	39
3.4 Section 3.4 – Numerical Results	41

Chapter IV – Experimental determination of lift and drag.....	45
4.1 Section 4.1 – Experimental Setup	45
4.2 Section 4.2 – Uncertainty in Measuring Speed and Displacement with Light Gates.....	56
4.3 Section 4.3 – Samples.....	65
4.4 Section 4.4 – Experimental procedures	67
4.5 Section 4.5 – Experimentally determining drag	67
4.6 Section 4.6 – Experimentally determining lift and angular velocity	69
4.7 Section 4.7 – Experimentally determining angular velocity of the ball.....	71
4.8 Section 4.8 – Drag results	73
4.9 Section 4.9 – Lift results	92
Chapter V – Summary	102
5.1 Section 5.1 – Summary.....	102
5.2 Section 5.2 – Future work.....	103
Appendix One.....	109

Dedication

-To Dad-

List of Figures

Figure 2.1 - Free body diagram of a translating and rotating sphere.	5
Figure 2.2 – Velocity distribution in the boundary layer over a flat plate.....	6
Figure 2.3 - Flow over a smooth cylinder: (a) $Re < 3 \times 10^5$, flow stays laminar in the boundary layer until 80° where it separates; (b) $3 \times 10^5 < Re < 3 \times 10^6$, flow separates at 80° becomes turbulent and reconnects before separating again at 120 degrees; (c) $3 \times 10^6 < Re$, flow is turbulent in the boundary layer on the front and stays turbulent until separating at 120°	8
Figure 2.4 – a) Flow over a smooth sphere; b) Flow over same smoother sphere with a trip wire placed on the front half of the surface. (7).....	10
Figure 2.5 - Flow over ball with Magnus effect.	11
Figure 2.6 - Flow around a cylinder rotating clockwise. Three images show cylinders rotating progressively faster with the upper image being the slowest and the lower image being the fastest (7).....	13
Figure 2.7 - Lateral deflection of a baseball, spinning about a vertical axis, when dropped across a horizontal windstream. These values are all for the same time interval, 0.6 sec, the time required for the ball to cross the stream. (11).....	14
Figure 2.8 - Graph showing that the observed lateral deflections are proportional to the square of the wind speed. (11).....	15
Figure 2.9 - Drag coefficient of the sphere as a function of Reynolds number taken from (12).....	17
Figure 2.10 - Data taken from wind tunnel and flight tests by Millikan and Klein.....	18

Figure 2.11 - CD curves while varying surface roughness of spheres.....	19
Figure 2.12 - Variation of the lateral force imbalance with orientation of the baseball ...	21
Figure 2.13 - Lift coefficient for a conventional golf ball. (17)	23
Figure 2.14 - Drag coefficient for a conventional golf ball. (17)	23
Figure 2.15 - Lift coefficient data comparing several data sets.....	24
Figure 2.16 – Drag coefficient of various pitches. Data suggests a drag crisis occurs with CD as low as 0.16.	26
Figure 2.17 - CL trend found in Nathan's experiment. 22 pitches were analyzed.	27
Figure 2.18 - Results for CL from various experiments. closed circles are from Nathan; open circles are from Watts and Ferrer; open triangles are from Briggs; open diamonds and squares re from Always two and four seam, respectfully; closed triangles are from Jinji (25); solid line is from parameterizations of Sawaicki, Hubbard, and Stronge (24); dashed is from (2.10).	28
Figure 2.19 - CL and CD reduced from PITCHf/x tracking system	29
Figure 2.20 - Flow propagation for Magnus effect and reverse Magnus effect.	30
Figure 2.21 - Lift coefficients for baseball with rifle spin. Various initial orientations are plotted.	33
Figure 3.1 - Geometry and mesh around NCAA baseball.....	36
Figure 3.2- Geometry of mesh zones.....	37
Figure 3.3 - Cross section of meshed zones.....	37
Figure 3.4 - Cross section of meshed baseball.....	38
Figure 3.5 – Sphere cross section of meshed zones (close up of ball).....	39
Figure 3.6 - Screen shot of viscous model in Fluent.....	41

Figure 3.7 - Particle path lines over a baseball traveling at 65 mph.	42
Figure 3.8 - Rear view of particle path lines over a baseball traveling at 50 mph with 200 radians/second angular velocity.	43
Figure 3.9 - Numerical model drag curves while varying the size of the outer boundary limit.	44
Figure 3.10 – Numerical model drag curve for smooth sphere.	45
Figure 4.1 - Light gates configuration inside the light box.	46
Figure 4.2 - Schematic of light box setup.	47
Figure 4.3 - 1st light box and pneumatic cannon.	48
Figure 4.4 – Baseball loaded into the polycarbonate sabot.	49
Figure 4.5 - Sabot placed in the cannon's barrel.	49
Figure 4.6 - Still frame shot of softball leaving the cannon at 90 mph.	50
Figure 4.7 - Side view of three wheeled pitching machine.	51
Figure 4.8 - Front view of the three wheeled pitching machine.	52
Figure 4.9 - Home Plate machine with control panel exposed.	53
Figure 4.10 - Home Plate circuit board.	54
Figure 4.11 - Schematic of experimental setup.	54
Figure 4.12 - Light boxes and wooden funnel.	55
Figure 4.13 - Scale mounted to front and aligned to the bottom of the box.	56
Figure 4.14 - Velocity repeatability test configuration.	57
Figure 4.15 - Light box configuration during vertical calibration.	58
Figure 4.16 - Light box in calibration setup (with coordinates).	59
Figure 4.17 - Light gate configuration for velocity uncertainty.	60

Figure 4.18 - Velocity repeatability between light boxes. 61

Figure 4.19 - Constant velocity and y location while changing x location. 62

Figure 4.20 - Constant x location and velocity, while changing y displacement. 63

Figure 4.21 - Constant x and y location while changing velocity. 63

Figure 4.22 - Constant velocity and y location while changing x location. Black bars show precision error (standard deviation). At least six samples were used in each data set. 64

Figure 4.23 - Constant x location and velocity, while changing y displacement. Black bars show precision error (standard deviation). At least six samples were used in each data set. 64

Figure 4.24 - Constant x and y location while changing velocity. Black bars show precision error (standard deviation). At two samples were used in each data set. 65

Figure 4.25 - Diagram showing the normal/4-seam (a) and parallel/2-seam (b) orientations. Black arrows indicate the airflow direction, white arrows indicate the ball rotation axis. 66

Figure 4.27 - Variation of angle of projection while pitching machine was in one fixed location. 70

Figure 4.28 - Image progression of a translating and rotating baseball through four frames. 73

Figure 4.29 - Local coordinates of all three dots on a baseball in flight (pixels). 73

Figure 4.30 – Acrylic contact juggling ball. Figure 4.31 - Rubber smooth stage juggling ball 74

Figure 4.32 - Smooth sphere drag curve with no rotation 75

Figure 4.33 - NCAA baseball	76
Figure 4.34 - NCAA baseball drag curve normalized with no rotation.....	76
Figure 4.35 - NCAA baseball drag curve with no rotation (vs. pitch speed)	77
Figure 4.36 - NCAA baseball with rotation normalized to spin factor.....	78
Figure 4.37 - MLB baseball.....	79
Figure 4.38 - Drag curve for MLB baseball	79
Figure 4.39 - MLB baseball drag curve with rotation.	80
Figure 4.40 - a) 11 inch circumference softball with raised stitches; b) 12 inch softball.	81
Figure 4.41 - Softball drag curve normalized	82
Figure 4.42 - Softball drag curve.	82
Figure 4.43 - Cricket ball	83
Figure 4.44 - Cricket ball drag curve normalized	84
Figure 4.45 - Cricket ball drag curve	84
Figure 4.46- Dimpled pitching machine ball	85
Figure 4.47 - Drag curve for dimpled pitching machine ball.	86
Figure 4.48 - Dimpled pitching machine ball drag curve with rotation.....	87
Figure 4.49 - Drag curve for all balls tested	89
Figure 4.50 - Comparison of balls with similar seam height to diameter ratio (raised seam).....	90
Figure 4.51 - Comparison of balls with similar seam height to diameter ratio (flat seam).	90
Figure 4.52 - Drag curve for rotating balls.	91
4.53 - Drag curve for a dimpled sphere with and without rotation.....	92

Figure 4.54 - Lift curve for NCAA in 2 seam and 4 seam orientations.....	94
Figure 4.55 - Lift curve for MLB baseballs.....	95
Figure 4.56 – Lift curve for dimpled pitching machine ball.....	96
Figure 4.57 - Lift curves for all balls tested.....	97
Figure 4.58 - Lift curves plotted against other experiments and research. Open triangles are from (21), closed triangles are from (23), and the solid line is the parameterization from (22).	98
Figure 4.59 – Scenario A: optimized trajectory for an MLB, NCAA, and 12 inch softball at 1200 rpm, 100 mph BBS.....	100
Figure 4.60 - Optimized trajectory for an MLB, NCAA, and 12 inch softball at 400 rpm, 120 mph BBS.....	100
Figure 4.61 – Scenario A: Lateral ball deflections. Pitch speed was 100 mph. Angular velocity was 500 rpm. Release angle was 0 degrees.	101
Figure 4.62 – Scenario B: Lateral pitched ball deflections. Pitch speed was 80 mph. Angular velocity was 500 rpm. Release angle was optimized such that each ball would cross home plate.....	101

List of Tables

Table 4.1 - Sample types and specifications.....	66
Table 4.2- Sample calculations showing iteration process to find <i>aL</i>	71

Chapter I – The Evolution and Flight of the Baseball

Section 1.1 – Introduction

For many citizens of the United States of America the game of baseball is more than watching a batter crush the ball into the outfield and slide safely into second; the game of baseball marked the beginning of the land of the free. The first sign of the game of baseball dates back to mid 1800's where the game was played with few rules and a baseball constructed out of rubber wrapped with strings covered by horsehide (1). Up until 1872, the game had few restrictions and the baseball itself varied among ball clubs. In 1872, a size restriction was placed on the ball confining it to be between 5 and 5.5 ounces, and 9.25 inches in circumference. This baseball, with its rubber core absorbed much of the energy delivered by the bat resulting in dull, short hits. To increase the livelihood of the ball, in 1910 (2) a cork core was implemented. Once implemented the number of 0.300 hitters tripled. To this day the Major League of Baseball still uses this cork core. Then in 1931 the baseball was improved again implementing rubber around the cork core and raised stitches which provided a more balanced ball and gave pitchers more control over the spin of the ball. These changes reduced the speed of the ball. What the designers of the baseball in 1931 didn't realize were the complex aerodynamic effects the seams played in the flight in the baseball. In 1974 the final major change in the baseball was made by replacing the horsehide cover with cowhide mainly for economic reasons.

The study of aerodynamics of sports balls dates back before the game of baseball was created. After noticing a tennis ball curve, Isaac Newton decided to scientifically explore the path of a ball's flight through the air. This interest carried on through the

years and as technology improved experiments could be conducted with greater accuracy. A more thorough understanding of the flight of a sphere, such as a tennis ball, golf ball or baseball, has been developed and researched by many. To this day, sphere aerodynamics are still studied. With some sports ball types, like the baseball, explanation of its flight phenomena is still uncertain.

Sports athletes and strategist value knowing the behavior of the equipment they use in their games. In baseball, aerodynamic ball properties such as lift and drag are important to understand what type of pitch will allow a ball to be hit with greater velocity or higher lift. From the pitchers perspective, knowing which pitches to throw can aid in reducing big hits. From the batters perspective, knowing how to optimally hit a baseball and which pitches produce an optimal hit can enable batters to hit more homeruns. Manufacturers and league regulators also have interest in the characteristics of the baseball such that they understand the affects each component of the ball has on the trajectory.

In 1936 all major components of the baseball design was complete. During this time period knowledge of lift and drag was still in its elementary stage, so the baseball was designed to be easy to manufacture and provide lively stable game play. Simple regulations such as diameter, weight, seam height, and materials used in the core were implemented, but lift and drag were not directly taken into consideration.

Research presented in this work is intended to benefit the entire baseball and sports community to better understand the flight of a baseball, but not intended to directly improve or optimize pitched or batted baseballs. This research also intends to understand drag on other sports balls. A numerical approach to lift and drag was attempted, but

resulted with little success. An experimental approach to lift and drag analysis was conducted experimentally by projecting balls in a lab setting. The ball traveled through a series of light gate boxes that recorded speed and displacement of the ball. Compared to other fluid based experiments in the past, this experiment moved the ball through the fluid. The intent was to obtain lift and drag from balls in a more game like behavior.

Chapter II– Literature Review

Section 2.1 – Background: The Flight of the Baseball

Understanding the flight of a baseball involves two major aerodynamic properties, lift and drag. Lift can be described as the forces on a ball which are directed perpendicular to the ball's trajectory, where drag is described as a force in the opposite direction of the ball's flight path (3). The lift force was first studied by Isaac Newton, but later explained and credited to G. Magnus in 1852 which is now commonly known as the Magnus force or Magnus effect. Lift on a ball is a function of the ball's surface geometry, velocity, orientation, and rotation. In the mid 1950's Prandtl conducted a lift and drag analysis by studying spheres of various roughness and further explained Magnus' findings that the lift was caused by a nonsymmetrical separation of flow in the ball's boundary layer region. The coefficient of lift, C_L , can be defined by (4)

$$C_L = \frac{2F_L}{\rho AV^2} \quad (2.1)$$

where F_L (or F_M) is the force due to lift, ρ is the fluid density, A is the cross sectional area of the ball, and V is the velocity of the ball through the fluid. Similar to the lift force, the drag force is a function of surface roughness, velocity, orientation, and rotation of the ball. Scientists began studying different spheres as they discovered drag on a smooth sphere did not remain constant as velocity or surface roughness changed. Recent research has shown that a sphere will go through three critical Reynolds regions where the coefficient of drag on the sphere will drastically change. The coefficient of drag, C_D , can be defined by (4)

$$C_D = \frac{2F_D}{\rho AV^2} \quad (2.2)$$

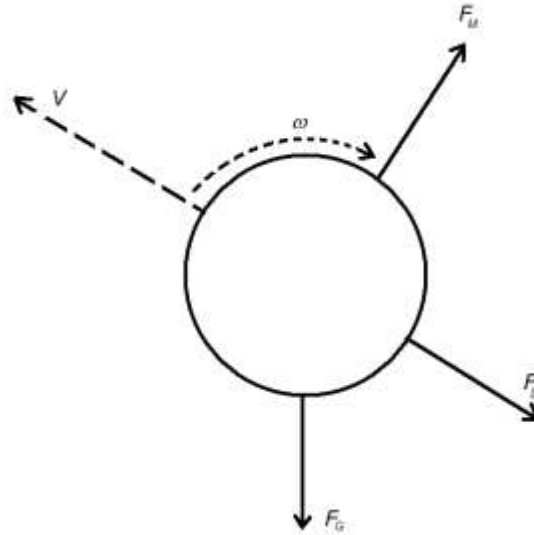


Figure 2.1 - Free body diagram of a translating and rotating sphere.

where F_D is force due to drag (see Figure 2.1). The second region, the Drag Crisis, is of the most interest by scientists since the sphere's coefficient of drag will significantly drop over a small change in Reynolds number. Reynolds number, Re , can be defined by (4)

$$Re = \frac{VD}{\nu} \quad (2.3)$$

where D is diameter of the ball, and ν is kinematic viscosity of air.

Section 2.2 – Overview of Boundary Layer Behavior

Before going into further discussion about lift and drag on an object, it is prudent to understand and give an introduction to the fluid and boundary layer behavior. Prandtl (5) went into great detail to explain boundary layers and their behavior with respect to fluid viscosity and object geometry. An object in a moving fluid is affected by the flow behavior very close to the object in a region known as the boundary layer. This is a very thin velocity distribution layer at the surface of the object where velocity ranges from zero to free stream velocity (5). Free stream velocity is the velocity of the unobstructed flow. The reason for the reduction in velocity near the wall of the object is due to the

object's friction and viscous shear forces at the surface. The velocity of the fluid at the surface of the object is zero and at some boundary layer thickness distance δ the fluid velocity is roughly equivalent to the free stream velocity. The height of the boundary layer is dependent on the fluid viscosity, μ , fluid density, ρ , fluid free stream velocity, v , and the length of the object, l , fluid is being passed over. The boundary layer for laminar flow over a flat plate (see Figure 2.2) can be found as (5)

$$\delta = 5 \sqrt{\frac{\mu l}{\rho v}} \quad (2.4)$$

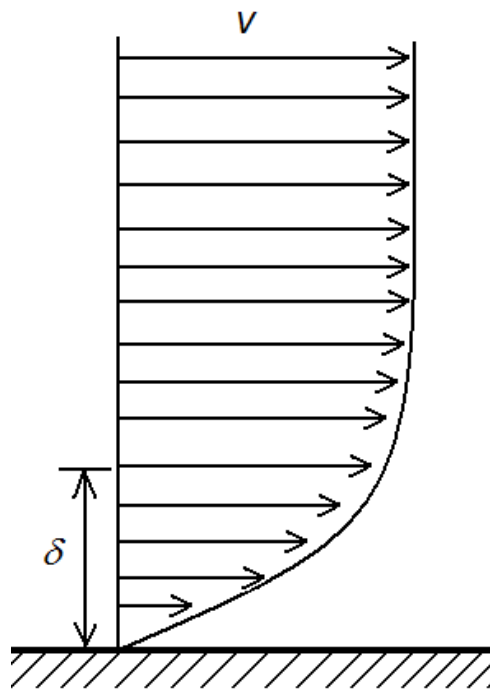


Figure 2.2 – Velocity distribution in the boundary layer over a flat plate

For example, a flat plate 2.85 inches long with air flowing over it at 73 mph at 80 degrees Fahrenheit will have a boundary layer thickness of 0.0074 inches. The boundary layer thickness for turbulent flow over a flat plate can be found as (6)

$$\delta = 0.14 \left[\frac{x}{(\text{Re}_x)^{1/7}} \right] \quad (2.5)$$

where x is the distance from the leading edge of the flat plate and Re_x is the Reynolds number at x distance along the plate.

The lift and drag forces are influenced strongly by the flow type and behavior in the boundary layer. Laminar flow can be described as slow, uniform, and a smooth appearance where turbulent flow can be described as fast, violent, unpredictable mixing. Laminar flow in the boundary layer can become turbulent very quickly with the slightest disturbance or obstruction of flow. As flow passes around a smooth cylinder or sphere the flow can go through many different states. The object will go through a series of vortex shedding stages in Reynolds number <200 . Viscous forces contribute a noticeable amount of drag in this region. Once flow becomes fast enough, $400 < \text{Re} < 3 \times 10^5$, the object enters the low range Reynolds number region where pressure forces become dominant over the viscous forces. For purposes of this paper, the low Reynolds region hereafter will be considered $\text{Re} < 3 \times 10^5$ since a ball in flight rarely travels below $\text{Re}=400$. During the low range of Reynolds numbers separation on the object will occur diverting flow and forming vortices downstream. Pressure downstream stays constant but is much lower than the free stream pressure. This will cause high drag (7).

During actual play, sports balls are expected to go through three critical Reynolds regions where flow separation can change lift and drag dramatically. These three regions are shown below as a two dimensional cylinder or smooth sphere in Figure 2.3.

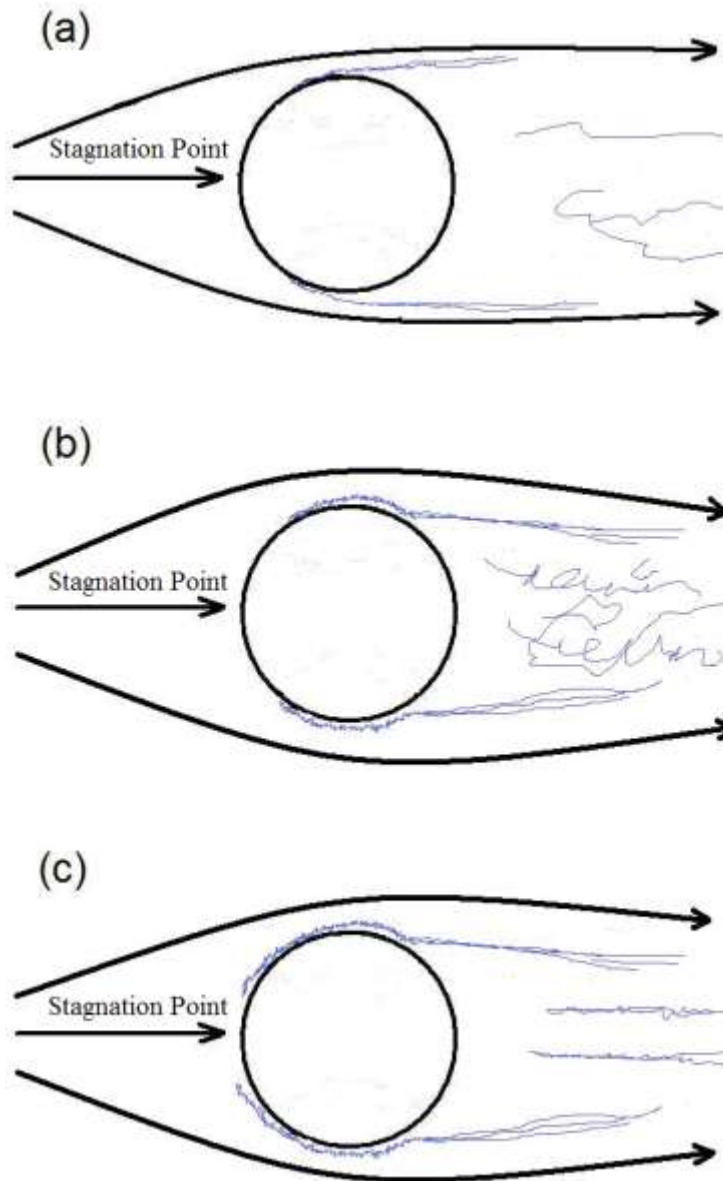


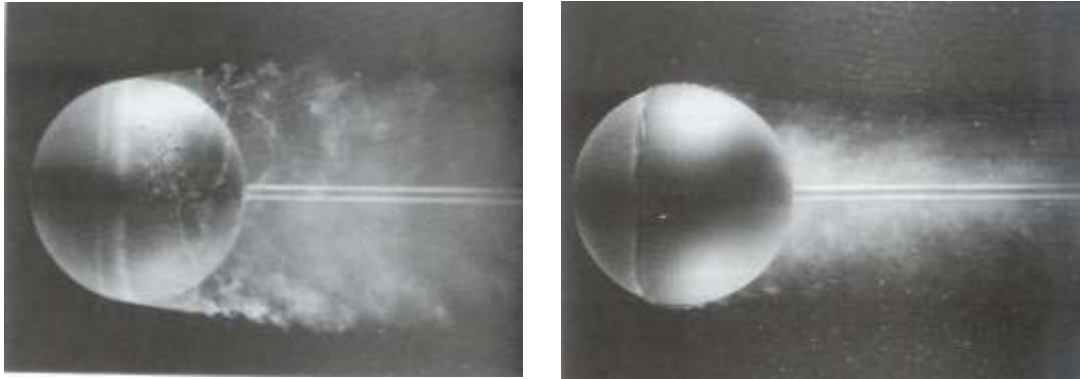
Figure 2.3 - Flow over a smooth cylinder: (a) $Re < 3 \times 10^5$, flow stays laminar in the boundary layer until 80° where it separates; (b) $3 \times 10^5 < Re < 3 \times 10^6$, flow separates at 80° becomes turbulent and reconnects before separating again at 120° ; (c) $3 \times 10^6 < Re$, flow is turbulent in the boundary layer on the front and stays turbulent until separating at 120° .

During the first critical Reynolds region, $Re < 3 \times 10^5$ (see Figure 2.3a), the flow stays laminar until roughly 80° from the stagnation point where laminar flow will separate from the object. Pressure downstream is lower in the separation area, thus drag

is increased. Once the ball enters the second critical Reynolds region or drag crisis region, $3 \times 10^5 < Re < 3 \times 10^6$ (see Figure 2.3b), the flow loses stability and separates in the boundary shear layer at 80 degrees from stagnation point. The boundary layer flow becomes turbulent, reconnects to ball surface and finally separates on the back side of the ball around 120 degrees from the stagnation point. This reconnection in the boundary layer delays flow separation and overall has less separation area and results in pressures similar to free stream pressure. This causes a severe drop in drag, sometimes up to 70% relative to the previous region. In the third and final critical region, $Re > 3 \times 10^6$ (see Figure 2.3c), drag will increase slightly. Flow becomes turbulent just after the stagnation point on the front of the object and stays turbulent until finally separating a small degree before 120 degrees. The pressure is lower than in the first critical region but higher than the drag crisis region.

Once the object begins to rotate in the fluid the relative fluid velocity at the surface changes. This difference in velocity from one side of the object than the other can cause an asymmetric flow separation on the ball. On the side where the flow is parallel with the rotational velocity the flow might be separating at the 80 degree location, whereas flow on the other side where rotation opposes the flow, the separation point might occur at the 120 degree location. The imbalance flow separation results in an imbalance of pressure distribution causing forces on the object perpendicular to air flow.

Laminar flow in the boundary layer is highly sensitive to geometry and surface roughness and can change flow separation. A small scratch or thread on a ball can transform the laminar flow to turbulent flow inducing the second critical region at lower Reynolds number.



a)

b)

Figure 2.4 – a) Flow over a smooth sphere; b) Flow over same smoother sphere with a trip wire placed on the front half of the surface. (7)

In Figure 2.4a, the flow around the smooth sphere is in the first critical Reynolds region. The smoke is laminar in the boundary until 80 degrees where flow separates from the ball and fans outward. The second image, Figure 2.4b, a trip wire has been added just before the separation point. The flow over Figure 2.4b is around Reynolds 30,000, which normally would have been subcritical. This small wire perturbs the boundary layer causing turbulence before the 80 degree separation. The turbulent flow in the boundary layer causes flow to reconnect to the ball and stay connected until the 120 degrees on the backside of the ball. Thus an onset of the drag crisis can be at a lower Reynolds number in the event of a disturbance in the boundary layer on the front side of the ball.

Section 2.3 – Lift and drag studies on balls, spheres, and other objects

Isaac Newton and Heinrich G. Magnus were first credited to lift analysis on a rotating object. At the time, Magnus (8) observed that spherical bullet shot out of a gun deviated from their expected target. Magnus decided to investigate on a smaller scale

with an experiment that involved rotating a cylinder while passing air around it. Magnus explained that the deviation takes place towards the side of the cylinder that the rotational motion direction is opposite to the cylinder's progressive motion. He explained, without the knowledge of boundary layer behavior in the early 1900's, that the pressure on the side where the rotational air opposed the translational air would see a lower pressure relative to the other side of the ball. Or the side with the rotational direction in the same direction as the air flow would see a decrease in pressure. Hence a force on the ball would be exerted causing a deviation in flight path (see Figure 2.5). Initially scholars explained the phenomena using the Bernoulli principle, meaning when a fluid has a velocity increase then it will also have a pressure decrease. Magnus made no reference to the roughness of the cylinder or that pressure around the cylinder changed with surface roughness. What Magnus did not realize is that the deviation was not caused by the Bernoulli principle, but was actually caused by disruption of fluid in the boundary layer, micro inches from the surface of the ball.

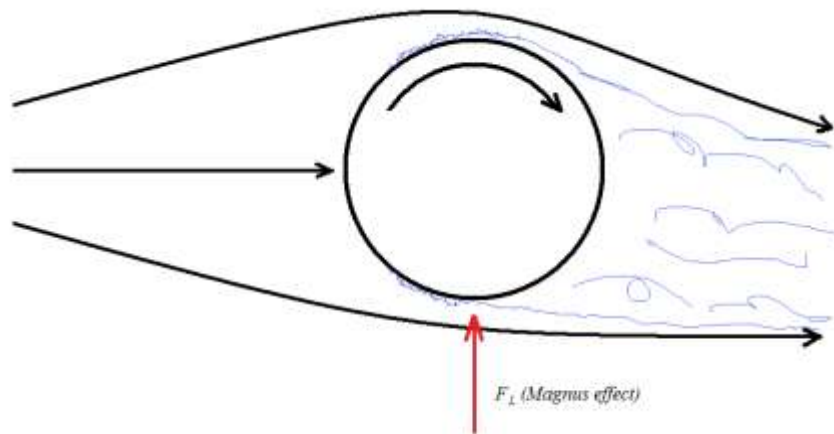


Figure 2.5 - Flow over ball with Magnus effect.

Magnus' theory of lift force was accepted for some time until Prandtl's discovery of boundary layers. Prandtl (5) observed that near the object's wall, a boundary layer existed. Lift and drag were greatly affected by the flow type and disruptions in this boundary layer. Prandtl, conducted experiments, similar to the image shown in Figure 2.4 and visually analyzed how disruptions in the boundary layer on the upstream side of the sphere induce turbulence and delay final separation to the backside of the sphere. The point at which the separation occurred on the ball directly affected the amount of drag or lift that was observed. Next to geometry, the separation point and behavior in the boundary layer is the cause of lift and drag.

Intrigued by the Magnus effect, Prandtl experimented with rotating cylinders. Flow was passed over a cylinder while varying its rotational velocity (see Figure 2.6). On the top surface where airflow was parallel with angular velocity, separation in the boundary layer never occurred. As expected, on the bottom side where angular velocity of the cylinder was opposing airflow, separation occurred. Thus, a strong eddy was formed and an imbalance of pressure produced force in the upward direction on the cylinder. This force, the Magnus effect, causes spheres to lift.

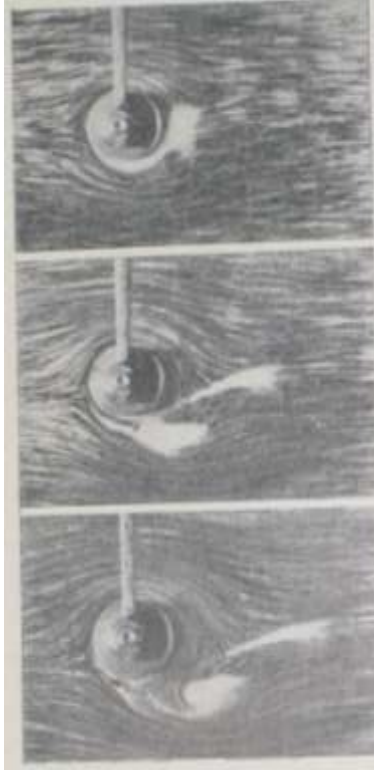


Figure 2.6 - Flow around a cylinder rotating clockwise. Three images show cylinders rotating progressively faster with the upper image being the slowest and the lower image being the fastest (7).

Once wind tunnel technology was developed experiments could be conducted more accurately on larger objects, mostly spheres of varying roughness and golf balls. Maccoll (9), and Davies (10) studied lift and drag on spheres in the early 1900's. With little lift and drag data on rotating sphere's, Davies decided to use a wind tunnel to study rotating golf balls. Davies placed a golf ball between two rotating cups just outside his horizontal wind tunnel. As the ball reached its target angular velocity it was released and dropped into the wind tunnel. The ball was forced down the tunnel at wind velocities of 105 feet per second and the contact point with the bottom of the tunnel was recorded. The deflection was converted into a lift and drag. Davies found a C_D in the first critical Reynolds region, $Re \sim 9 \times 10^4$, to be around 0.44.

Briggs (11) studied the effect that spin and speed had on the forces of a pitched baseball. His first experiment involved an air gun constructed by the National Bureau of Standards. The ball was placed on a spinning tee and was impacted with a projectile from the air gun driving the ball 60 feet where a lateral deflection was measured. The test was eventually abandoned since it resembled a ball after it had been impacted by a bat rather than thrown by a pitcher. His next experiment was set up such that a rotating baseball could be dropped into an octagonal wind tunnel, similar to Davies' experiment. The ball was coated lightly with lubricant containing lamp black. The bottom of the tunnel was lined with card board such that the ball would leave a mark on its first impact and a deflection could be measured. Samples were taken at 0 – 1800 rpm and 75 to 150 mph. Data related to lateral deflections of 10.8 inches to 17.5 if the ball was to travel 60 feet. Briggs commented that the amount the ball deflected over 60 feet was proportional to spin and the square of the wind speed (see Figure 2.7 and Figure 2.8).

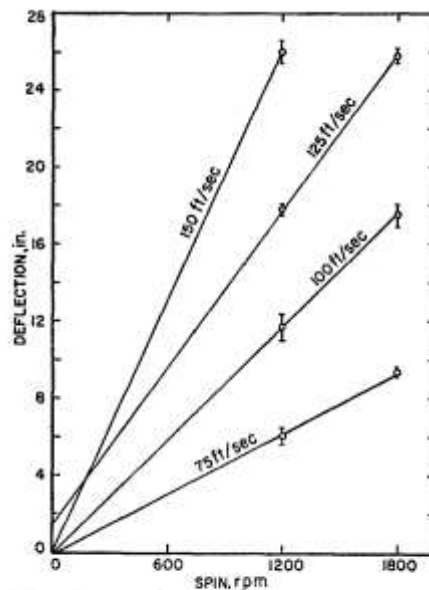


Figure 2.7 - Lateral deflection of a baseball, spinning about a vertical axis, when dropped across a horizontal windstream. These values are all for the same time interval, 0.6 sec, the time required for the ball to cross the stream. (11)

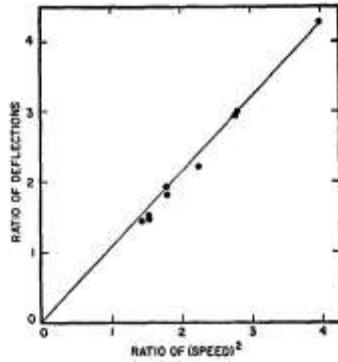


Figure 2.8 - Graph showing that the observed lateral deflections are proportional to the square of the wind speed. (11)

Briggs did not reduce the data to find the coefficient of lift or drag on the baseballs.

Several years later interest in this field was sparked again with Achenbach (12) passing airflow around spheres at high Reynolds numbers in a wind tunnel. A wide range of velocities were achieved in his experiment contributing a full C_D curve through the three critical Reynolds regions that a sphere was said to go through. Achenbach mounted a 20 cm diameter sphere to a 2 cm support pole inside the tunnel and measured forces using

strain gages attached to the sphere supports. Data from this experiment (see

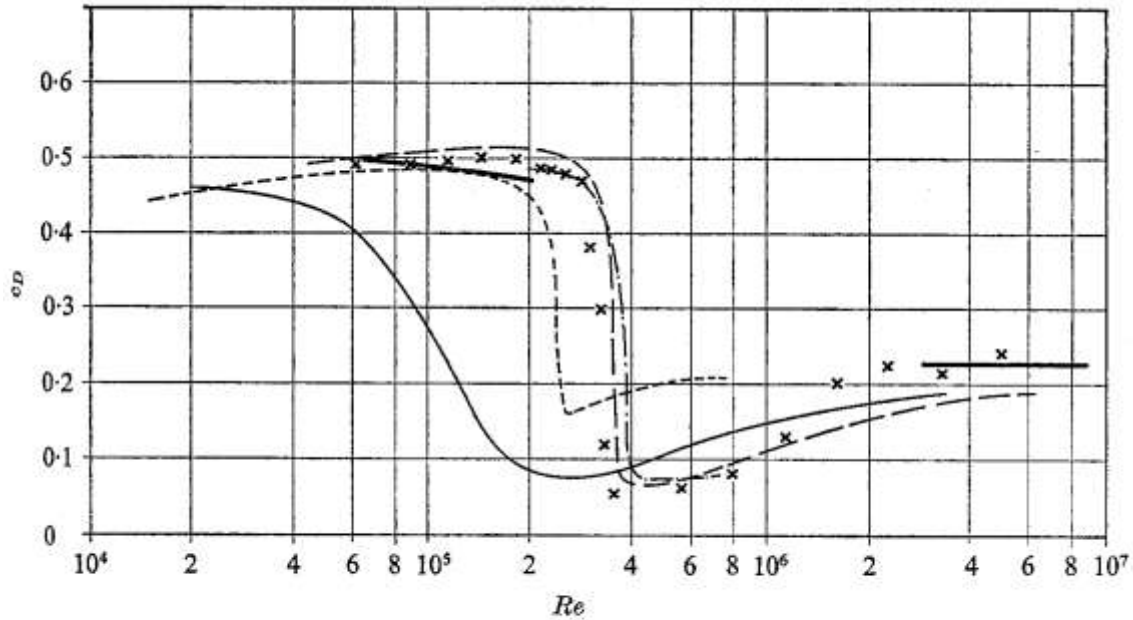
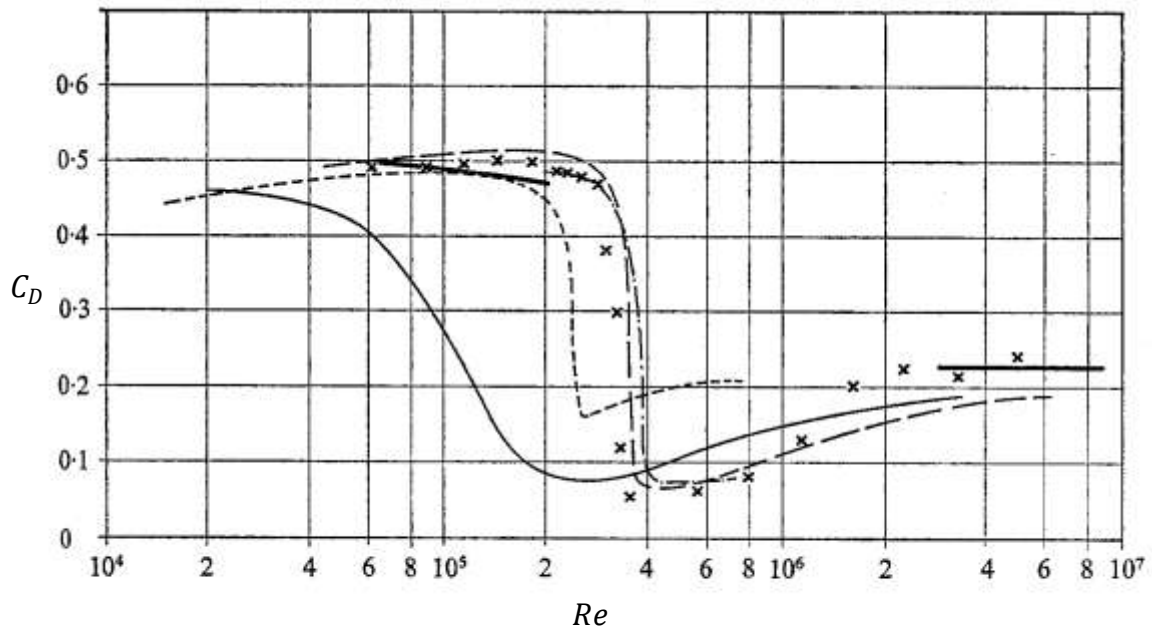


FIGURE 6. Drag coefficient of the sphere as a function of Reynolds number; comparison with literature. —, Wieselsberger (1922); —, Bacon & Reid (1924); —·—, Millikan & Klein, free-flight (1933); —, Maxworthy (1969). Present results: —, from strain gauges; ×, from integration.

Figure 2.9) showed the drag crisis region at higher Reynolds numbers than that of Wieselsberger (13). Achenbach's data clearly showed a drag crisis beginning at a Reynolds number of 3×10^5 and finishing around 4×10^5 . This differed from Maxworthy and Weiselsberger. Achenbach criticized Wieselsberger's experiment explaining the high value of C_D at $Re\ 4 \times 10^5$ was due to the support system he used. Maxworthy (14) conducted his experiment by mounting a sphere inside a wind tunnel as well, and performed tests under a variety of conditions which included tunnel blockage, boundary layer tripping, and inserting objects downstream of the sphere to disrupt the recirculation region. Achenbach's data supported Millikan and Klien's (15) free flight test (see Figure 2.10).



Drag coefficient of the sphere as a function of Reynolds number; comparison with literature. ---, Wieselsberger (1922); —, Bacon & Reid (1924); —·—, Millikan & Klein, free-flight (1933); —, Maxworthy (1969). Present results: —, from strain gauges; ×, from integration.

Figure 2.9 - Drag coefficient of the sphere as a function of Reynolds number taken from (12).

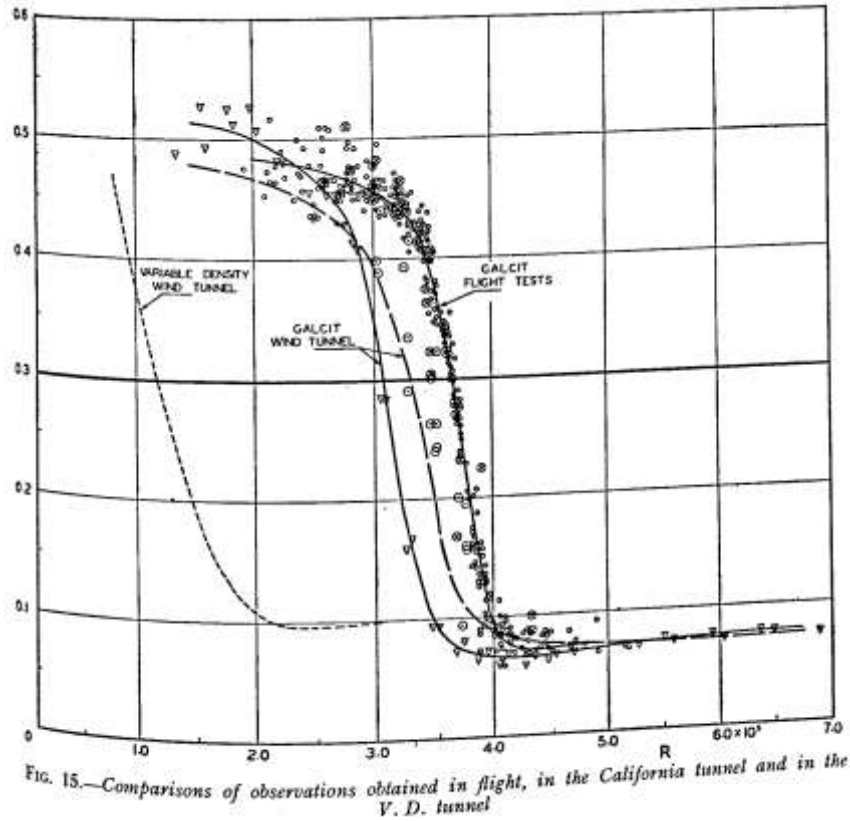


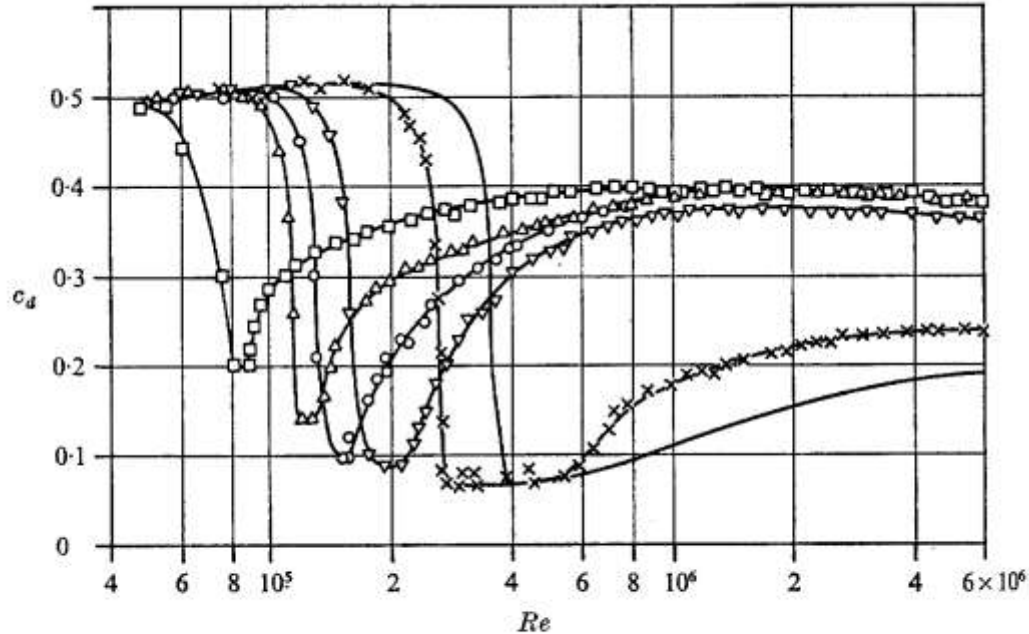
Figure 2.10 - Data taken from wind tunnel and flight tests by Millikan and Klein.

In the free flight tests by Millikan and Klein, Klein built an apparatus that was mounted to an airplane. The plane was flown through the atmosphere at different velocities. This eliminated disturbances and turbulence issues that were common in wind tunnel experiments. However the sphere was still attached to a rod on the backside which measured pressures and forces.

Achenbach was also curious how surface conditions of the sphere influenced the drag. The second part of his research was varying the roughness of the sphere and placing them in the same high speed wind tunnel as he used in the previous experiment.

Achenbach characterized the ball by roughness parameter $\frac{k}{d_s}$, where k was the height of

the roughness element and d_s was the diameter of the sphere. Achenbach used spheres with $\frac{k}{d_s}$ ranging from 1250×10^{-5} to 25×10^{-5} .



Drag coefficient c_d vs. Reynolds number for a sphere. Parameter: surface roughness. —, smooth (Achenbach 1972); \times , $k/d_s = 25 \times 10^{-5}$; ∇ , $k/d_s = 150 \times 10^{-5}$; \circ , $k/d_s = 250 \times 10^{-5}$; \triangle , $k/d_s = 500 \times 10^{-5}$; \square , $k/d_s = 1250 \times 10^{-5}$.

Figure 2.11 - C_D curves while varying surface roughness of spheres.

Achenbach's data showed (see Figure 2.11) that as surface roughness increased the onset of the drag crisis occurred at lower Reynolds number. The data also showed as roughness increased the drag crisis magnitude decreased. Increased surface roughness induced turbulence at a lower Reynolds number, which moved the drag crisis to a lower Reynolds number. This can be related to the trip wire placed on the front side of the sphere (7). The trip wire added roughness or an obstacle in the boundary layer that induced turbulence preventing the flow from separating at 80 degrees from stagnation. As described before, the added turbulence in the boundary layer caused flow to reconnect, travel to the backside of the ball, and disconnect at 120 degrees. The surface

roughness of Achenbach's spheres was causing turbulence in the boundary layer at lower Reynolds numbers. An explanation of the less severe drag crisis and higher overall C_D is due to the increase in overall surface friction.

Understanding the importance of asymmetric obstructions in the boundary can help predict how a ball moves through the air. When large obstructions, such as the stitches on a baseball, pass through the critical boundary layer on a sphere the separation point on the surface will change. As Achenbach discovered, the surface roughness of the sphere can drastically change the separation point on the sphere and the magnitude of the drag force. A great example of asymmetric surface roughness is a baseball's stitches. In the game of baseball a knuckleball pitch is described by batters as being unpredictable during flight. A knuckleball is thrown by placing the ball on the knuckles of a pitcher's hand such that nearly zero rotation is applied when released. A batter can see a curveball and predict its path as it comes near the plate since its curve direction is constant through its flight. However the knuckle ball is said to change directions in mid flight. Watts and Sawyer (16) explored the aerodynamics of a knuckleball. Experimentally exploring this phenomenon, Watts and Sawyer mounted a baseball with the standard stitch pattern inside a wind tunnel to a device that measured forces on the ball. The baseball was incrementally turned in the wind tunnel and forces were recorded (see Figure 2.12).

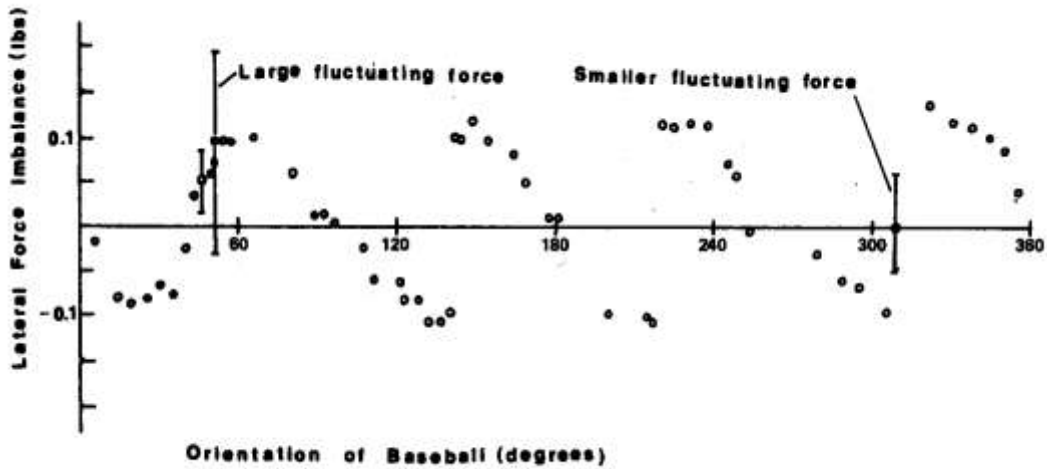


Figure 2.12 - Variation of the lateral force imbalance with orientation of the baseball. (16)

Watts and Sawyer concluded that there are two mechanisms for this fluctuation. One could be the fluctuating lateral force when the stitch was in the separation region of the ball. The boundary layer could be switching between laminar and turbulent causing fluctuating pressures on the ball. A more likely situation is the ball was slightly turning causing the stitches to produce an asymmetric roughness. The asymmetric roughness causes asymmetric separation, which leads to a non-uniform pressure distribution on the ball. Since the knuckleball is rotating very slowly, the result is an unpredictable erratic flight path. The lateral force imbalance exerted on the ball appeared to be sinusoidal with respect to the degree it was rotated. The oscillating Magnus force as a function of lateral deflection, was modeled by Watts and Sawyer as

$$x = \frac{F_0 \sin(\omega t + \pi)}{m\omega^2} \quad (2.6)$$

where x is the lateral distance, F_0 is the lateral force, m is the mass of the baseball, t is time, and ω is angular velocity of the ball.

Curious in how surface roughness could change the boundary layer behavior on an object, Bearman and Harvey (17) studied the properties of lift and drag on various golf ball types in a wind tunnel test. A conventional dimpled ball, hexagonally dimpled ball, and a smooth sphere were tested. The wind tunnel velocity was constrained to 100 mph, thus a ball model 2.5 times larger than an actual golf ball was used to achieve the corresponding Re that actual golf balls have during flight. The model was hung between two wires in the wind tunnel with the upper wire connected to a load cell to measure lift force. The strain gage arm was mounted to a balance beam which was used to measure drag force. Inside the ball model, a motor was used to apply rotation at various speeds. As previously found, when the rotational speed increased for a given airflow velocity, lift on the ball increased. Being able to measure lift and drag at the same time, trends of drag verses angular velocity could be analyzed. While holding translation velocity constant, Bearman and Harvey found as angular velocity increased both C_L (Figure 2.13) and C_D (Figure 2.14) increased. For a smooth sphere measurements of C_L were as high as 0.5 which occurred at the highest rotational speed, but the slowest airflow velocity.

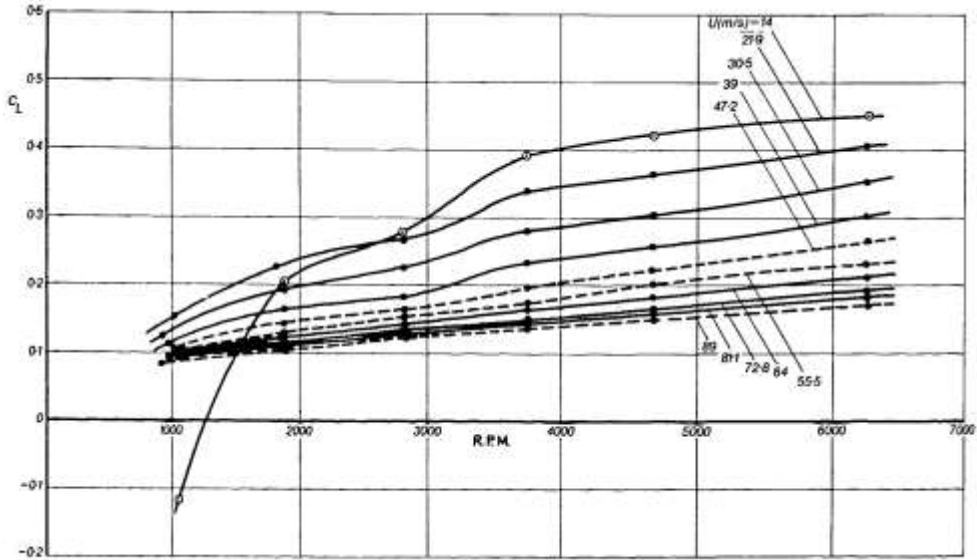


Figure 2.13 - Lift coefficient for a conventional golf ball. (17)

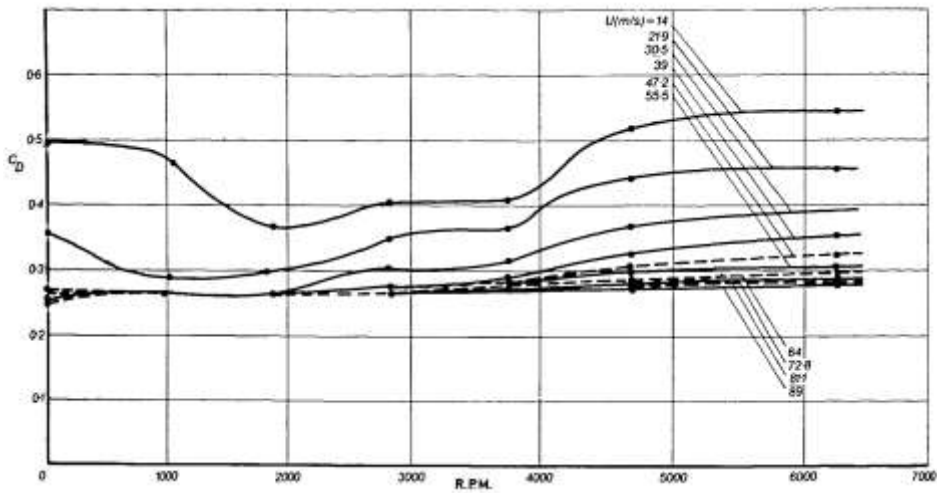


Figure 2.14 - Drag coefficient for a conventional golf ball. (17)

In the mid 1980's, more interest began to be directed towards the baseball since a wide variety of research had been conducted on spheres of varying roughness and golf balls. Watts and Ferrer (18) analyzed actual baseballs in a subsonic wind tunnel to

measure the lift forces on a baseball in three different stitch orientations. Watts and Ferrer's experimental setup mounted a baseball on a shaft and was placed in a wind tunnel. A device was used to spin the ball while another was used to measure the lift force on the ball. A ratio of $\pi D\omega/V$, where D is the diameter of the ball, was used to plot their results against the three published data sets for C_L of a rotating sphere. Results for C_L differed from the Sikorsky, Briggs, and Davies, but was consistent with Bearman and Harvey (see Figure 2.15).

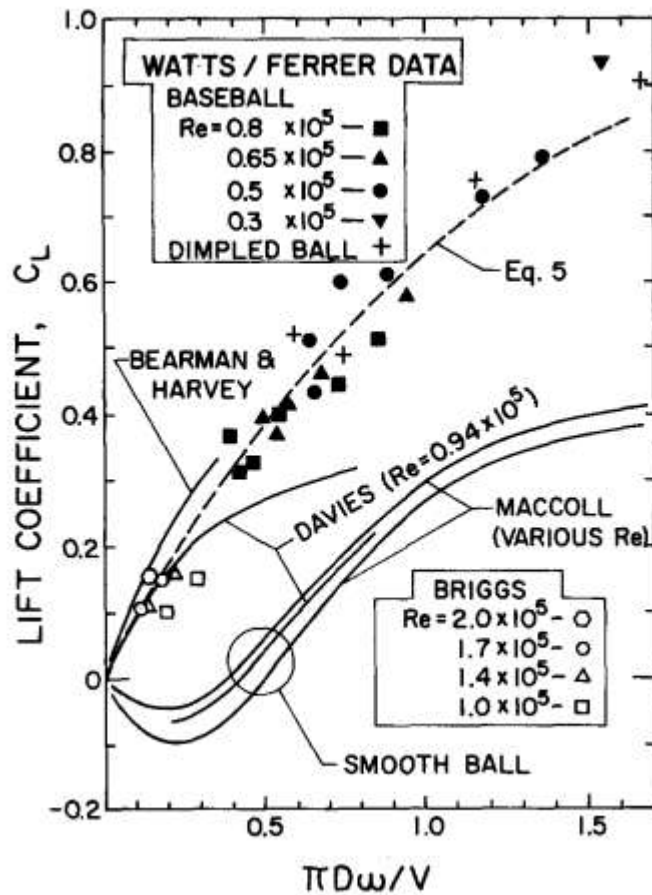


Figure 2.15 - Lift coefficient data comparing several data sets.

After rediscovering Sikorsky and Lightfoot data that had appeared to have been lost for many years, Alaways (19) made comparisons with his own lift data. Sikorsky, similar to Watts and Ferrer, mounted a MLB baseball on thin shaft and spun the ball in a wind tunnel. Data for the four seam orientation showed values of C_L reaching 0.2 for a spin factor of 0.15. This agreed with Alaways' four seam data. Comparisons between Watts and Ferrer and Sikorsky are difficult to make since there was a large gap in spin (0.2) factor where Sikorsky left off and Watts began.

Up until the late 1990's, there was great difficulty analyzing projected baseballs in laboratory experiments. In the 1996 Summer Olympic Games, pitched baseball trajectories were measured and analyzed by Alaways, Mish, and Hubbard (20). Using two 120-Hz speed cameras, baseball pitches were recorded. The camera resolution was 640x480, which relates to an image of the baseball only filling one or two pixels. A dynamic model of the baseball trajectories was developed to estimate pitch trajectories given different initial conditions. Alaways (21), claimed that the baseball's translational velocity for a flight distance from the pitching mound to home plate will only change by 5% and the angular velocity will change even less. The constants C_D and C_L were assumed constant and found for each pitch. C_L was said to depend on Re (22). Alaways, Mish, and Hubbord observed that C_L has dependence on the spin parameter, S ,

$$S = \frac{r\omega}{V} \quad (2.7)$$

for baseballs where r is the radius of the ball, ω is the angular velocity of the ball, and V is the translational velocity of the ball. This spin factor concept used by Alaways, Mish, and Hubbord is similar to the ratio $(\pi D\omega/V)$ used by Watts and Ferrer. Using this relationship and the translational equations of motion, a pitched baseball model was

developed. These estimations were used in conjunction with the experimental data to approximate the initial conditions at the release of the pitch.

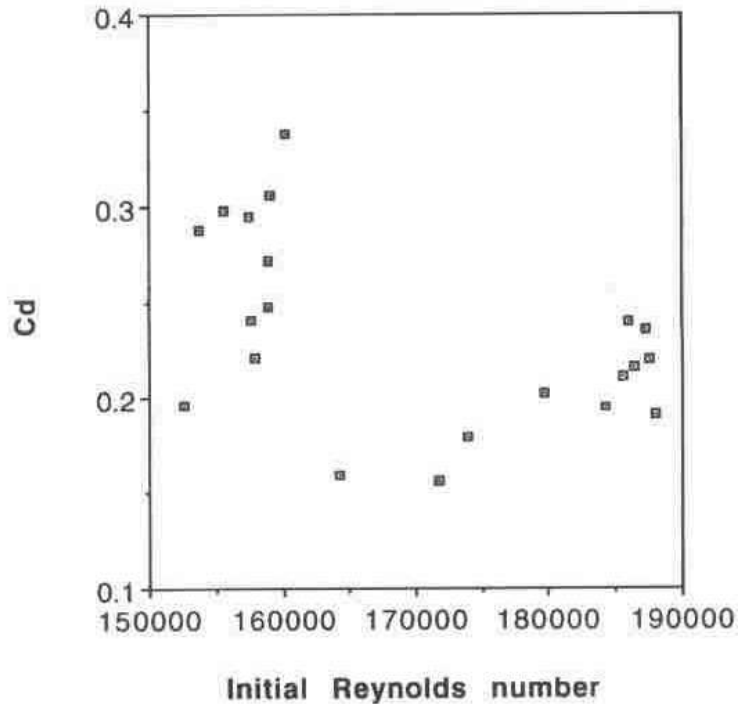


Figure 2.16 – Drag coefficient of various pitches. Data suggests a drag crisis occurs with C_D as low as 0.16. The model was also used to estimate C_D for different pitches (see Figure 2.16). Though there were not enough data points for statistical certainty, the data reflected a drag crisis. C_L data was not explored by Alaways, Mish, and Hubbord in this experiment.

The most recent research involving the lift force on a baseball was conducted by Nathan (23), which involved ten high speed cameras to track a ball over a distance of 15 feet. Different from Alaways, Nathan used one set of cameras to track the entire path of the ball. This same set of cameras was able to track translational and rotational components of the ball. The cameras operated at 700 frames per second and tracked reflective dots marked on the baseball which reflected light back to the camera. Using special reconstruction software, the position of the ball was plotted and lift and drag

forces were calculated. A two wheeled pitching machine was used to project balls with translational velocity from 50-110 mph and angular velocity from 1500-4500 rpm. This relates to a spin factor range from 0.09-0.595. A total of 22 pitches were analyzed (see Figure 2.17).

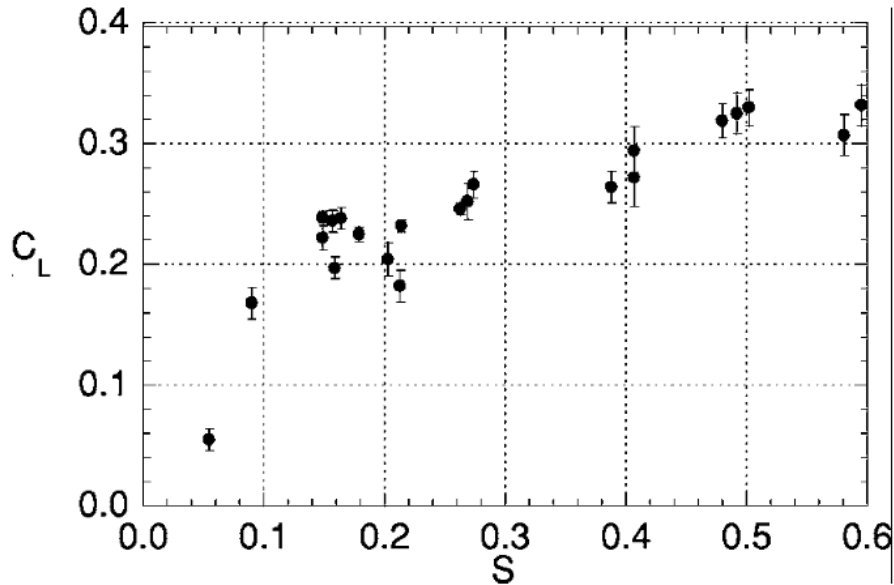


Figure 2.17 - C_L trend found in Nathan's experiment. 22 pitches were analyzed.

Nathan found that C_L depended on the spin factor. As the spin factor increased, C_L increased. From spin factor 0 – 0.15 the lift sharply increased. After spin factor 0.15 the C_L trend continued to increase but at a lower rate. This trend was also seen in previous research (see Figure 2.18). The solid line came from a bilinear best fit curve to several published C_L data (24),

$$C_L = 1.5S, S \leq 0.1 \tag{2.8}$$

$$C_L = 0.09 + 0.6S, S > 0.1 \tag{2.9}$$

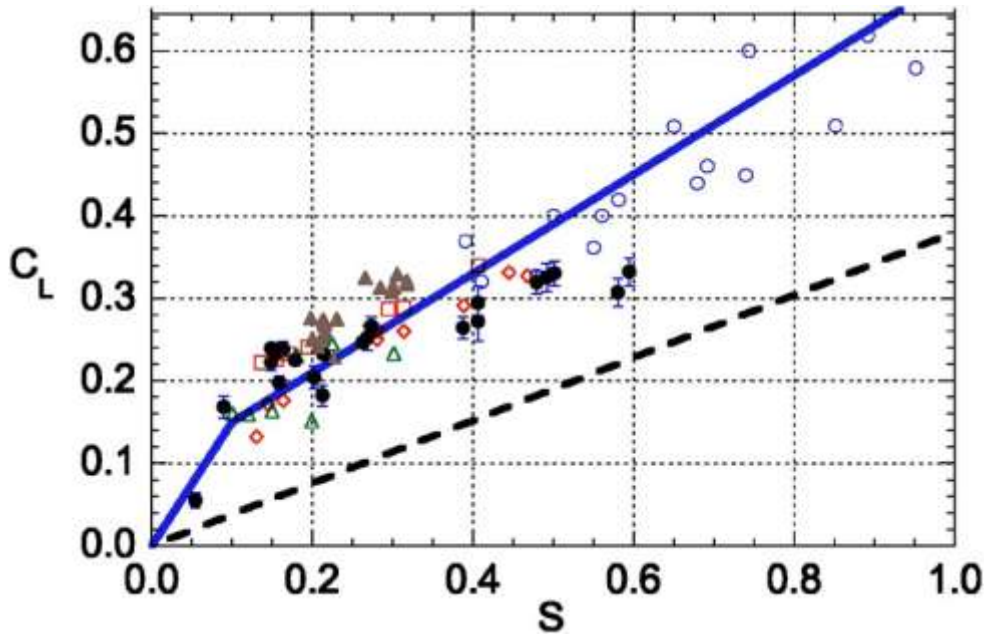


Figure 2.18 - Results for C_L from various experiments. closed circles are from Nathan; open circles are from Watts and Ferrer; open triangles are from Briggs; open diamonds and squares re from Alaways two and four seam, respectively; closed triangles are from Jinji (25); solid line is from parameterizations of Sawaicki, Hubbard, and Stronge (24); dashed is from $C_L = 1.5S, S \leq 0.1$ (2.8).

Nathan's results showed a similar trend to previous research were C_L increased sharply up to a spin factor of 0.1, then continued to increase but at a lower rate. Nathan calculated C_D but said the data was too scattered to show any statistical certainty.

Similar to Alaways' (20) experiment which recorded actual pitched balls during game play, Nathan (26) used the PITCHf/x (27) camera system to track pitched baseballs from the pitcher's mound to home plate. Using kinematic equations, Nathan found accelerations of the ball in the horizontal and vertical directions. From these accelerations, lift and drag forces were found and reduced to C_L and C_D curves (see Figure 2.19).

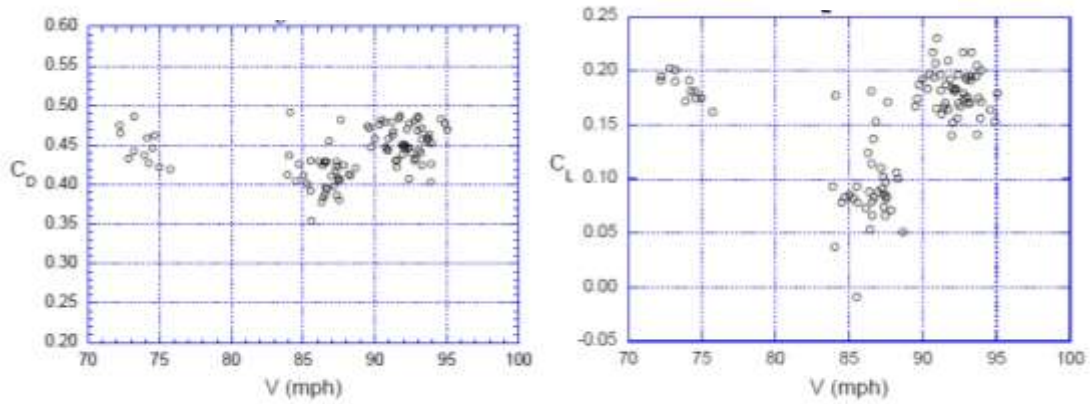


Figure 2.19 - C_L and C_D reduced from PITCHf/x tracking system

Nathan found little evidence of a drag crisis. The C_D of most pitches fell in the 0.40 and 0.5 range.

Section 2.4 – Reverse Magnus Effect

Researchers, such as Briggs and Davies, were analyzing the lift forces on rotating spheres and noticed a counter intuitive phenomenon. Rotating balls were deflecting in an opposite direction from what was expected. When a ball had back spin, a normal Magnus effect would push the ball upward. They were experiencing a reverse Magnus effect where the ball with back spin would be forced downward (see Figure 2.20).

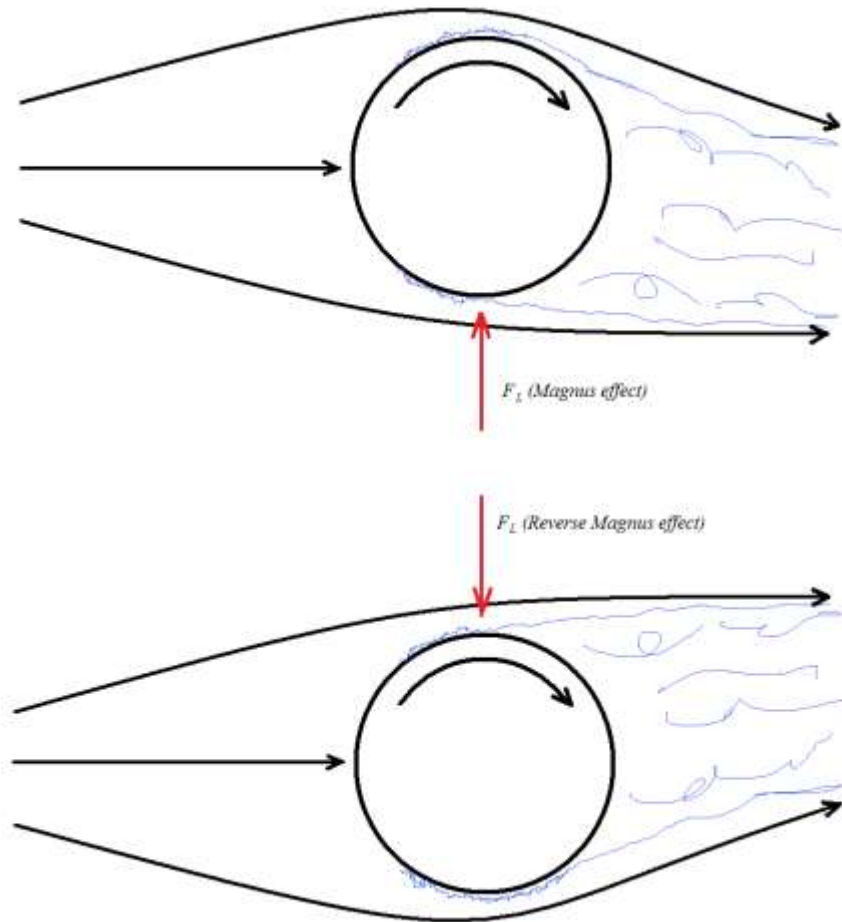


Figure 2.20 - Flow propagation for Magnus effect and reverse Magnus effect.

In order for a reverse Magnus effect to occur, separation at the 80 degree location on the sphere will occur on the side where rotation is parallel with airflow. If a sphere is moving at the appropriate translational and rotational velocity the side of the ball opposing the flow will become turbulent in the boundary layer, reconnect and separate on the backside of the ball. On the other side of the ball where flow is in the same direction as the rotation the boundary layer does not become turbulent and the flow separates on the front side of the ball. This reverses the Magnus effect.

Davies (10) found a pronounced reverse Magnus effect during his study of golf balls. Davies found that while comparing golf ball lift and drag with a smooth sphere of

similar diameter, at fluid velocities around 70 mph the smooth sphere produced a reverse Magnus effect for 0 to 5000 rpm. Davies only found this for smooth spheres. Bearman and Harvey found a reverse Magnus effect for smooth spheres at 1500 rpm. Briggs noted the phenomenon of the reverse Magnus effect on smooth spheres as well. Again this only occurred on the smooth spheres. Briggs questioned that Davies found a reverse Magnus effect for high angular velocities. Briggs commented,

“In Davies experiments the point of impact on the tunnel floor represents the combined effect of spin and drag, both being directed downstream. To get the lift, the point of impact had to be reduced by the drag with no spin; whereas in my baseball measurements the lateral deflection, being at right angles to the drag, could be measured directly.”

The combined effect of spin and drag might explain why Davies found the reverse Magnus effect for high angular velocities.

Section 2.5 – Numerical lift and drag analysis

By the mid 1980's enough research had been conducted on smooth spheres, rough spheres and golf balls to convince scientists that sports balls were affected by the Magnus effect and drag fluctuations. Frohlich (28) commented saying, “It would be impossible to throw a ball that curves or ‘knuckles’ i.e. changes direction sharply sideways after it has left the pitcher’s hand.” Frohlich pointed out that given the numerous experimental data, pitched or batted baseballs might go through a drag crisis. Knowing that Briggs’ experiment showed balls deviating up to 29cm, Frohlich decided to numerically investigate trajectories of balls to deduce a drag coefficient. Frohlich solved the kinematic equations for ball acceleration in the x and y direction and analyzed five

different pitch types. The purpose was to find which drag coefficients pertained to a specific pitch and batted ball type. His analysis suggested that the ball does have the possibility of going through a drag crisis. He commented that his “Type 2” and “Type 3” ball, with surface roughness factor, $\frac{k}{d}$, being 500×10^{-5} and 150×10^{-5} respectively could be close to representing the baseball.

Denbo and Kawamura (29) numerically studied the behavior of a knuckleball with rifle spin. Using the governing incompressible Navier-Stokes equation,

$$\nabla \cdot \mathbf{v} = 0 \quad (2.10)$$

$$\frac{\partial \mathbf{v}}{\partial t} + (\mathbf{v} \cdot \nabla) \mathbf{v} = -\nabla p + \frac{1}{\text{Re}} \Delta \mathbf{v} \quad (2.11)$$

where \mathbf{v} is the velocity, p is the pressure, the flow around the ball was calculated. As the ball spun a fluctuating force was observed that was dependent on the stitch orientation. The model was calculated using a fixed Reynolds number of 97,000. As observed in previous experiments and other numerical models, lift fluctuates depending on the orientation of the ball. The magnitude of the lift also depends on the initial orientation of the ball as well. In some orientations the lift force fluctuated in a sinusoidal fashion as the rifle spin was applied (see Figure 2.21). Denbo found numerical C_L with magnitudes as high as 0.15.

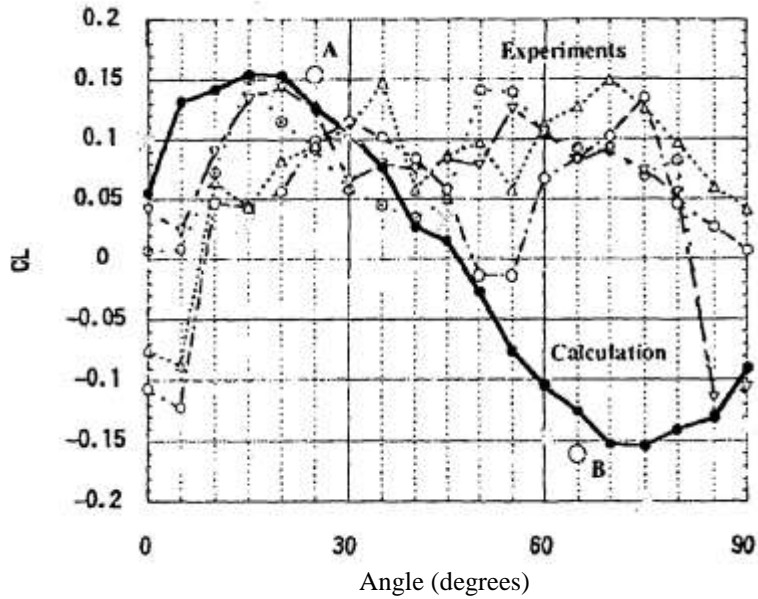


Figure 2.21 - Lift coefficients for baseball with rifle spin. Various initial orientations are plotted.

The high points relate to when a large portion of the stitches are in the critical zone of the boundary layer.

Recently, Constantinescu (30) developed a numerical model to study flow over a sphere to simulate separation of flow in the boundary layer. Constantinescu notes that modeling massive flow separation on an object is one of the most difficult CFD challenges.

Section 2.6 – Concluding Remarks

Extensive research over the last two hundred years has been conducted in the field of determining sphere aerodynamics. Lift and drag experiments on smooth spheres, rough spheres, dimpled balls, and various sports balls have been conducted to reveal more information on the Magnus effect and drag force fluctuations. In general, past research has found that for the high Reynolds region, spheres and sports balls can have a C_D approximately from 0.1 to 0.5 depending on the Reynolds number, geometry, and

surface roughness. C_L values were observed at greater than 0.4 with angular velocities achieving 6000 rpm.

While most of the research has been conducted by analyzing the fluid around a stationary object, few experiments have been conducted on actual balls in flight. In the past it has been much easier to pass fluid around an object (i.e. a wind tunnel), and record the fluid properties than it is to push the object through the fluid and record its behavior. However, the object's fluid properties may behave differently if it were not constricted in the fluid.

In the last two decades improvements in the video capturing devices and tracking software have enabled tracking pitched baseballs during game play. Using the tracking software, rotation and displacements of the ball, lift and drag forces were computed. Results involved with in flight baseballs conflict in two ways: the magnitude of their drag crisis, and the Reynolds number that the crisis begins. Research involving balls in actual flight is limited.

The following describes a numerical 3-D model and an experimental setup to measure lift and drag on balls in situ. Using high speed light gates to measure time and displacement of the objects, accurate measurements of ball aerodynamics were made while spin, orientation, and surface roughness were varied.

Chapter III – Numerical Determination of Lift and Drag

Section 3.1 – Numerical Model Introduction

A numerical model was developed using commercial computational fluid dynamics software (Fluent 6.3.26). Both two and three dimensional models of a smooth sphere and baseball were considered. Most numerical research has been conducted in 2D, so the three dimensional model was chosen. The purpose of the model was to measure the aerodynamic properties of a ball while changing air speed, surface roughness, and rotational speed.

Section 3.2 – Geometry and Meshing

Two balls were modeled – a smooth sphere, and an NCAA baseball. Geometry and meshing of the sphere was made using the geometry tools in Gambit. The geometry of the baseball, however, was too complex for Gambit and was simpler to construct in SolidWorks. Modeling the stitches on the baseball needed to be simplified by forming one continuous raised seam instead of each individual thread. Later, a roughness was applied to the seam to imitate a rough stitch (see Figure 3.1). The SolidWorks geometry was imported as a STEP file into Gambit where the surfaces were defined.

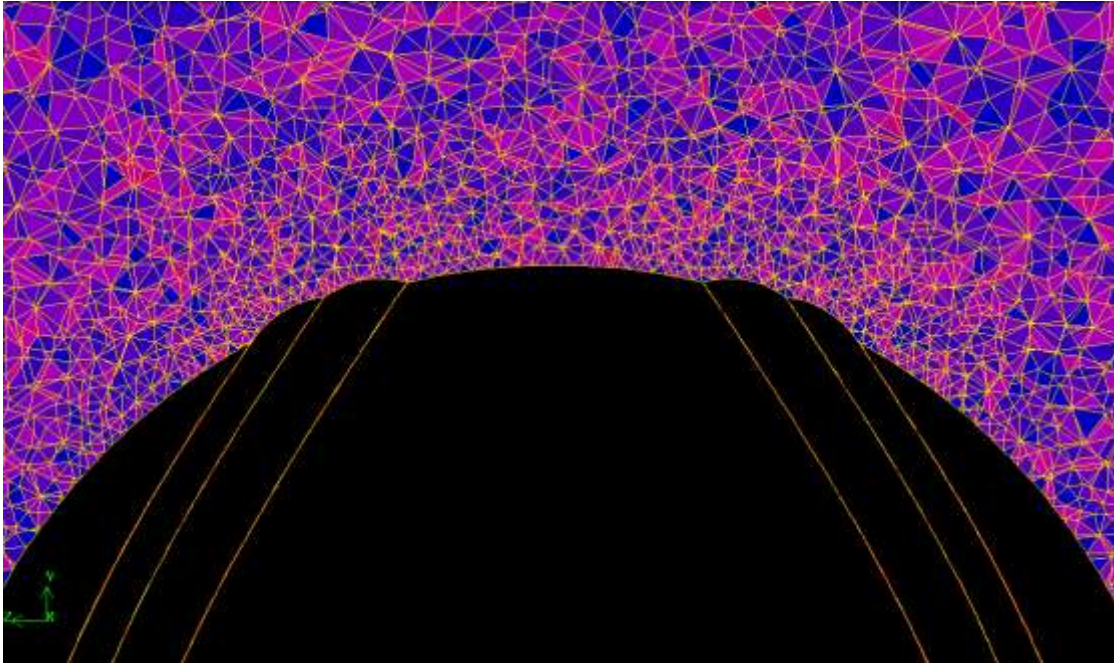


Figure 3.1 - Geometry and mesh around NCAA baseball.

Once the 3-D geometry was constructed in Gambit, the balls were meshed. To properly mesh the ball and obtain a solution in a timely manner, four zones were created each having different density of mesh elements (see Figure 3.2). The first zone was created using the boundary layer meshing tool. The boundary layer height was chosen by trying to achieve $y^+ = 1$ at the balls wall. The boundary layer consisted of 20 small layers, with each layer being 10% larger than the previous (see Figure 3.5). Once outside the boundary layer, a second zone resembling a cylinder around the ball was created. This zone spanned three ball diameters wide and 8 diameters long. A finer Tetrahedral/Hybrid mesh was needed in this zone since this is where the wake of the separation would take place (see Figure 3.3 and Figure 3.4). A size function was placed such that the mesh would stay very small next to the ball and get larger towards the outer boundary of the zone. The third zone was similar to the second, only the size function was larger. This zone was 7 ball diameters wide and 22 diameters long. Finally the

fourth zone was similar to the third and had an even larger size function. The zone spanned 14 diameters wide and 28 diameters long.

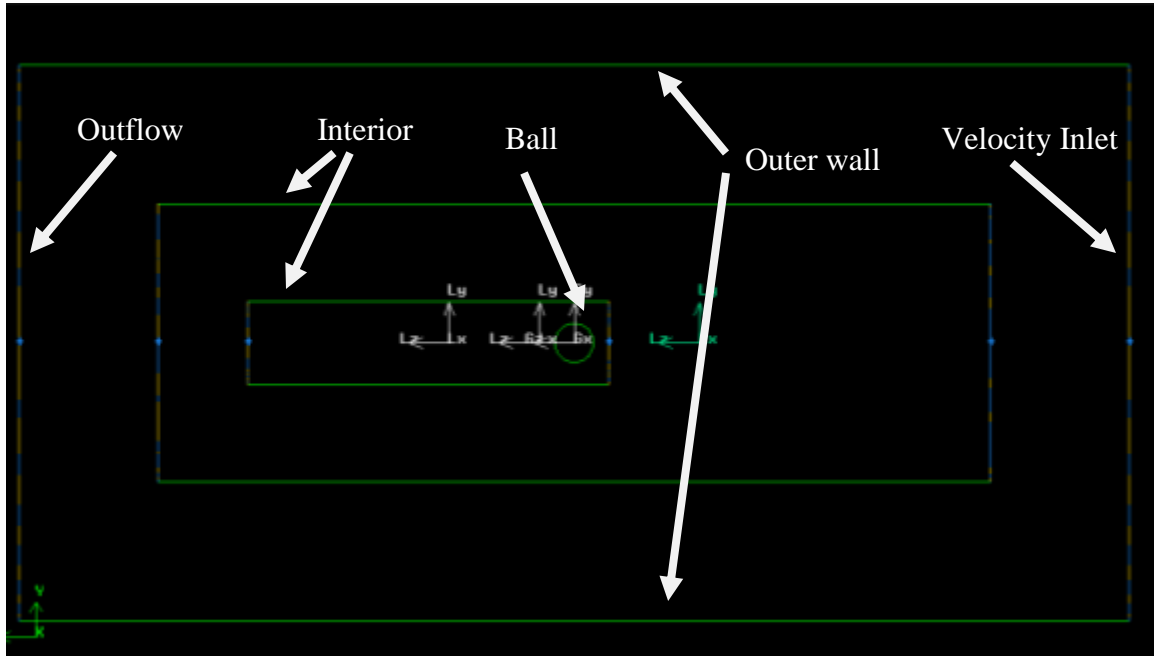


Figure 3.2- Geometry of mesh zones.

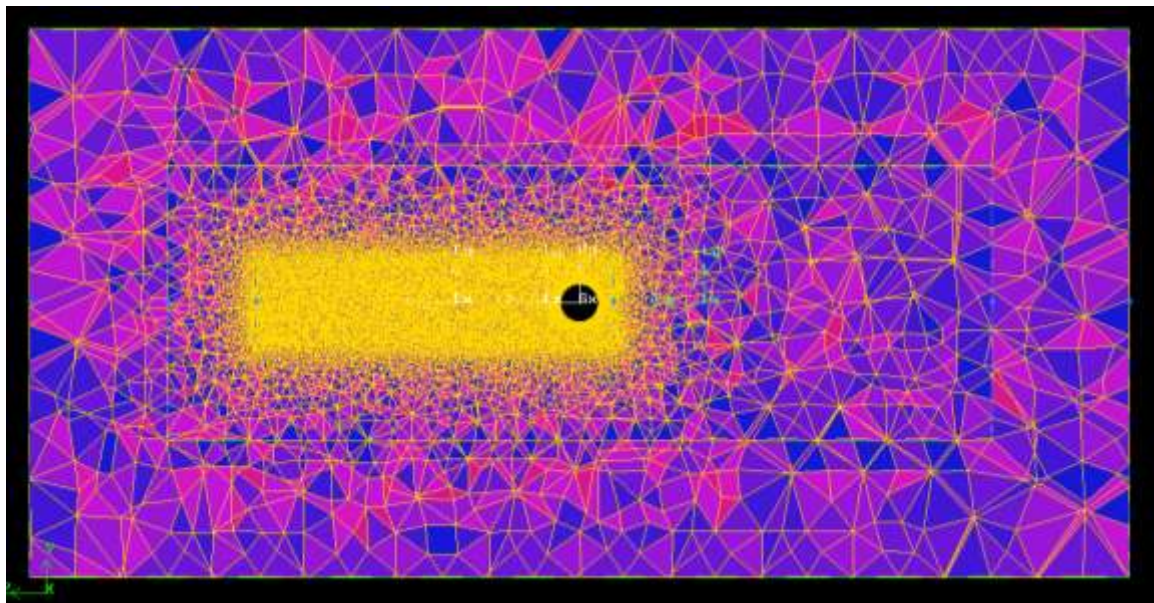


Figure 3.3 - Cross section of meshed zones.

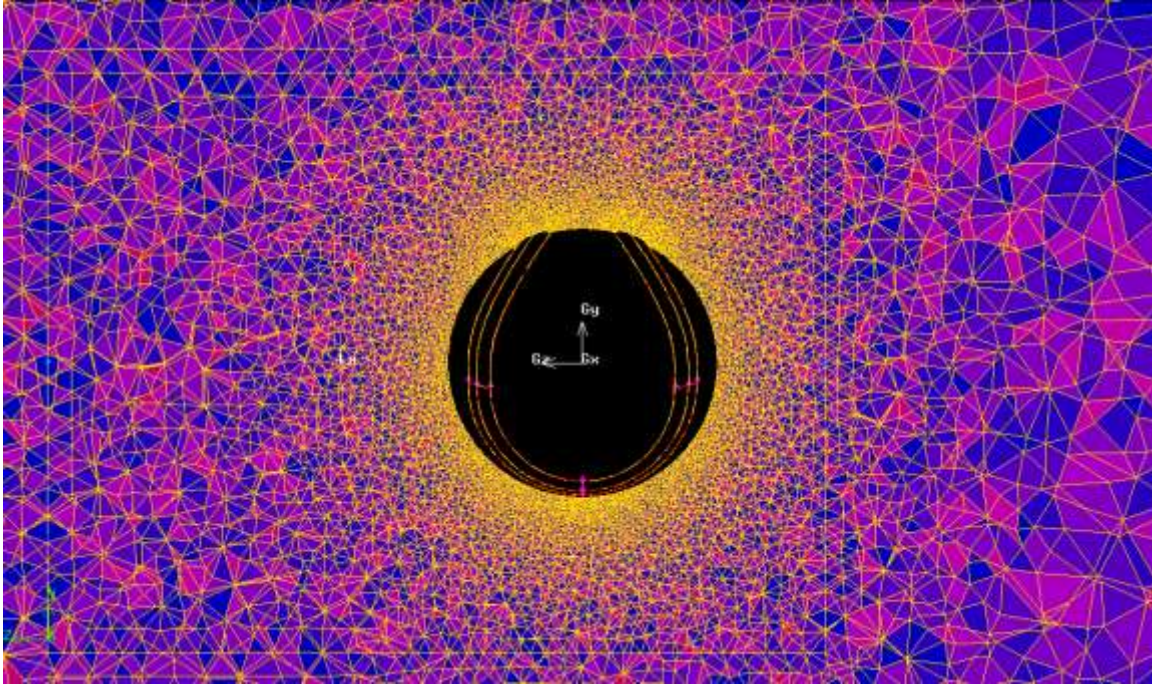


Figure 3.4 - Cross section of meshed baseball.

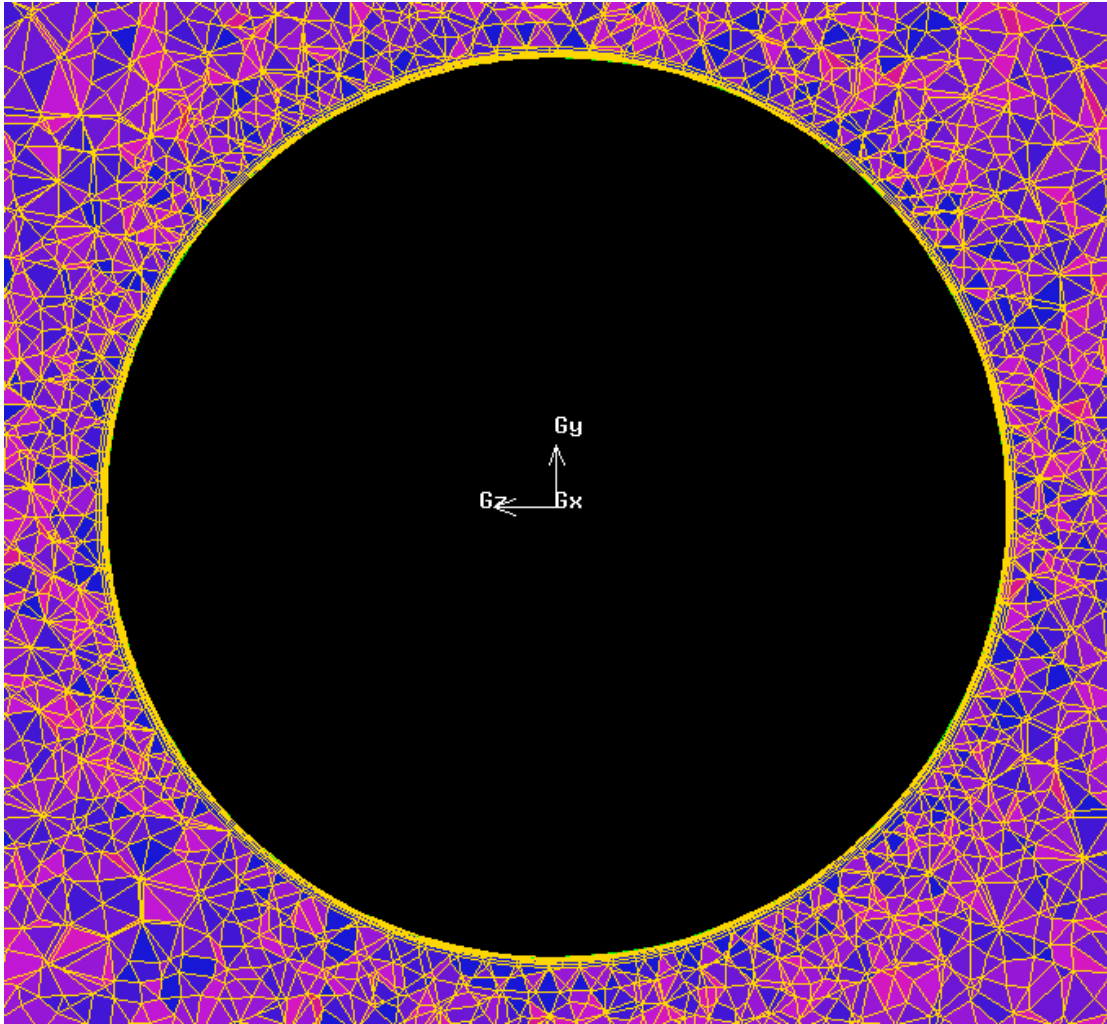


Figure 3.5 – Sphere cross section of meshed zones (close up of ball).

After completing the mesh, surfaces needed to be joined and defined. This was important such that the baseball threads could be addressed independent of the rest of the ball. The final defined mesh was exported for Fluent.

Section 3.3 – Boundary Conditions and Solver

Fluent was used to carry out the finite element analysis. The mesh was imported. A Realizable k-epsilon (2 equation) model was used (see Figure 3.6). The transport equations used in the model are (31)

$$\frac{\partial}{\partial t}(\rho k) + \frac{\partial}{\partial x_j}(\rho k u_j) = \frac{\partial}{\partial x_j} \left[\left(\mu + \frac{\mu_t}{\sigma_k} \right) \frac{\partial k}{\partial x_j} \right] + G_k + G_b + \rho \epsilon - Y_M + S_k \quad (3.1)$$

$$\frac{\partial}{\partial t}(\rho \epsilon) + \frac{\partial}{\partial x_j}(\rho \epsilon u_j) = \frac{\partial}{\partial x_j} \left[\left(\mu + \frac{\mu_t}{\sigma_\epsilon} \right) \frac{\partial \epsilon}{\partial x_j} \right] + \rho C_1 S_\epsilon - \rho C_2 \frac{\epsilon^2}{k + \sqrt{v \epsilon}} + C_{1\epsilon} \frac{\epsilon}{k} C_{3\epsilon} G_b + S_\epsilon \quad (3.2)$$

where

$$C_1 = \max \left[0.43, \frac{\eta}{\eta + 5} \right], \eta = S \frac{k}{\epsilon}, S = \sqrt{2 S_{ij} S_{ij}}$$

In this equation ϵ is the dissipation rate, k is the turbulent kinetic energy, G_k is the generation of turbulence kinetic energy due to the mean velocity gradients, G_b is the generation of turbulence kinetic energy due to buoyancy, and Y_M is the contribution of the fluctuating dilatation in compressible turbulence to the overall dissipation rate. $C_{1\epsilon}$ is a constant, σ_k and σ_ϵ are the turbulent Prandtl numbers for k and ϵ , and S_k and S_ϵ are user-defined source terms.

Boundary conditions pertaining to fluid flow were ‘velocity inlet’ at the inlet side of the mesh and ‘outflow’ for the outlet side of the mesh. The ‘velocity inlet’ speed was user defined and air was allowed to only exit through the outflow surface. The interior surfaces were set to ‘interior’ and the ball and threads were set to ‘wall’. Using ‘standard wall functions’ the walls could be defined as a stationary or rotating boundary condition with a no slip shear condition. Surface roughness and roughness height were also defined for the ball wall.

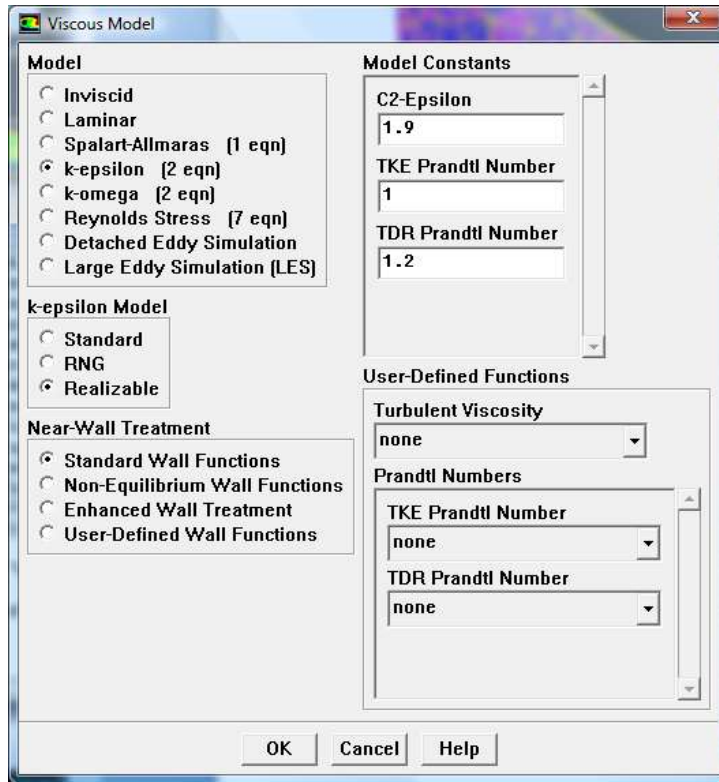


Figure 3.6 - Screen shot of viscous model in Fluent.

The conditions were initialized and air was passed around the sphere.

Section 3.4 – Numerical Results

Several iterations of the baseball model were conducted. Drag results were in the range of those found in experiments, however as Reynolds number was increased or decreased for a given mesh the drag trend did not fit experimental data. For Reynolds numbers which did produce a similar result to experimental results, plots were made of particle path lines over the ball. In Figure 3.7, path lines were plotted for free stream velocity of 65 mph without rotation. The flow lines do show turbulence in the boundary layer causing separation on the backside of the ball. The quantitative results showed solutions to be inaccurate over a wide range of Reynolds numbers. This meant that the mesh gave approximate solutions at one specific velocity for a given mesh. Using the

same mesh while changing boundary conditions yielded an inaccurate solution. The mesh had to be continuously changed if the velocity over the ball was changed. In Figure 3.8, path lines were plotted for free stream velocity of 50 mph with 200 radians/second angular velocity. The plot is showing the backside of the ball. Vortices formed off the lower half of the ball. The rotation directed the vortices downward causing a lift force upward.

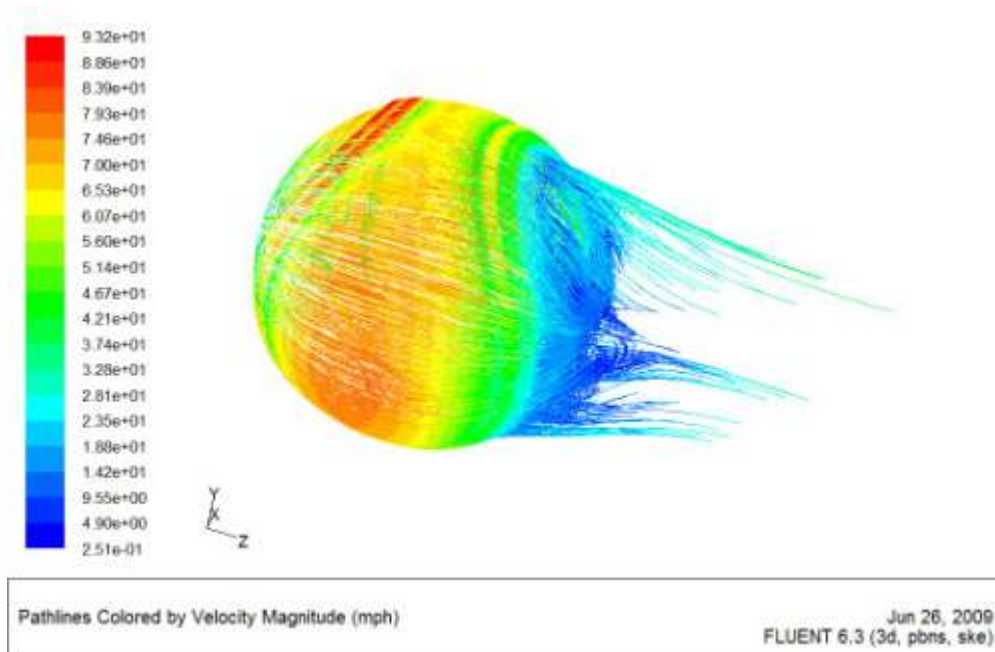


Figure 3.7 - Particle path lines over a baseball traveling at 65 mph.

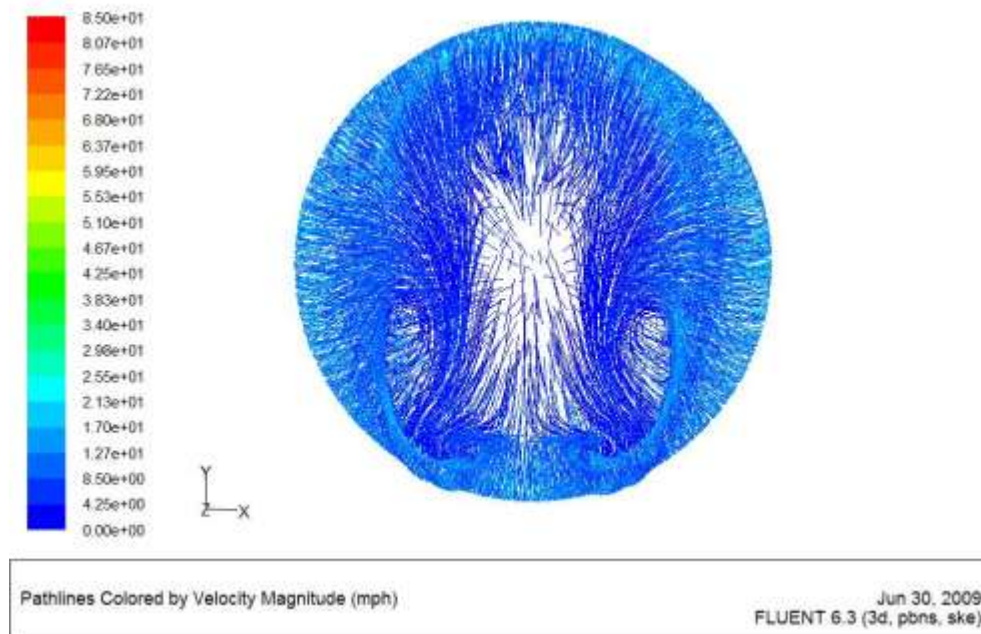


Figure 3.8 - Rear view of particle path lines over a baseball traveling at 50 mph with 200 radians/second angular velocity.

Several meshes, constants, and coefficients were used at various air velocities around the smooth sphere. Fluent was capable of determining drag related to pressure forces, but could not properly predict the separation point on the ball. Flow lines were never observed to separate at the 80 degree location, only at the 120 degree location. Drag curves for a smooth sphere showed decreasing drag as velocity increased, but did not show a drag crisis (see Figure 3.9). Changing mesh types did change C_D , but again the trend did not show a drag curve or correct magnitudes for a wide range of Reynolds numbers.

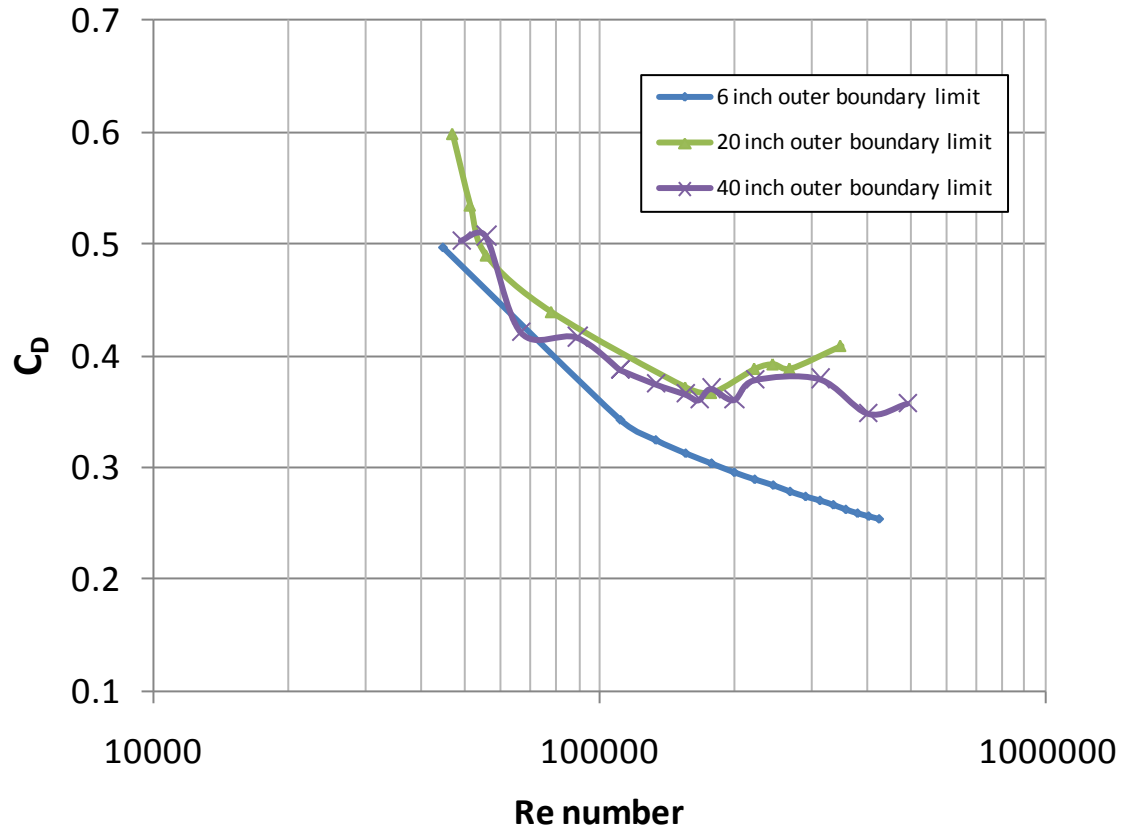


Figure 3.9 - Numerical model drag curves while varying the size of the outer boundary limit.

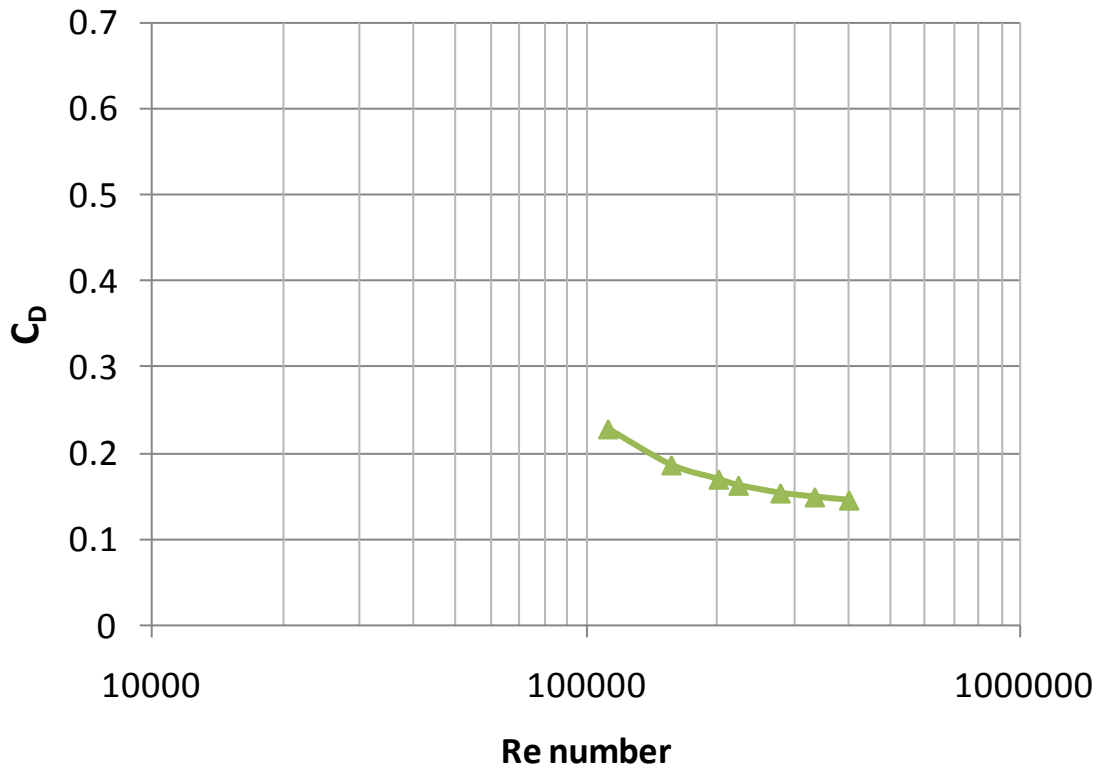


Figure 3.10 – Numerical model drag curve for smooth sphere.

Chapter IV – Experimental determination of lift and drag

The current experiment determined aerodynamic properties of sports balls in situ. Using light gates and computer software, balls were projected up to 16 feet through static air where velocity and accelerations were determined and flight properties calculated.

Section 4.1 – Experimental Setup

Sports balls were projected in a lab setting through static air. Two light boxes were constructed out of 45mm Bosch Aluminum framing. Each box had an opening for the projectile to pass through of 15 inches by 19.5 inches. This opening allowed enough room for a ball to pass through without impacting the box walls.

Inside each light box were three sets of light gates (ADC iBeam) labeled Gate1, Gate2, and Gate3 (see Figure 4.1 and Figure 4.2).



Figure 4.1 - Light gates configuration inside the light box.

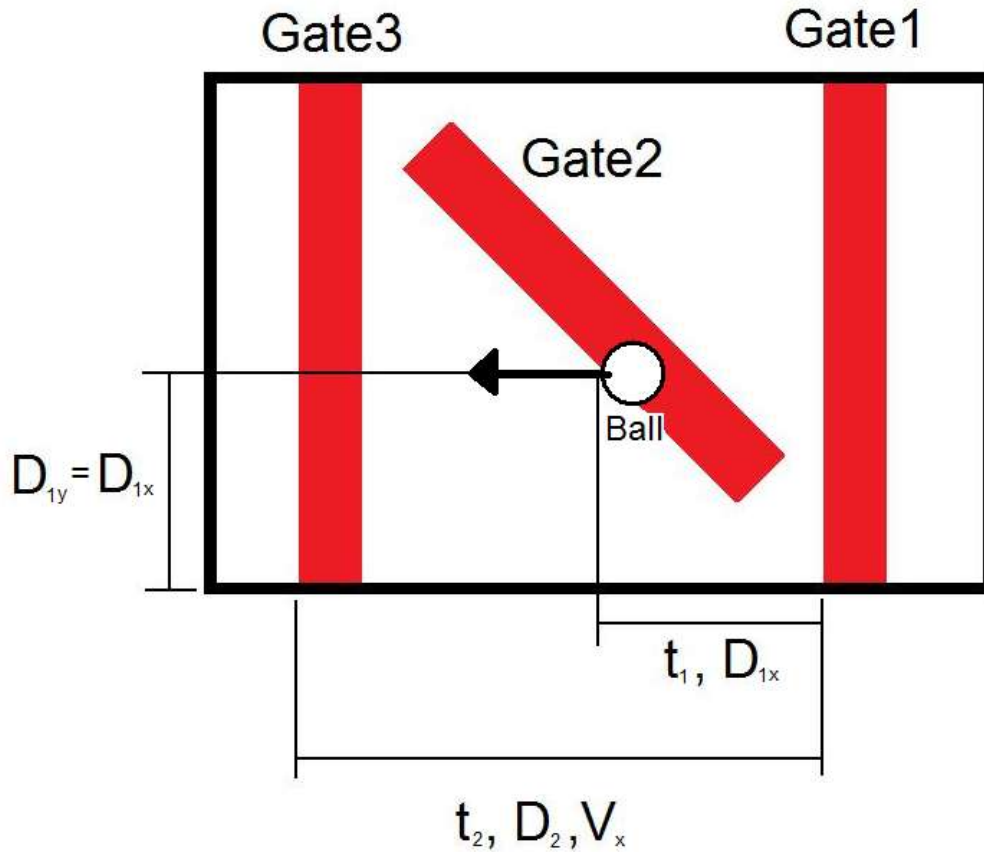


Figure 4.2 - Schematic of light box setup.

The gate signals were timed with an 80 MHz NI-PCI 6602 data acquisition board. A LabVIEW program was written to convert the signals to speed and vertical location for each light box.

Two sets of light gates, Gate1 and Gate3 were mounted vertically and were placed 16.5 inches apart, D_2 . This distance provided enough length between the gates to obtain a velocity. Velocity was found by taking the distance between these gates and dividing by the time, t_2 , an object took to pass between them. Gate2 was centered and oriented at 45 degrees between the two vertical gates. This gate was used to calculate the position of the ball inside the light box. Using the time from Gate1 to Gate2, t_1 , and multiplying by

the velocity of the ball, V_x , the horizontal distance, D_{1x} , to the ball inside the box was found as

$$D_{1x} = D_{1y} = V_x t_1 \quad (4.1)$$

Since Gate2 was placed at a 45 degree angle, the horizontal and vertical distance to ball is the same (see Equation 4.1).

A pneumatic sabot style air cannon (Washington State University Sports Science Laboratory) was used to project sports balls with no rotation (see Figure 4.3). The ball was loaded into a polycarbonate sabot (see Figure 4.4), or cradle, in a specific orientation. The ball could then be loaded into the breech of the canon (see Figure 4.5).



Figure 4.3 - 1st light box and pneumatic cannon



Figure 4.4 – Baseball loaded into the polycarbonate sabot.



Figure 4.5 - Sabot placed in the cannon's barrel.

For each shot the pressure was released from the accumulator tank and the sabot was accelerated. A high speed camera operating at 1000 frames per second and 1/10,000 second shutter was used to record each shot leaving the cannon for verification of correct orientation and flight path (see Figure 4.6).



Figure 4.6 - Still frame shot of softball leaving the cannon at 90 mph.

Since the pneumatic cannon was only capable of projecting balls with no rotation, a three wheeled pitching machine (HomePlate by Sports Tutor, see Figure 4.7) was used to consider the effect of ball rotation. Different from two wheeled machines, the three wheeled machine had concave wheels. This allowed for less wear on the balls, a more consistent release out of the pitching machine, and a more predictable flight path. The three wheels were oriented 120 degrees apart from each other with the lower wheel aligned vertically (see Figure 4.8).



Figure 4.7 - Side view of three wheeled pitching machine.

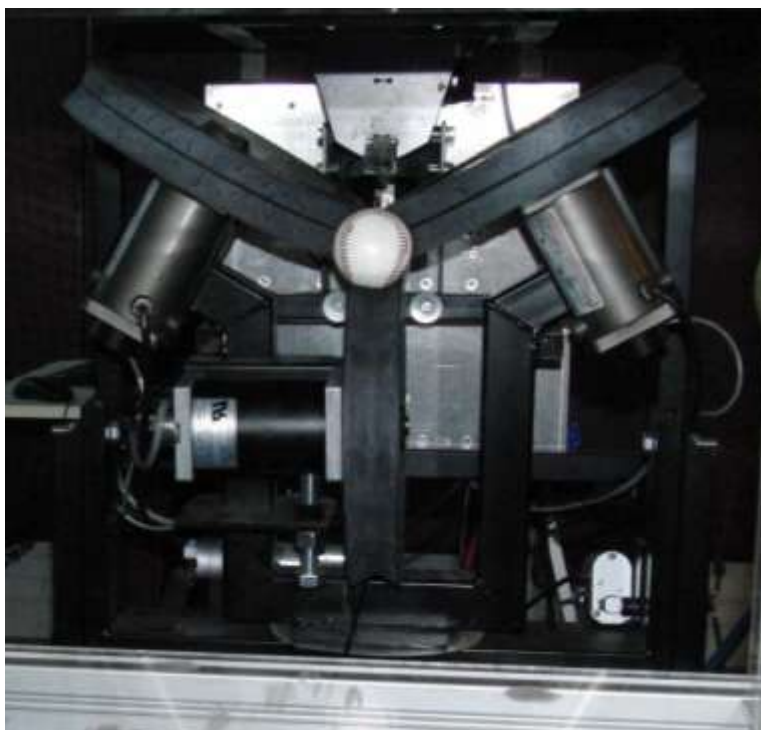


Figure 4.8 - Front view of the three wheeled pitching machine.

Since the three wheeled pitching machine was designed to throw any type of pitch, careful tuning of the two outer wheels to the same angular velocity was required to keep the balls' rotational axis horizontal. This was done by opening up the control panel (see Figure 4.9) and checking each axle's optical encoder to ensure each wheel was spinning at the correct speed. Wheel speed was adjusted by turning each wheel's potentiometer (see Figure 4.10). By speeding up the lower wheel independently of the upper wheels, backspin was placed on the ball. Each ball was placed in a specific orientation in the ball feeder. The ball was released from the feeder by pulling the stop pin and the ball rolled into the wheels. Once the ball was projected, a high speed camera was used to verify correct orientation. Later, this video was loaded into tracking software to determine angular velocity of each projection.

After the ball was released from either pitching device, it began its path through the light boxes. The light gates measured both the position and speed of the ball at two different locations along the ball's path (see Figure 4.11).



Figure 4.9 - Home Plate machine with control panel exposed.

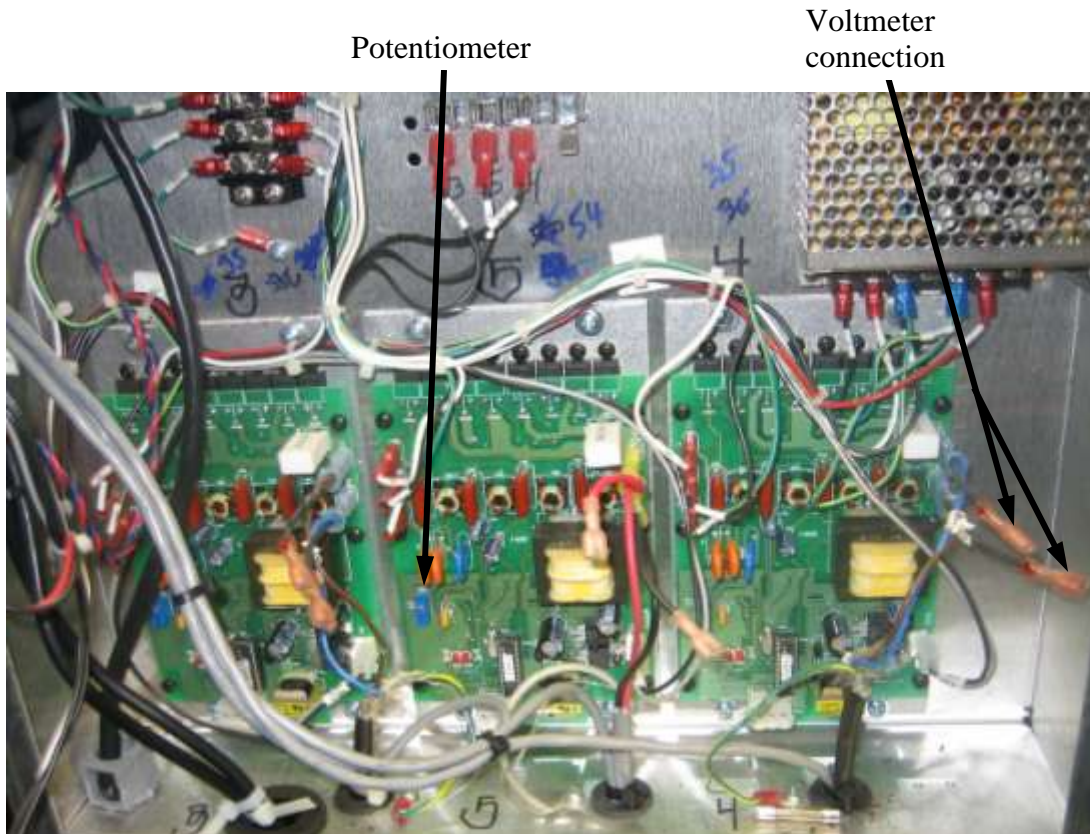


Figure 4.10 - Home Plate circuit board.

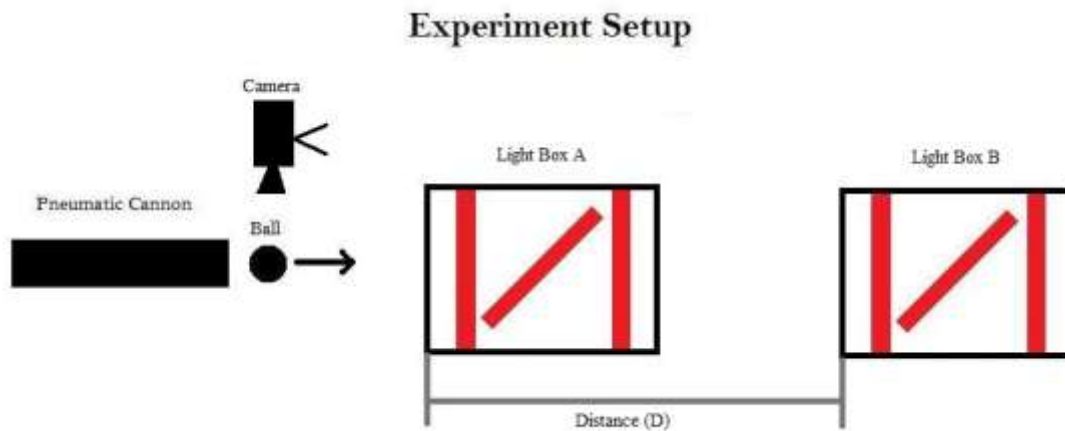


Figure 4.11 - Schematic of experimental setup.

Two light boxes were assembled identically. The first light box was squared to the pitching device using a tape measure and plumed using a bubble level. The second light box was placed downstream of the flight path, plumed using a bubble level, and squared to the first light box with a laser level (MP3 Laser Mark). A free standing

wooden funnel was fabricated to prevent balls from impacting, moving or damaging the second light box (see Figure 4.12). To align boxes using the laser level, the laser beam was initially directed down the inside wall of the first light box. Then the second box was moved into place so the laser beam was also directed down its inside wall.



Figure 4.12 - Light boxes and wooden funnel.

At higher pitch velocities the gates were placed farther apart (roughly 16 feet) to allow enough time for the ball to decelerate to make a recording of drag force. When projecting balls at slower velocities, the light boxes were moved closer together (roughly 10 feet) to prevent ball contact with the bottom of the second light box and large angled trajectories when passing through the box. Even projecting at high speed, the ball would have vertical drop due to gravity. To account for the drop the second light box was lowered relative to the first light box. The relative vertical distance was measured by

placing the laser level in the bottom of the first light box and directing it onto a scale mounted to the front of the second light box (see Figure 4.13). After subtracting the height of the laser level, a relative vertical displacement was found. Once both boxes were set, a measuring tape was used to find the final distance between the two light boxes.



Figure 4.13 - Scale mounted to front and aligned to the bottom of the box.

Section 4.2 – Uncertainty in Measuring Speed and Displacement with Light Gates

Drag was experimentally determined from change in velocity between two points and lift was determined from vertical displacement between two points (see Equation 4.2 and 4.8)). Therefore an uncertainty in the velocity and vertical displacement needed to be quantified to validate the precision, or repeatability, of the measurements that were made. The light gate emitters contained 32 infrared LEDs evenly spaced over 15 inches and the light gate receivers contained nine photo diodes spaced evenly along 15 inches. When

the ball passed through the curtain of light, the ball cast a shadow over the photo diodes and the receiver measured a voltage change.

To determine the uncertainty in velocity and vertical displacement, the light boxes were fixed together using bolts such that the outlet of the first box was mounted to the inlet of the second box (see Figure 4.14 and Figure 4.15)

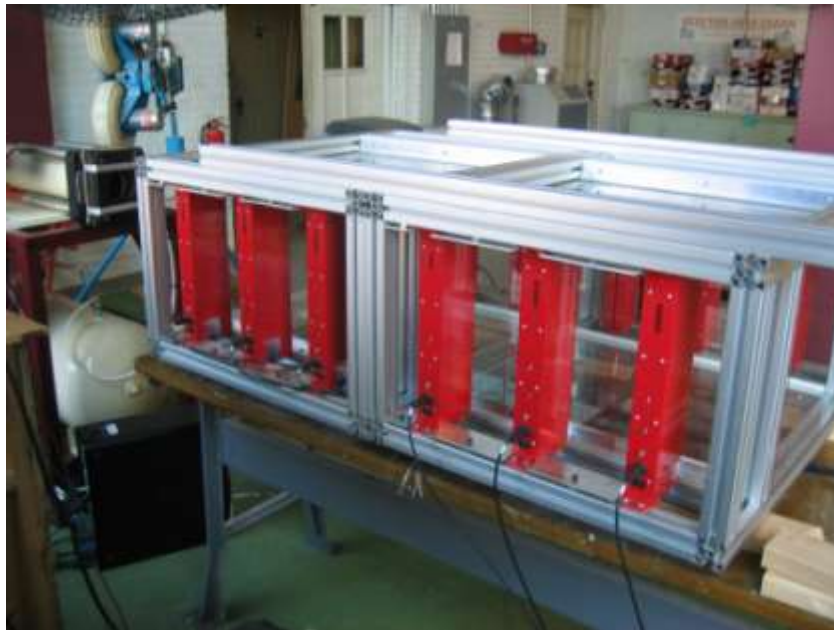


Figure 4.14 - Velocity repeatability test configuration.

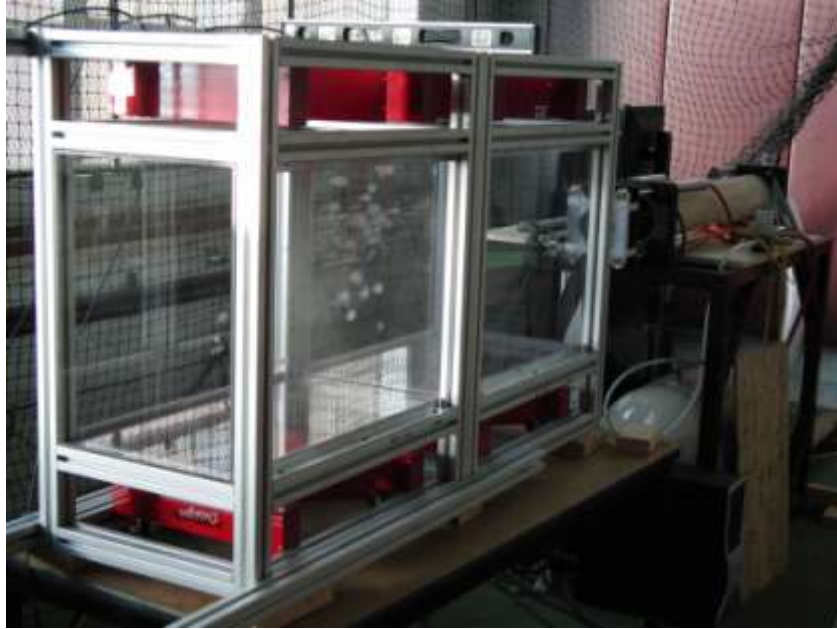


Figure 4.15 - Light box configuration during vertical calibration.

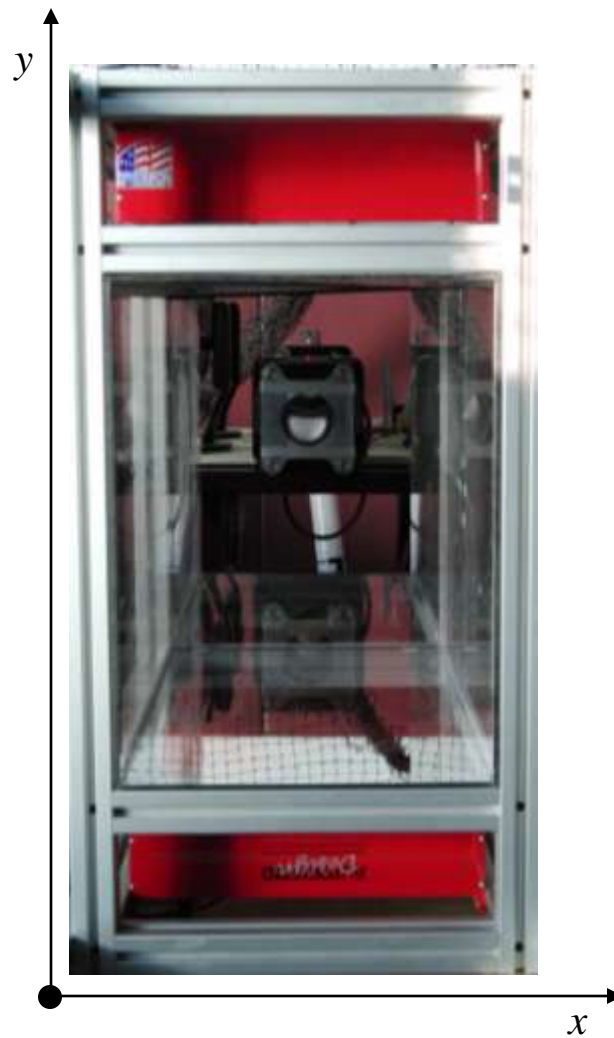


Figure 4.16 - Light box in calibration setup (with coordinates).

The first test was conducted to determine the velocity uncertainty if the individual light gates were spaced at 8.25 inches apart versus 16.5 inches apart. All six light gates were mounted vertically. Light gates LG1, LG2, and LG3 were each spaced 8.25 inches apart and similarly LG4, LG5, and LG6 were spaced 8.25 inches apart (see Figure 4.17 - Light gate configuration for velocity uncertainty. Figure 4.17). For each shot this arrangement allowed velocities to be calculated at an 8.25 inch spacing and a 16.5 inch spacing. MLB baseballs in the parallel orientation were shot through the light gate configuration. Velocity measurements were compared between Light Box A and B (see Figure 4.18): velocity LG1-LG3 was compared to velocity LG4-LG6; velocity LG1-LG2

was compared to LG4-LG5; and velocity LG2-LG3 was compared to LG5-LG6. At the 16.5 inch spacing, the bias error was 0.1 mph with a precision error of 0.025 mph (standard deviation). At the 8.25 inch spacing the bias error was 0.19 mph with a precision error of 0.038 mph. Reducing the gap between light gates increased bias error by 190%.

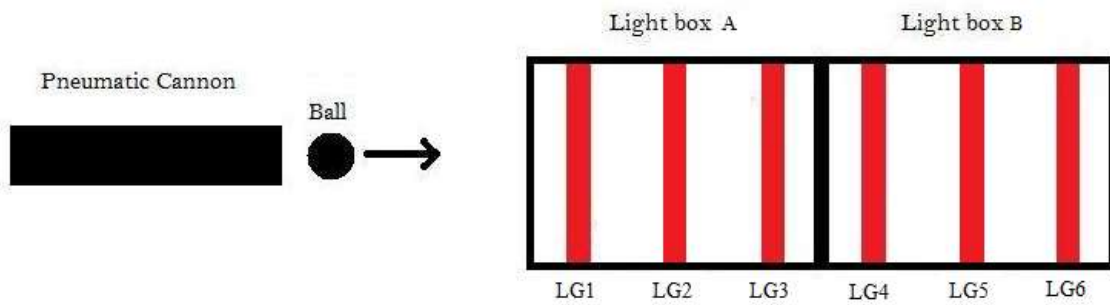


Figure 4.17 - Light gate configuration for velocity uncertainty.

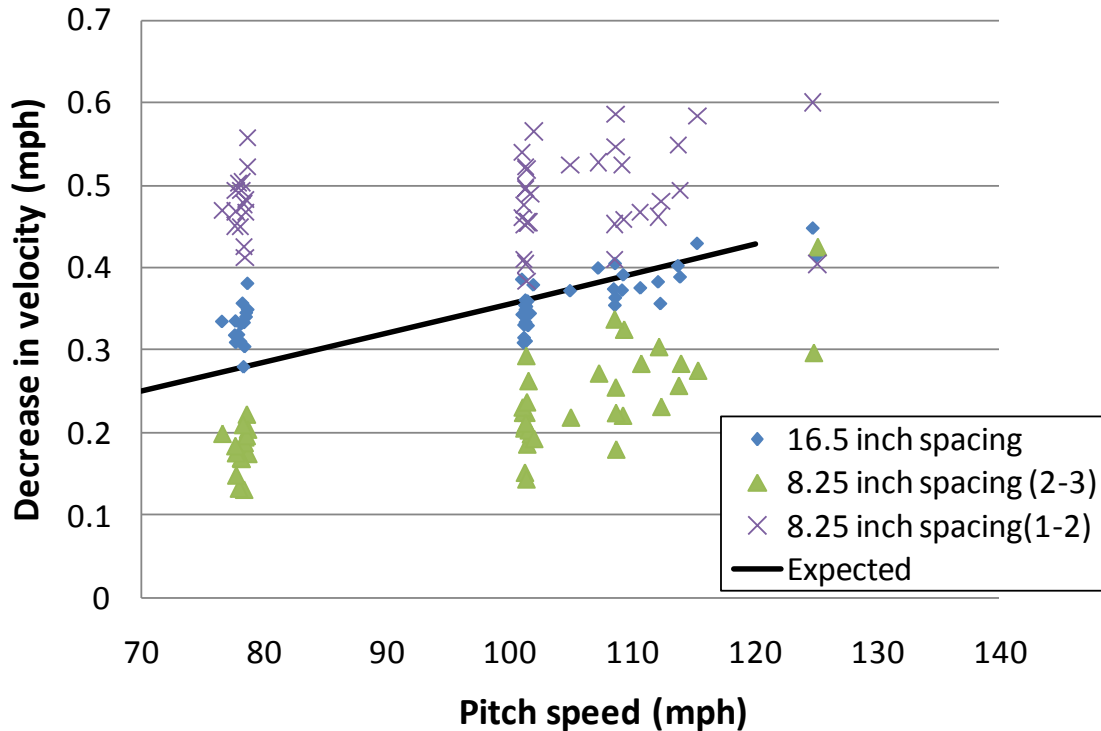


Figure 4.18 - Velocity repeatability between light boxes.

The light boxes were turned on their side for the vertical displacement calibration test. This eliminated displacement of the ball due to gravity. The boxes were squared with the pitching device and plumbed using a bubble level. A smooth sphere was shot horizontally through the boxes which measured speed and horizontal displacement. A perfect recording of displacement would have been zero.

Three tests were conducted to analyze possible scenarios the ball might have encountered while traveling through the light boxes. The first scenario held velocity and y location constant while changing the x location of the light boxes (see Figure 4.19). This verified that diodes measured voltage consistently for small changes in the ball's horizontal position. Variation in displacement did not show a trend and showed displacements up to 0.15 inches. Similarly the second scenario held velocity and

horizontal placement constant while changing vertical placement (see Figure 4.20). Variation in displacement while changing y location did show a trend that as the ball moved closer to the emitters. More displacement was observed with a maximum displacement of 0.17 inches. The final scenario held x and y location constant while changing velocity (see Figure 4.21). This was to verify that the sample rate was high enough to have repeatable data at both high and low speeds. No trends were found during this test and a maximum displacement of 0.17 inches was found.

The same three scenarios were plotted against decrease in velocity, Figure 4.22, Figure 4.23, and Figure 4.24 respectively. The largest precision error (0.06 mph) was observed when the ball location was moved closer two inches closer to the emitters.

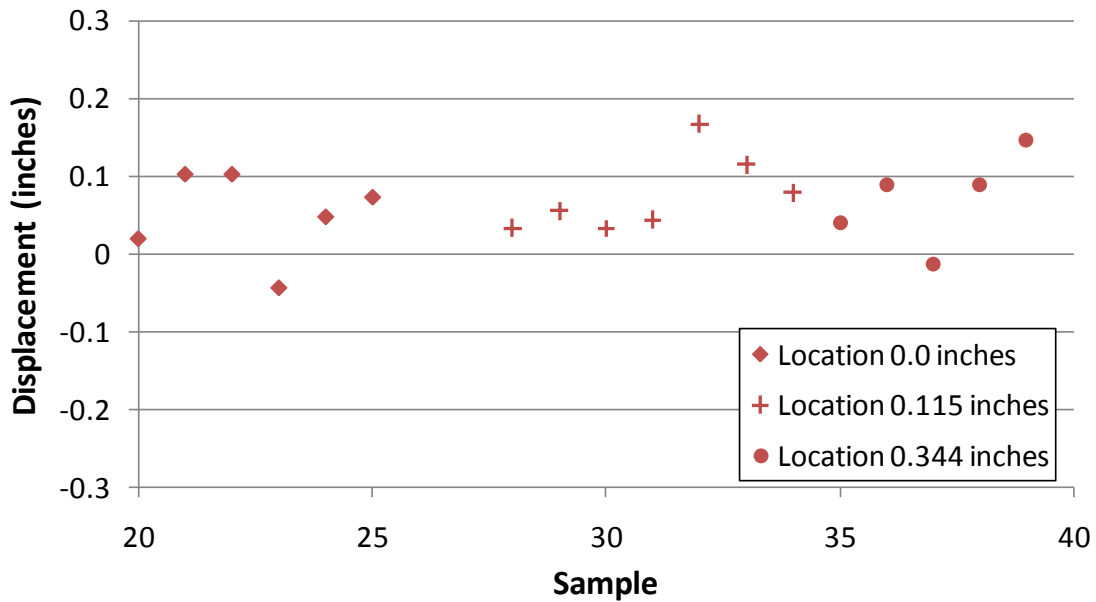


Figure 4.19 - Constant velocity and y location while changing x location.

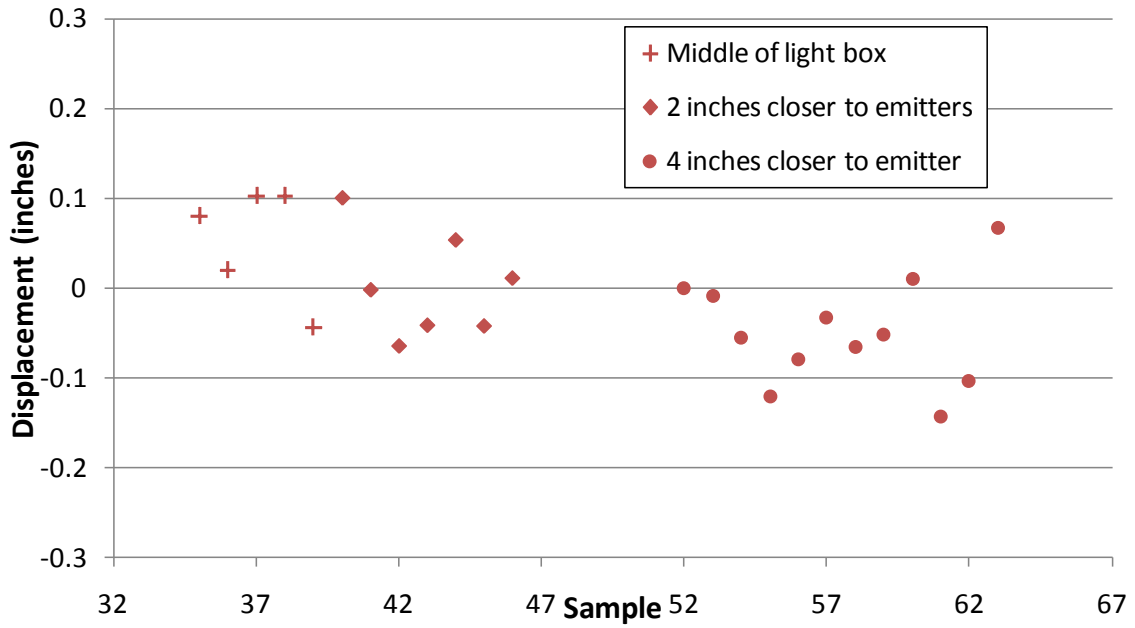


Figure 4.20 - Constant x location and velocity, while changing y displacement.

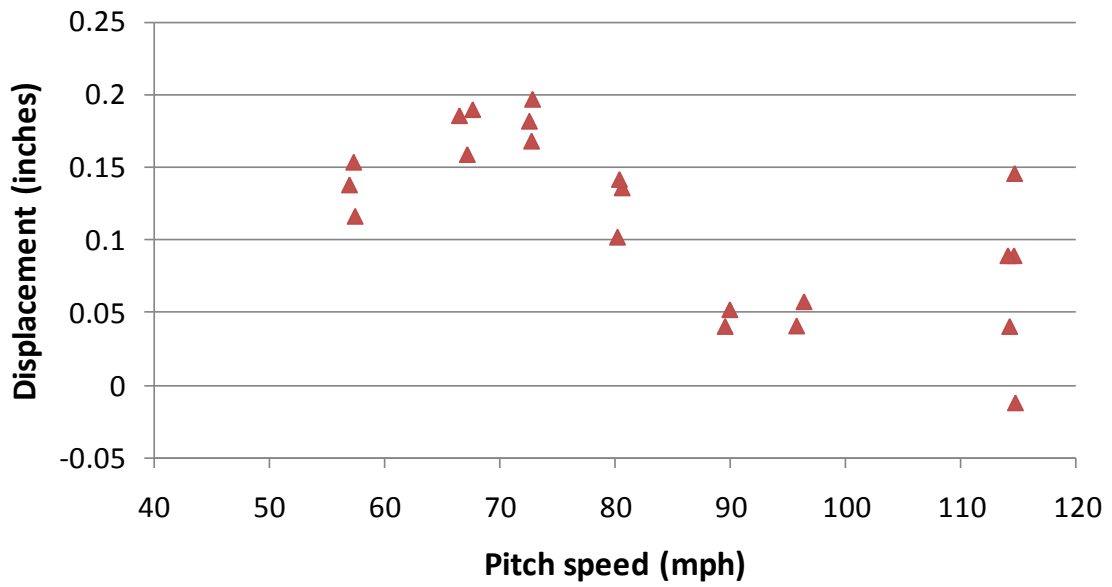


Figure 4.21 - Constant x and y location while changing velocity.

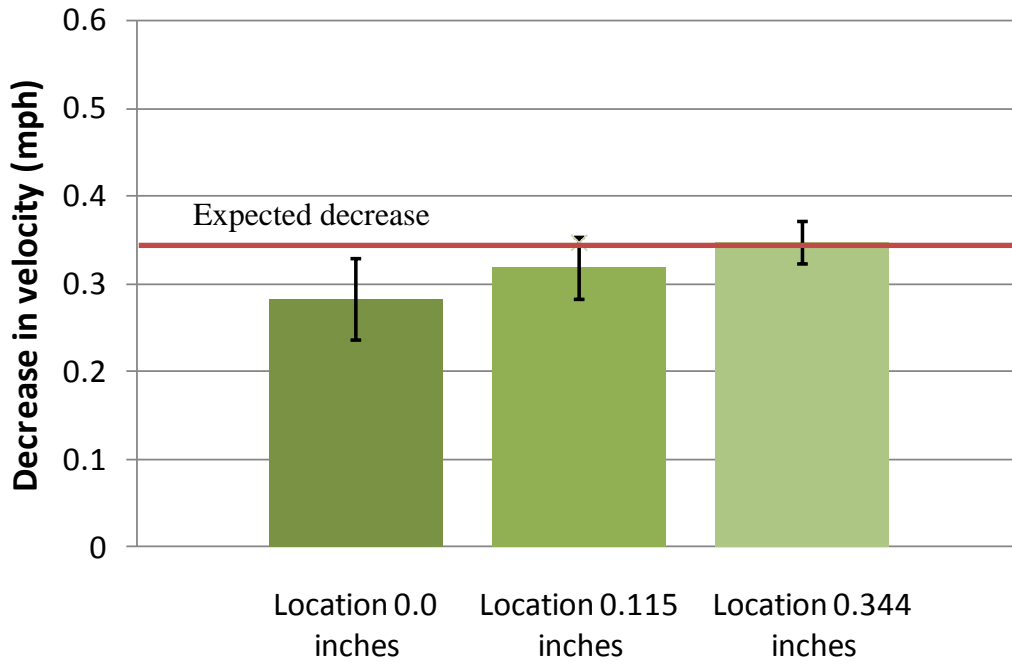


Figure 4.22 - Constant velocity and y location while changing x location. Black bars show precision error (standard deviation). At least six samples were used in each data set.

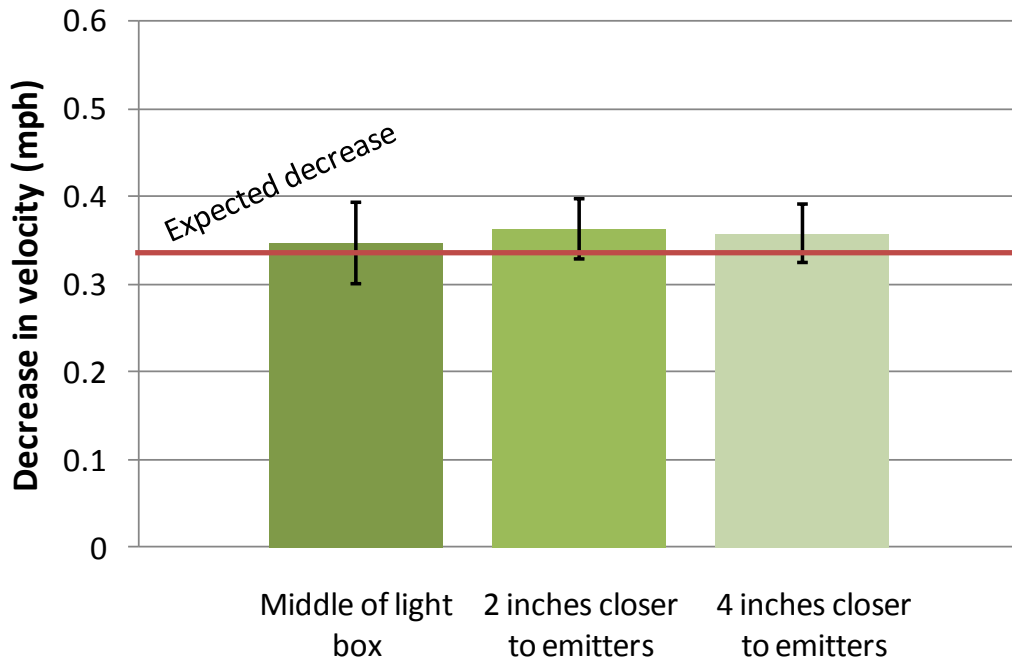


Figure 4.23 - Constant x location and velocity, while changing y displacement. Black bars show precision error (standard deviation). At least six samples were used in each data set.

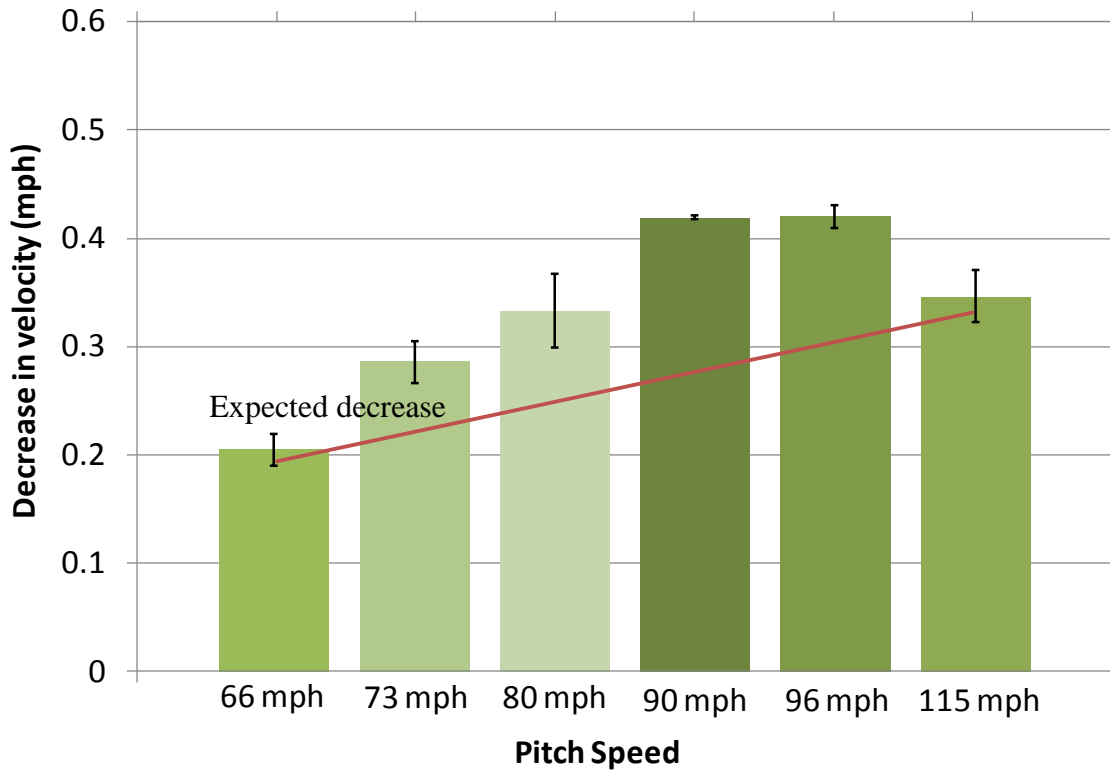


Figure 4.24 - Constant x and y location while changing velocity. Black bars show precision error (standard deviation). At two samples were used in each data set.

Section 4.3 – Samples

Each ball’s weight, diameter, average stitch height (k_h), average major surface roughness height were measured (see Table 4.1). Drag was obtained for nine different sphere types which included smooth acrylic spheres, smooth soft rubber spheres, dimpled pitching machine balls, NCAA baseballs (raised seam), MLB baseballs (flat seam), 11 inch softballs (raised seam), 12 inch softballs (flat seam), golf balls, and cricket balls. Lift forces were obtained for three different sphere types which included NCAA baseballs, MLB baseballs, and dimpled pitching machine balls.

Table 4.1 - Sample types and specifications

Sphere Type	Number of Samples used	Average Diameter (in)	Average Weight (oz)	Average Surface Roughness Height k_s (μin)	Seam or dimple Height k_h (in)	k_h/d	k_s/d
Smooth Sphere (Acrylic, polished)	2	2.99	9.95	1.2	NA	NA	4.01E-07
Smooth Sphere (Soft rubber)	2	3.94	7.08	16.1	NA	NA	4.09E-06
Dimpled Pitching Machine Ball	13	2.86	4.87	75	0.046	1.61E-02	2.62E-05
NCAA Baseball (raised seam)	21	2.84	5.07	75	0.042	1.48E-02	2.64E-05
MLB Baseball	24	2.88	5.14	77	0.012	4.17E-03	2.67E-05
12 inch Softball (raised seam)	6	3.86	6.87	83.3	0.018	4.66E-03	2.16E-05
11 inch Softball	6	3.5	6.19	52.5	0.068	1.94E-02	1.50E-05
Golf Ball	3	1.686	1.62	7	0.004	2.37E-03	4.15E-06
Cricket Ball	1	2.859	5.69	79	0.046	1.61E-02	2.76E-05

The pneumatic cannon allowed velocities of balls to range from 38 mph to 140 mph. The three wheeled pitching machine allowed velocities of balls to range from 60 mph to 99 mph with an angular velocities from 18 rpm to 4730 rpm.

NCAA baseballs, MLB baseballs, 12 inch softballs, and cricket balls were used to test how stitch orientation affected aerodynamic properties. Two stitch orientations, parallel and normal, were used (see Figure 4.25).

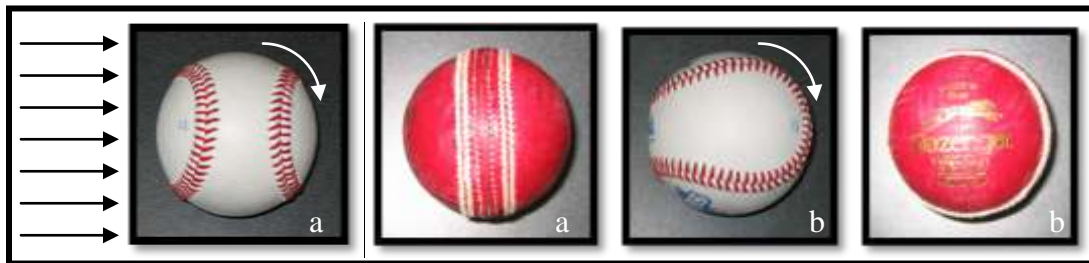


Figure 4.25 - Diagram showing the normal/4-seam (a) and parallel/2-seam (b) orientations. Black arrows indicate the airflow direction, white arrows indicate the ball rotation axis.

The parallel orientation could be described as having the majority of the stitches or seams parallel with the airflow. The normal orientation could be described as have the majority of the stitches perpendicular to airflow.

Section 4.4 – Experimental procedures

Two different procedures were used to take data with the pneumatic cannon and the three wheeled pitching machine. The procedures for taking samples can be found in Appendix One.

Section 4.5 – Experimentally determining drag

Drag force can be expressed as the mass multiplied by the deceleration of the object. Pressure and shear forces caused by fluid viscosity slow the ball down. To find the deceleration, two velocities in the object's trajectory needed to be calculated.

Deceleration was found from the kinematic equation (32)

$$a_D = \frac{V_{Ax}^2 - V_{Bx}^2}{2D} \quad (4.2)$$

where V_{Ax} was the velocity at Light Box A, V_{Bx} was velocity in the x direction at Light Box B, and D was the horizontal distance between them. Vertical velocity was added to the balls trajectory due to gravity by

$$V_y = gt \quad (4.3)$$

where t is the time between light gates. At low pitch velocities, the trajectory angle in Light Box B was up to seven degrees. The drag force directly opposes the velocity vector at any given position in the ball's trajectory. This complicated finding a_D as its

direction changed along its path. Trajectories were calculated by finding the instantaneous velocity, horizontal position, x , and vertical position, y , of the ball using

$$V(t) = V_0 - \sum a(t)\tau \quad (4.4)$$

$$x(t) = x_0 + \sum V_x(t)\tau \quad (4.5)$$

$$y(t) = y_0 + \sum V_y(t)\tau \quad (4.6)$$

where τ is a specified time constant. A solver function in Excel was used to iterate by changing C_D such that the initial velocity and final V_{Bx} velocity matched what was recorded from the light gates. A series of C_D were solved using this method. These drag results were compared to drag assuming constant deceleration (Equation 4.2) which used the velocity, V_{Bx} , obtained directly from Light Box B. The average differences in C_D between the two methods were less than 3%. Therefore, V_{Bx} was used to calculate C_D .

The drag force was found from the product of the ball mass and a_D . The drag coefficient was then found using Equation 2.2. Barometric pressure was found to change less than 1 inHg over the entire duration of the experiment. This change in pressure affected the drag by less than 2.8% and therefore was neglected.

The added mass fluid to an accelerating body was considered. The force of drag on a spherical accelerating body can be simplified as (7)

$$F = \frac{2}{3}\pi r_0^3 \rho \frac{dU}{dt} \quad (4.7)$$

If the sphere is given a virtual mass of

$$(\rho_0 + 0.5\rho)V \quad (4.8)$$

where V is the volume of the sphere, the added mass can increase the coefficient of drag by 0.08%. If the virtual mass was to reduce by 10% from Light Box A to B (since the

average deceleration of the object is roughly 10% between the light boxes) the drag would decrease approximately 0.01%.

The average uncertainty in C_D was found to be 0.05.

Section 4.6 – Experimentally determining lift and angular velocity

Lift can be expressed as the mass of an object multiplied by the acceleration of the object's motion perpendicular to its direction. Three vertical positions in the object's trajectory needed to be measured to find acceleration due to lift. The first position was the height of the pitching machine, and the second two were the displacements measured by the light boxes. Acceleration between the two light boxes was found from the kinematic equation (32)

$$a_L = \frac{2(D_{\Delta y} - V_{Ay} t_0)}{t_3^2} - g \quad (4.9)$$

where

$$D_{\Delta y} = D_{A1y} - D_{B1y} \quad (4.10)$$

is the vertical difference between the ball at the two light boxes, V_{Ay} is the initial vertical velocity at Light Box A, t_0 is the time taken from the release of pitching machine to Light Box A, t_3 is the time the ball takes to travel between the light boxes, and g is gravity. V_{Ay} was found from

$$V_{Ay} = V_{Ax} \tan(\alpha) \quad (4.11)$$

where α is the angle of projection of the ball after exiting the pitching machine. The angle of projection was found from

$$\alpha = \arctan\left(\frac{D_{Py}}{D_{Px}}\right) \quad (4.12)$$

where D_{Py} is the vertical height of the pitching machine and D_{Px} is the horizontal distance from the pitching machine to the ball's position in Light Box A. A scatter plot of the variation in angle of projection versus angular velocity (Figure 4.26) showed a range of angles from -0.038 to 0.0057 radians or -2.2 to 0.32 degrees. As angular velocity increased, the angle of projection became more consistent.

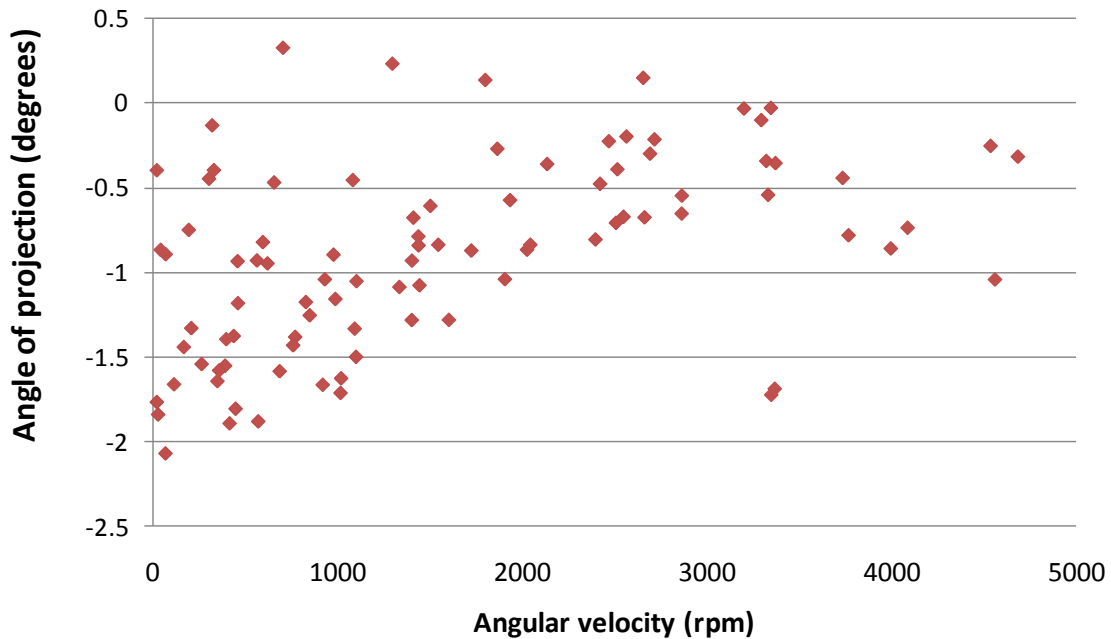


Figure 4.26 - Variation of angle of projection while pitching machine was in one fixed location.

Once the acceleration from the lift of the ball was found, gravity was subtracted and the final acceleration was multiplied by the mass of the ball to obtain force of lift.

The lift force was used in Equation 2.1 to obtain a coefficient of lift.

Since the ball was released from the pitching machine with angular velocity, a lift force was immediately seen on the ball. The lift force before the first light box affected the vertical position of the ball inside the light box. This also affected the angle of projection. To account for this, first an acceleration due to lift (a_L) was calculated

assuming zero lift was applied to the ball before Light Box A (refer to Table 4.2 for a sample of iterated accelerations). Using the initial calculated value of acceleration (column 3 in Table 4.2), a solver function in Excel was used to iterate by changing values of a_L in column 1 (Table 4.2) until the difference between the accelerations (column 1 less column 3 in Table 4.2) was less than or equal to 1×10^{-6} . Thus a_L was determined and applied over the entire ball path.

Table 4.2- Sample calculations showing iteration process to find a_L .

Acceleration of ball (use this cell to iterate)	Error of acceleration	Acceleration of ball (ft/s ²)
-7.6	-0.56	-7.1
21.4	0.53	20.9
16.6	-0.59	17.2
25.6	-1.69	27.3
22.3	-1.09	23.4
19.6	-2.44	22.1
28.0	-2.00	30.0
5.3	-2.07	7.4
10.5	-2.98	13.5

The average uncertainty in C_L was found to be 0.015.

Section 4.7 – Experimentally determining angular velocity of the ball

A high speed camera was used to record each shot after it exited the three wheeled pitching machine. The camera was placed such that at least seven frames were recorded at the maximum pitch velocity. Black dots were drawn on the surface of the ball to provide high contrast visible to the camera (see Figure 4.27). The video was imported into a computer and horizontal and vertical coordinates of the dots were tracked using *Motion Plus* software. Coordinates were exported from *Motion Plus* and imported into

Excel. The angle of rotation observed on the ball in 7/1000s of a second is minimal.

Hence fitting the coordinates to a periodic curve was not possible. The position of the dots in the first frame were compared to the dots in the last frame such that an angle of rotation could be calculated. The angle was found by removing the translational components of the coordinates by finding the centroid (P_{cx}, P_{cy}) of the black dots in each frame,

$$P_{cx} = \frac{1}{3}(P_{1x} + P_{2x} + P_{3x}) \quad (4.13)$$

$$P_{cy} = \frac{1}{3}(P_{1y} + P_{2y} + P_{3y}) \quad (4.14)$$

Where (P_{1x}, P_{1y}) , (P_{2x}, P_{2y}) , and (P_{3x}, P_{3y}) are the global coordinates of the black dots in each frame. By subtracting the centroid coordinates from the global coordinates, only angular coordinates remained (see Figure 4.28). Using the length from the centroid to the dot, C_1 , and the law of cosines, the angle of rotation, θ , was found as,

$$C_1 = \sqrt{(P_{1x} - P_{cx})^2 + (P_{1y} - P_{cy})^2} \quad (4.15)$$

$$\theta = \arccos\left(\frac{-((P_{1x1i} - P_{1x1f})^2 + (P_{1y1i} - P_{1y1f})^2) + 2(C_1)^2}{2(C_1)^2}\right) \quad (4.16)$$

An angle for each dot on the ball was calculated to find the average angle of rotation. Finally, the angular velocity was found by dividing the average angle of rotation by the total time.

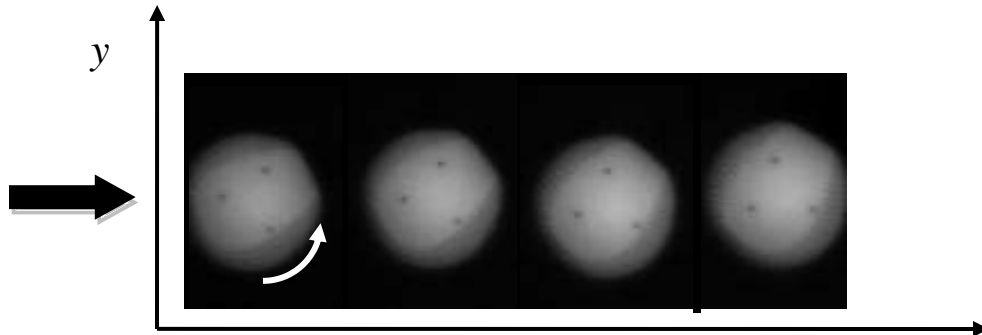


Figure 4.27 - Image progression of a translating and rotating baseball through four frames.

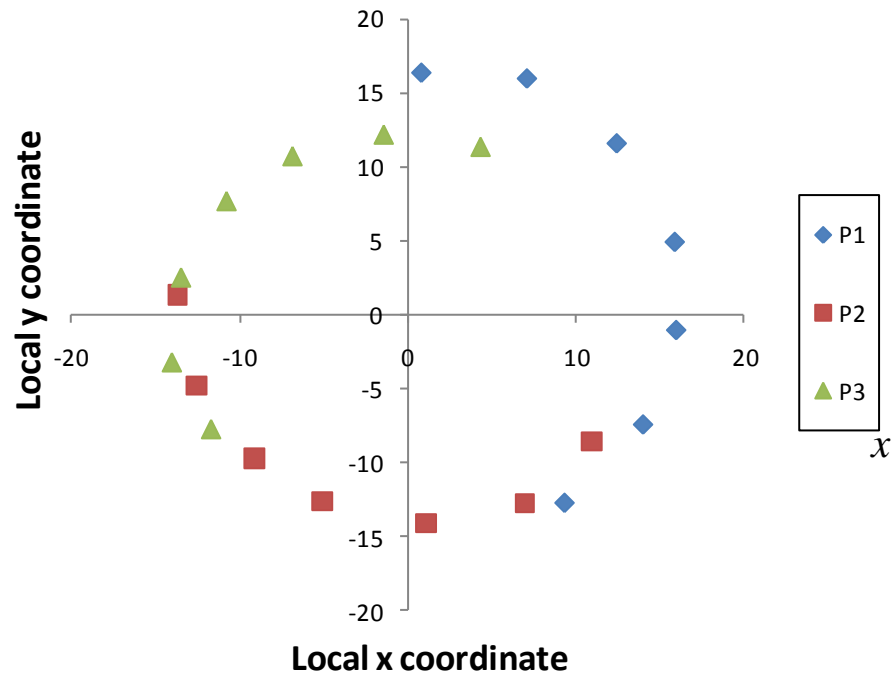


Figure 4.28 - Local coordinates of all three dots on a baseball in flight (pixels).

Section 4.8 – Drag results

4.8.1 Smooth Sphere

Past research has primarily focused on smooth sphere aerodynamics; hence the first data set taken here was of a smooth sphere for comparison. The first sphere was a black acrylic contact juggling ball that had a similar diameter to a baseball, but weighed over nine ounces (see Figure 4.29). Due to its weight this sphere was unable to reach a

high enough Reynolds numbers to enter the drag crisis region. The second smooth sphere, both lighter and greater in diameter, was used for the higher Reynolds region and reached the drag crisis. This was a hollow, soft rubber, smooth stage juggling ball (see Figure 4.30).



Figure 4.29 – Acrylic contact juggling ball.



Figure 4.30 - Rubber smooth stage juggling ball

The C_D curve for the sphere is comprised of both sphere types as shown in Figure 4.31. The onset of the drag crisis is seen just before $Re = 2 \times 10^5$. Achenbach (12) found the onset for the smooth sphere to occur around $Re = 3 \times 10^5$. The reason for the early crisis seen here may be that the hollow juggling ball might have slightly deformed or was not as smooth as Achenbach's. Millikan and Klien's (15) free flight drag crisis onset was also around 3×10^5 .

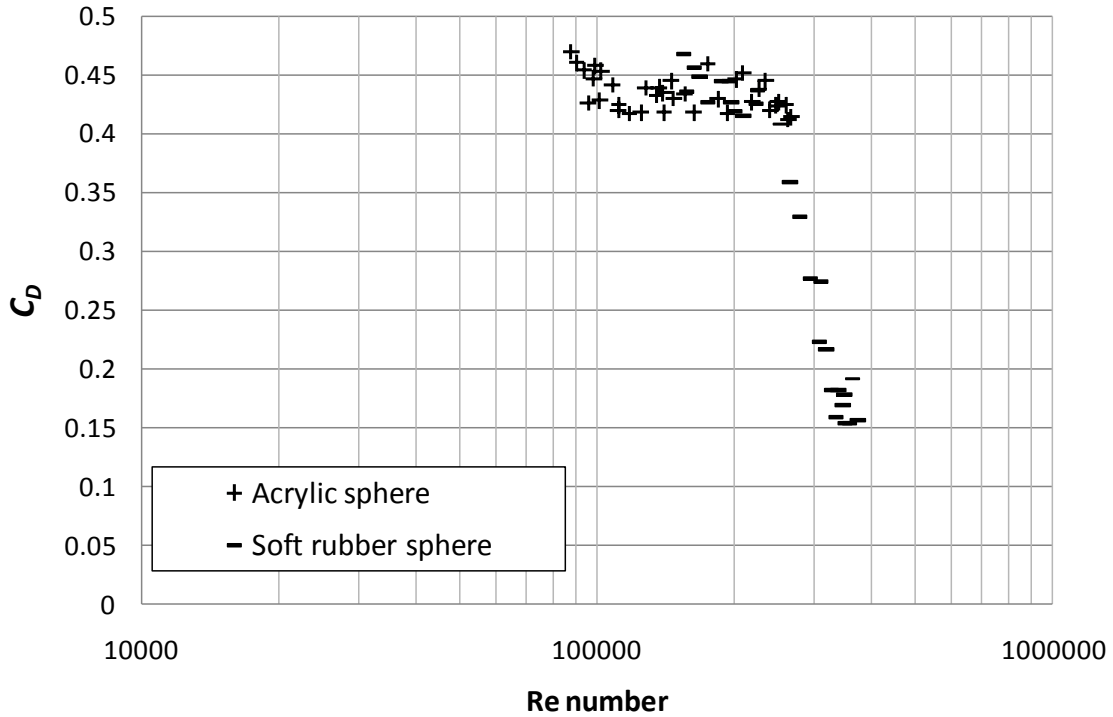


Figure 4.31 - Smooth sphere drag curve with no rotation

4.8.2 NCAA Baseball

The NCAA baseball (see Figure 4.32) was projected in two different orientations with no rotation, as seen in Figure 4.25. Data in the normal orientation showed more scatter than data in the parallel orientation. Even with no rotation, drag was very sensitive to seam orientation (see Figure 4.33). Isolating the parallel orientation, data showed a slight drag crisis region with a minimum C_D as low as 0.3. Data was plotted to show C_D vs pitch velocity (see Figure 4.34). The beginning of the drag crisis appears to be at the start of the data set at 40 mph. The bottom of the crisis is near a pitch velocity of 85 mph, which is easily achieved by baseball pitchers.



Figure 4.32 - NCAA baseball

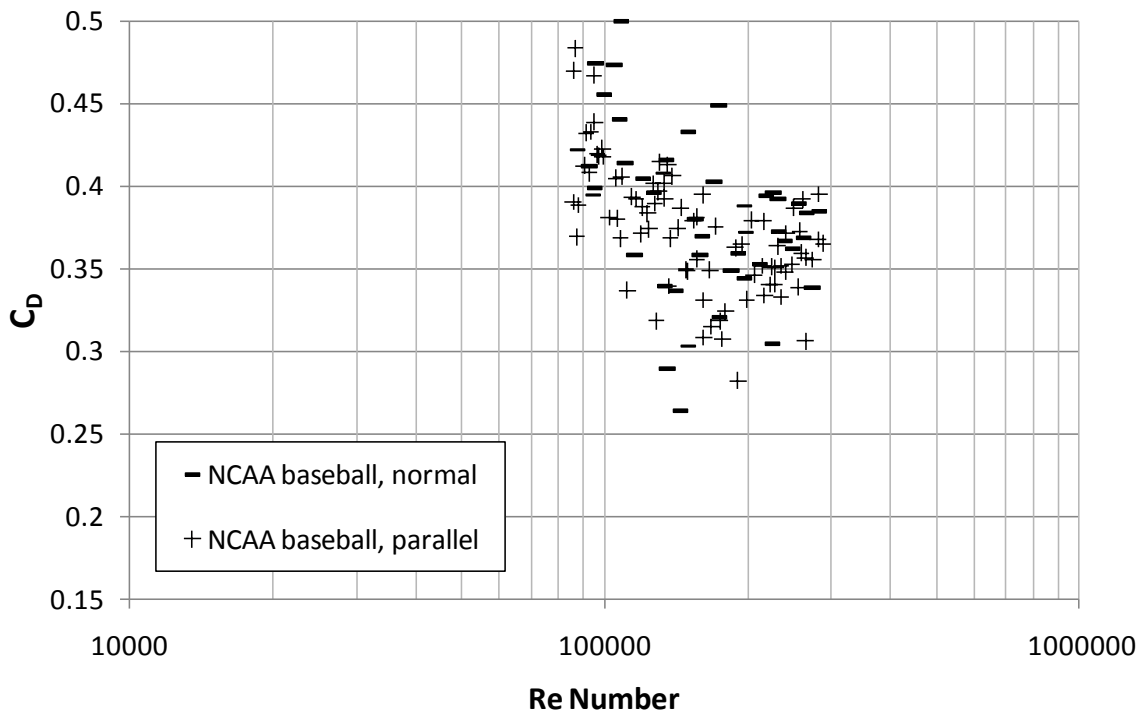


Figure 4.33 - NCAA baseball drag curve normalized with no rotation

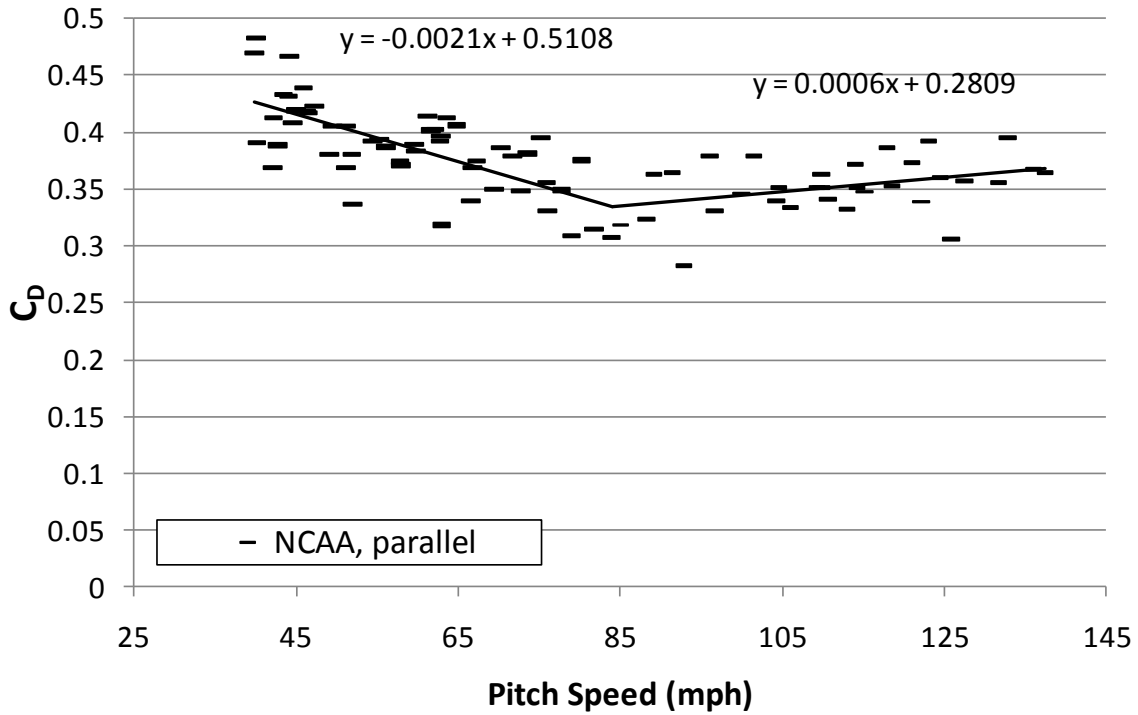


Figure 4.34 - NCAA baseball drag curve with no rotation (vs. pitch speed)

The effect of spin on C_D for a baseball is often ignored and was considered here (see Figure 4.35). The translational velocity for the rotating balls ranged from 60 mph to 99 mph with angular velocities from 22 to 4731 rpm. The NCAA baseball was rotated in two orientations. The normal orientation has four seams traveling through the air flow, while the parallel orientation has two seams traveling through the airflow. The rotational and linear velocities were normalized to a spin factor, S . Rotating spheres observed elsewhere [(17), (22)], show an increase of C_D with spin. Faster spin apparently disturbed the boundary layer, increasing drag. In the case of the NCAA baseball, a drag increase with rotation was observed.

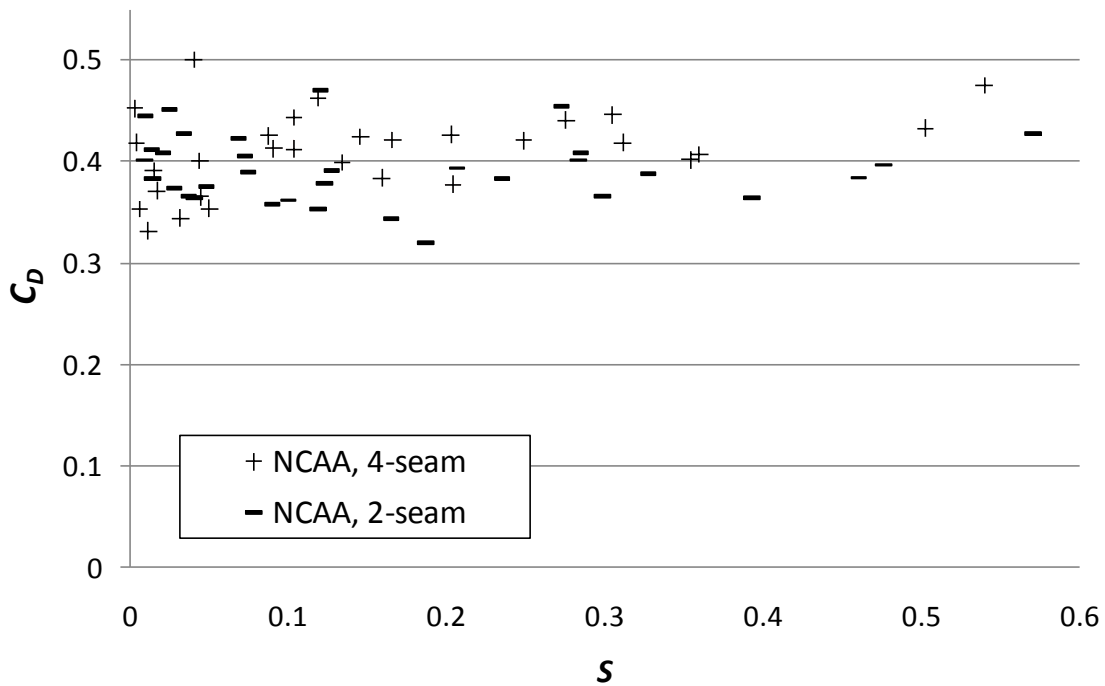


Figure 4.35 - NCAA baseball with rotation normalized to spin factor

The average C_D for a non rotating NCAA baseball in the 60-90 mph range was 0.34 where the rotating baseball was 0.41.

4.8.3 MLB Baseball

The MLB baseball (see Figure 4.36) was projected in the parallel orientation. C_D was observed to be as low as 0.26 (see Figure 4.37). The low stitch height provided a drag curve with little scatter. Resembling more of a smooth sphere than the NCAA ball, the MLB ball revealed a more pronounced drag crisis.

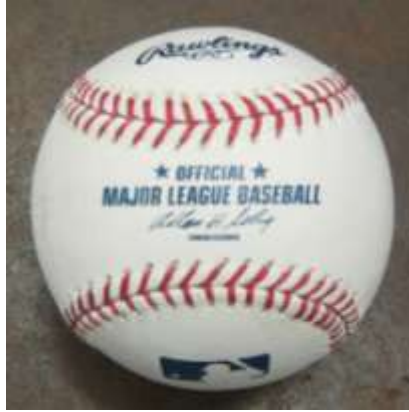


Figure 4.36 - MLB baseball

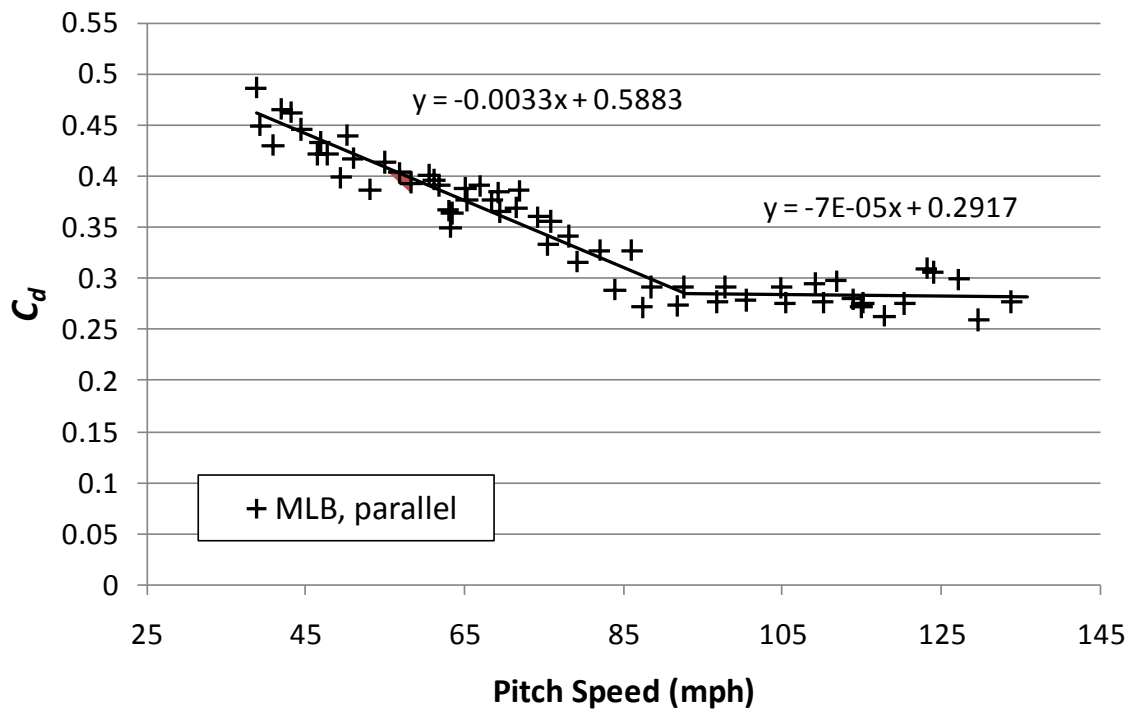


Figure 4.37 - Drag curve for MLB baseball

Rotation was applied to the MLB ball and drag measurements were taken.

Similar to the NCAA baseball, the C_D increased as S increased, but at a greater rate.

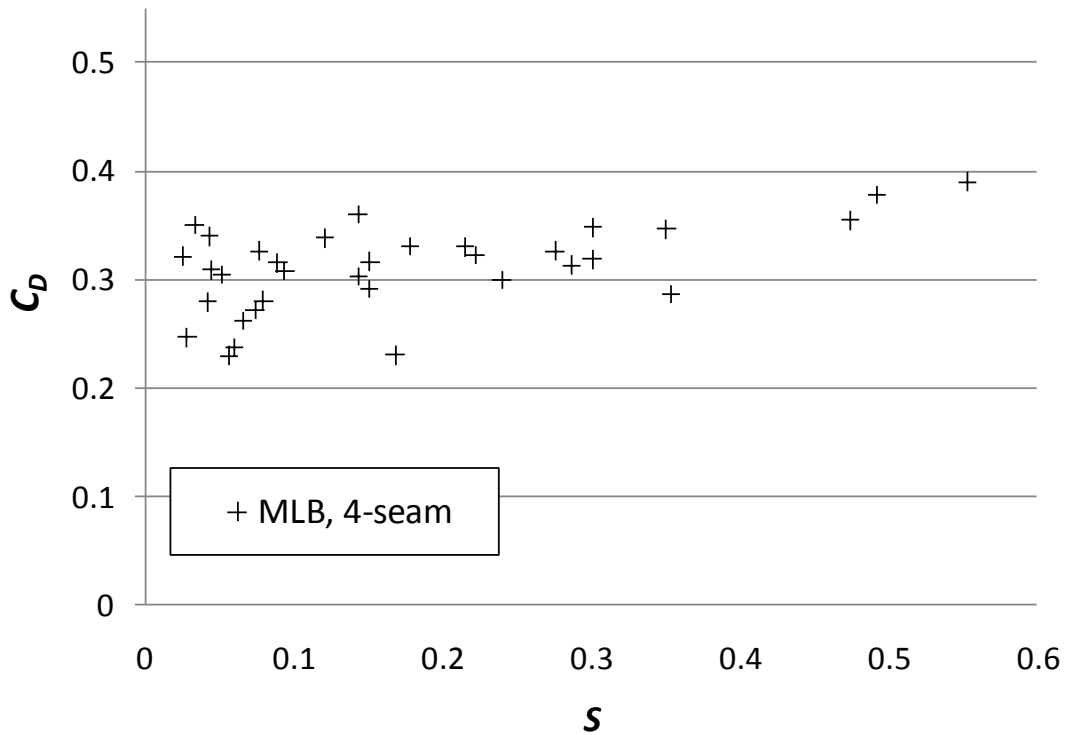


Figure 4.38 - MLB baseball drag curve with rotation.

4.8.4 Softball

The 12 inch circumference and the 11 inch circumference softballs (see Figure 4.39) were analyzed in the parallel orientation. The 11 inch has a stitch height three times greater than the 12 inch ball. Both were tested to see how various stitch heights changed the drag curve (see Figure 4.40 and Figure 4.41). The 12 inch ball experienced less overall drag and appeared to be entering a small drag crisis which began at the lowest velocity tested. The lowest drag coefficient was around 0.25. The 11 inch softball also appeared to be in a drag crisis at 40 mph. Therefore it is unclear when the crisis began for the softball. Drag was higher for the 11 inch ball and had a drag crisis smaller in magnitude of a drag crisis compared to the 12 inch ball. The minimum drag for the 12

inch softball was 0.27 achieved around 80 mph. Women's fast pitch speeds range from 60-70mph (33). Pitch velocities in men's fast pitch may achieve 80 mph.

Rotation of softballs was not considered because they would not fit in the pitching machine.



a)

b)

Figure 4.39 - a) 11 inch circumference softball with raised stitches; b) 12 inch softball

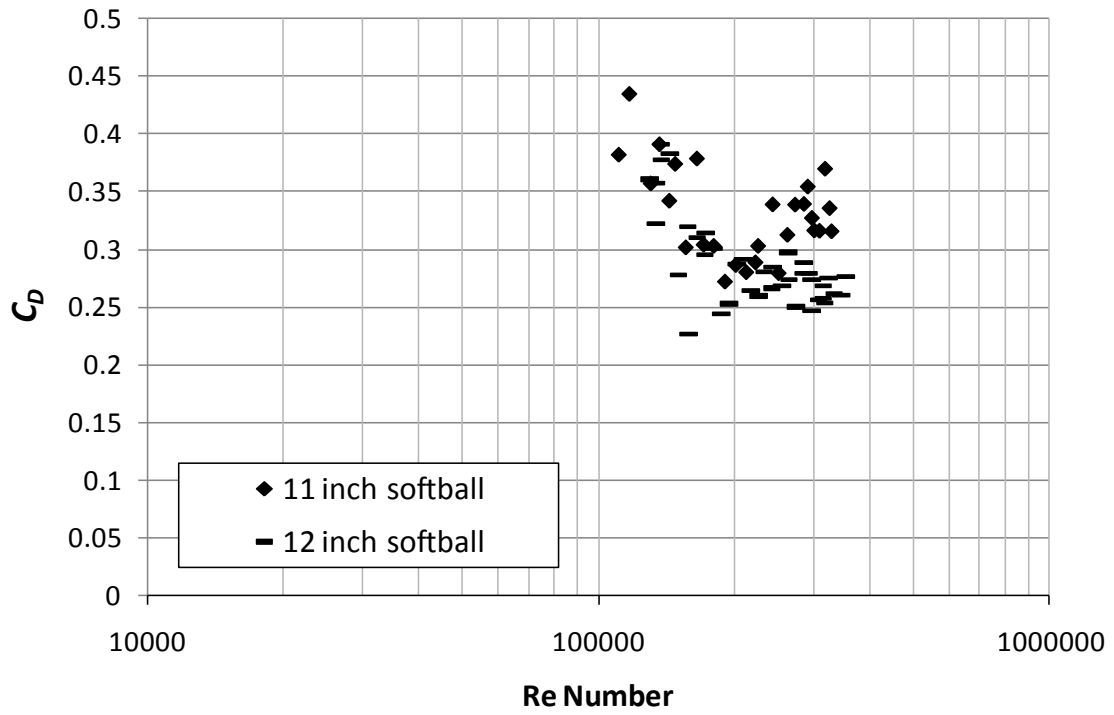


Figure 4.40 - Softball drag curve normalized

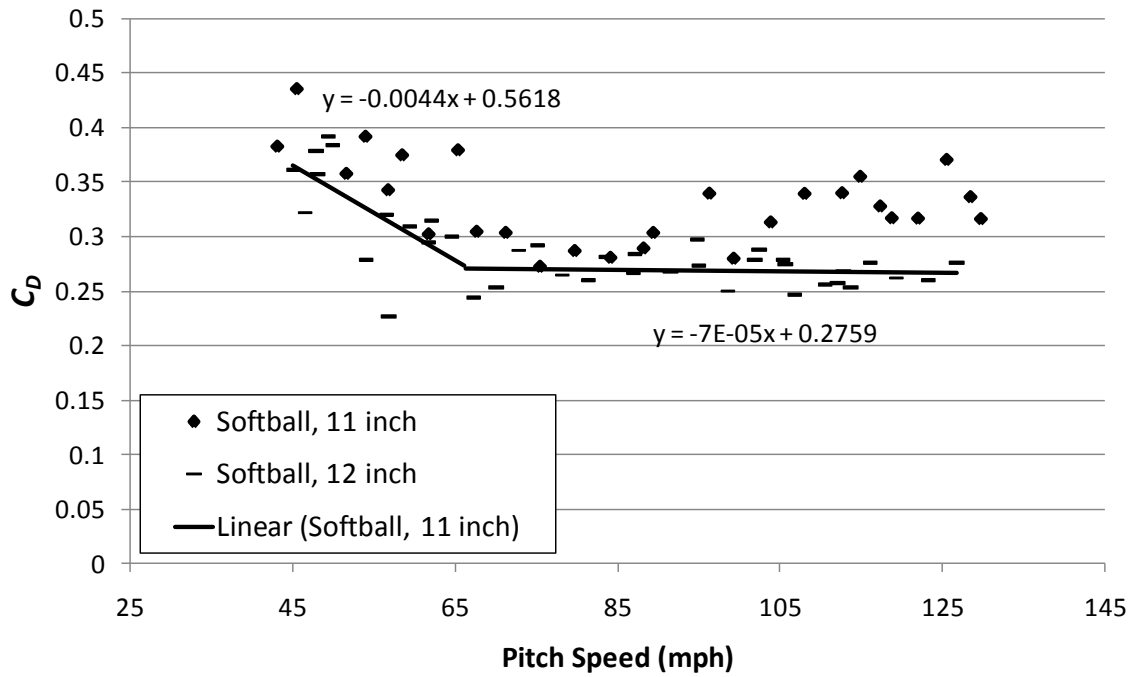


Figure 4.41 - Softball drag curve.

4.8.5 Cricket ball

The cricket ball (see Figure 4.42) was analyzed in both parallel and normal orientations to study how the seam placement would affect drag. As seen with the two orientations of the NCAA baseball, the seam placement affects drag (see Figure 4.43). Unlike the NCAA baseball, the normal orientation does not show scattered data. A drag crisis is not apparent for the normal orientation either. The parallel orientation does show a small crisis with the minimum drag around 0.26. Having the seam in the normal orientation increased drag.



Figure 4.42 - Cricket ball

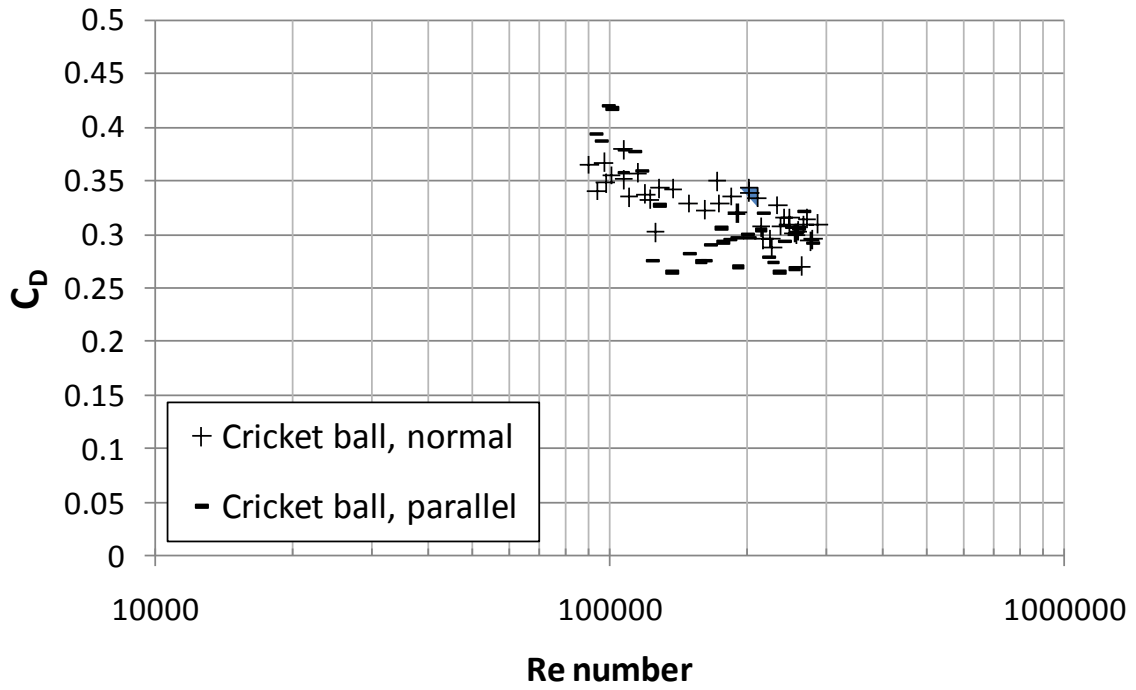


Figure 4.43 - Cricket ball drag curve normalized

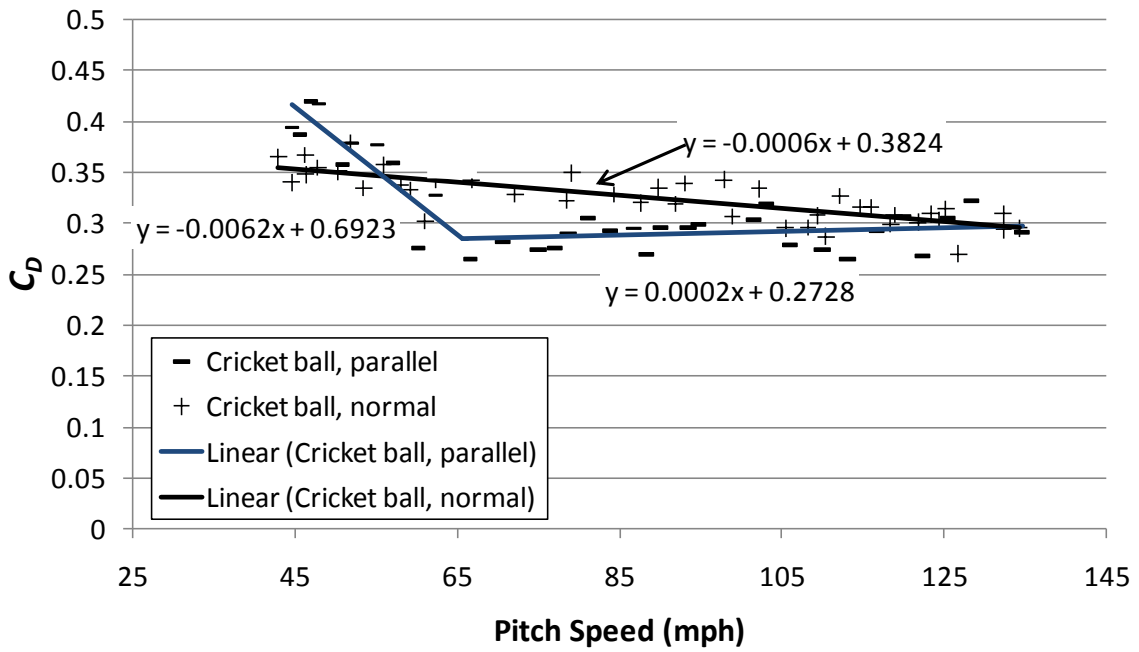


Figure 4.44 - Cricket ball drag curve

4.8.6 Dimpled pitching machine ball

The dimpled pitching machine ball (see Figure 4.45) was analyzed both with and without rotation. The data for the ball showed little scatter compared to the NCAA baseballs (see Figure 4.46). Due to constraints of the test apparatus the velocity of the dimpled ball could not be slowed down enough to see the beginning of the drag crisis. Compared to other dimpled spheres, such as the golf ball the onset should be around Reynolds 70,000. The dimples appear to induce the drag crisis at a lower Reynolds number and create a more uniform separation on the ball.

Rotation increased drag as well. Compared to both types of baseballs, the dimpled ball saw the greatest drag rate increase as spin factor increased (see Figure 4.47).



Figure 4.45- Dimpled pitching machine ball

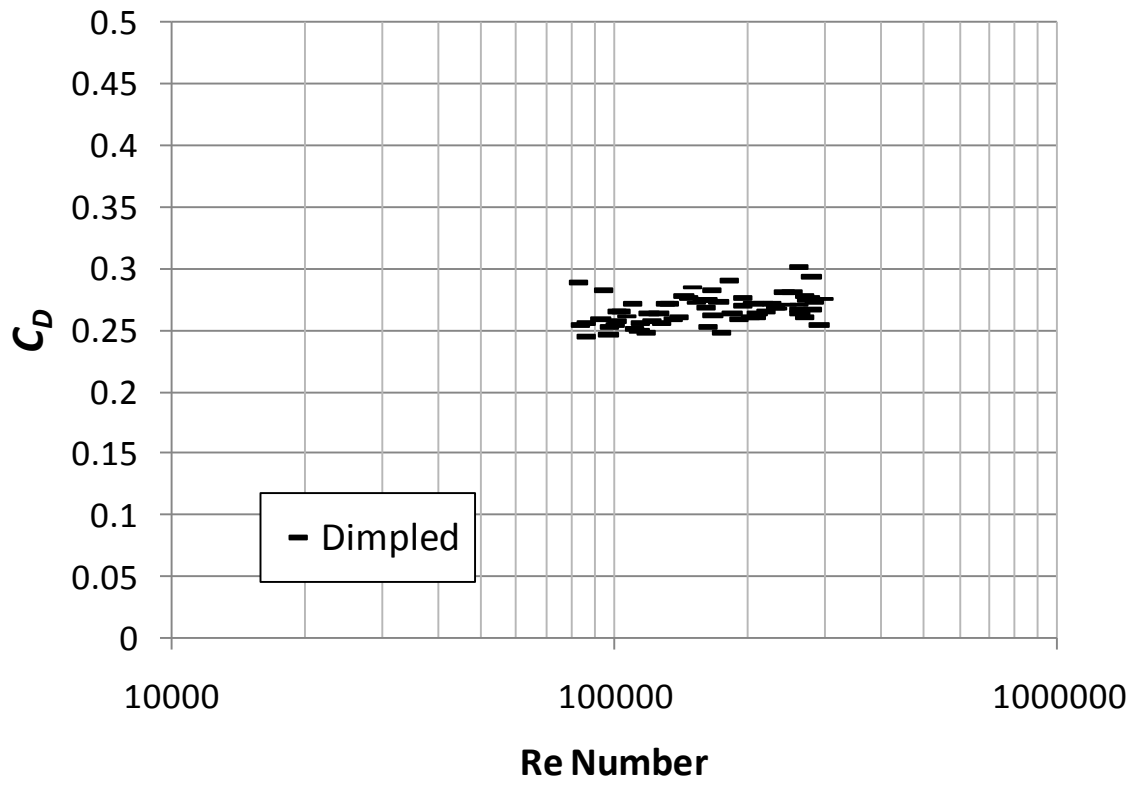


Figure 4.46 - Drag curve for dimpled pitching machine ball.

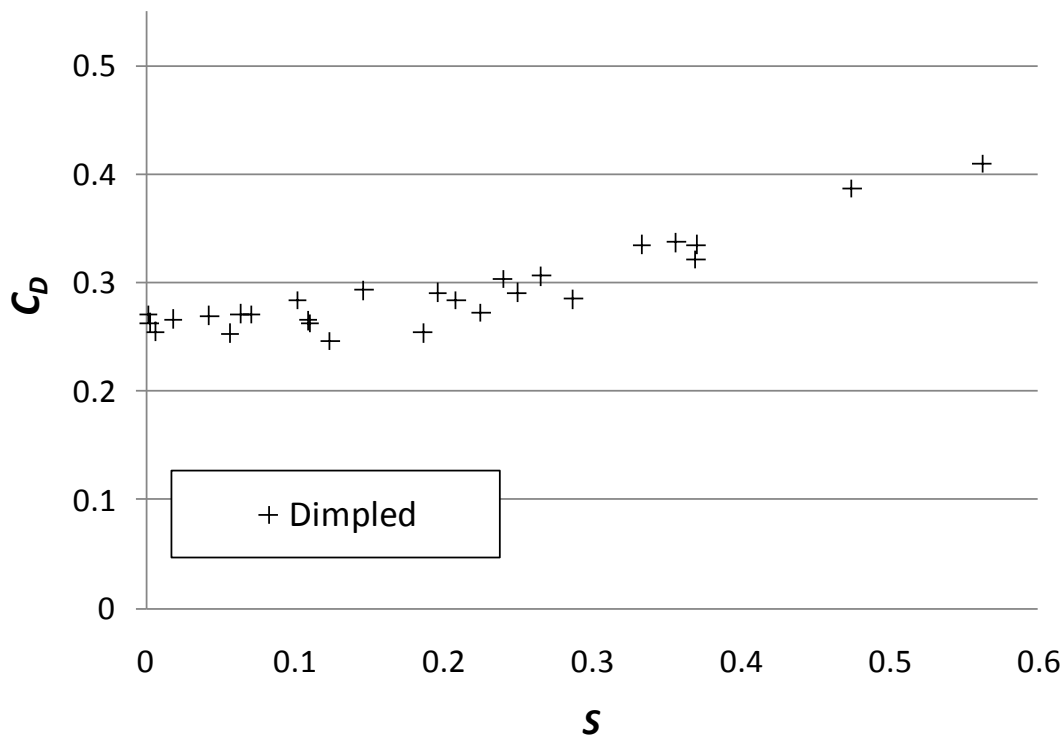
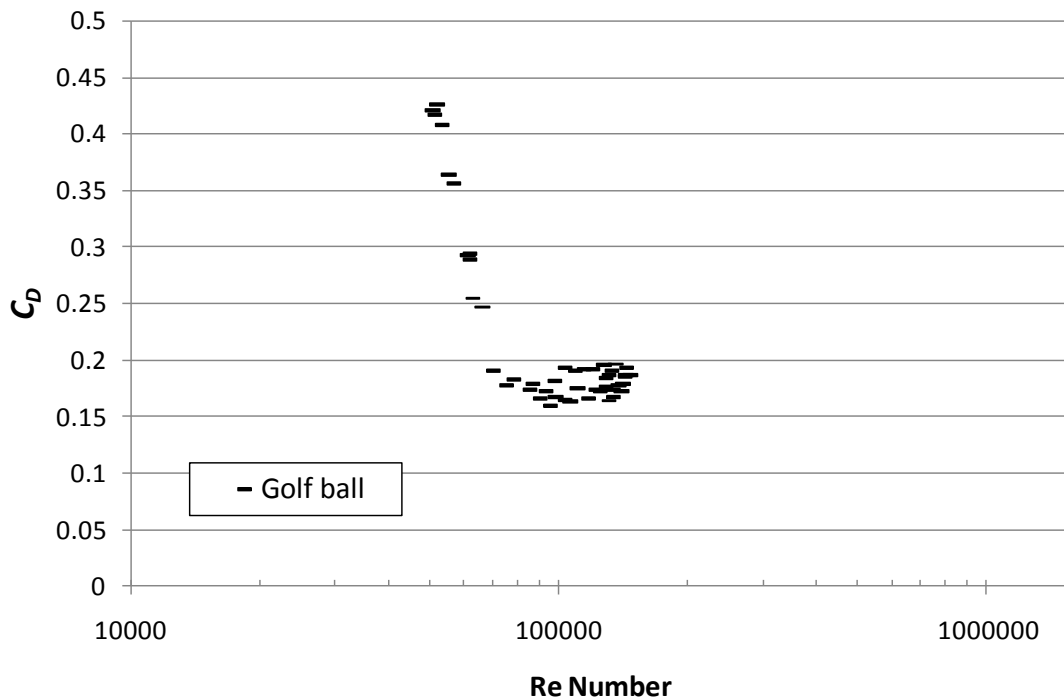


Figure 4.47 - Dimpled pitching machine ball drag curve with rotation

4.8.7 Golf ball

The golf ball was analyzed with no spin. Of all sports balls the golf ball produced the most severe drag crisis. The golf ball had dimples similar to the pitching machine ball, but dimples touched instead of being spaced far apart. Unlike the dimpled pitching machine ball, the golf ball had a smooth glossy finish aiding in a lower drag. The drag crisis onset is far lower than any other sports ball occurring at Reynolds number 70,000. The minimum drag observed was 0.17. Bearman and Harvey (17) found their minimum drag on dimpled balls to be 0.23, which is closer to the dimpled pitching machine ball. This is expected since the golf ball has been continually optimized to have less drag.



4.8.8 Drag results summary

The drag coefficient for all balls without rotation is shown in Figure 4.48. As expected, the dimpled surface of the golf ball and pitching machine ball caused the drag crisis to occur at a lower Reynolds number than the smooth sphere. The optimized dimple pattern of the golf ball appears to help maintain the relatively large magnitude of its drag crisis. While the NCAA baseball, MLB baseball, 12 inch softball, and cricket balls show C_D decreasing with increasing speed, the magnitude of their “drag crisis” was significantly smaller than the smooth sphere and golf ball. Balls with taller stitches, such as the 11 inch softball and NCAA ball, show less evidence of a crisis.

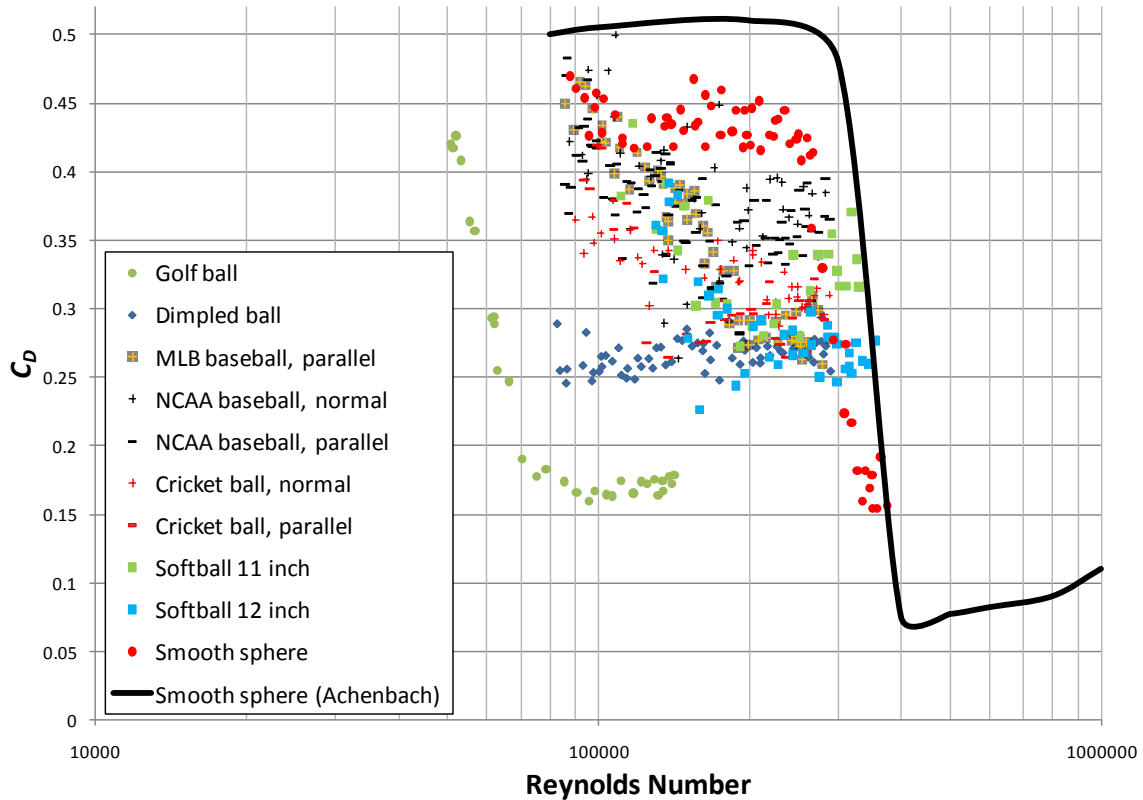


Figure 4.48 - Drag curve for all balls tested

Scatter in drag was larger for the NCAA baseball and softball than the other ball types or orientations. The arrangement of the stitches on the baseballs, softballs, and cricket balls likely play a role in their respective drag crisis. The stitches on a baseball trip the boundary layer earlier than a smooth sphere inducing turbulence and moving the flow separation point to the backside of the ball. Since the stitches are raised and rough, the magnitude of the drag crisis is muted. Variation in the orientation of stitched balls will also contribute to variation in drag as seen in Figure 4.32.

The drag crisis of the 11 inch softball was comparable to the NCAA baseball (see Figure 4.49), which have relative seam height to diameter of 0.019 and 0.014 respectively. The crisis of the 12 inch softball was comparable to the MLB baseball (see Figure 4.50), which had relative seam height to diameter of 0.0047 and 0.0042.

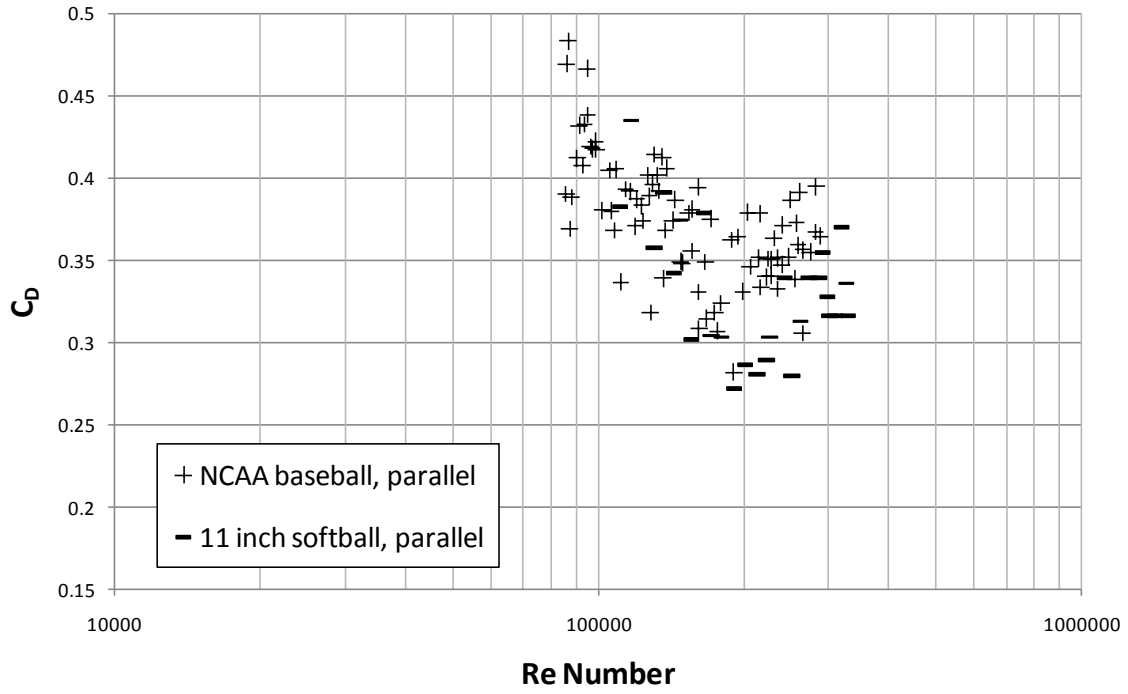


Figure 4.49 - Comparison of balls with similar seam height to diameter ratio (raised seam).

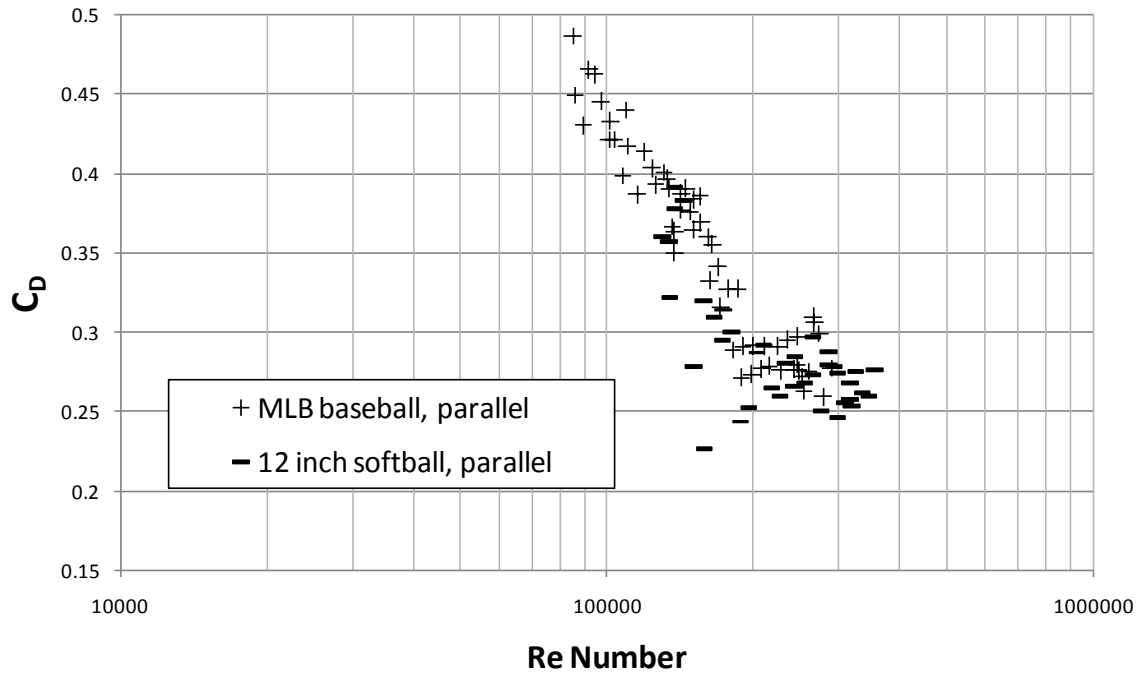


Figure 4.50 - Comparison of balls with similar seam height to diameter ratio (flat seam).

Comparing all balls that were spun, the dimpled sphere had the greatest increase in drag as spin factor increased (see Figure 4.51). The roughest ball showed the least drag increase with spin factor increase. Scatter in drag data was observed for low S values. In this region the angular velocity was low and translational velocity varied from 60 to 99 mph, which is when the baseball is going through its drag crisis. Hence a wide range of C_D was found at low values of S .

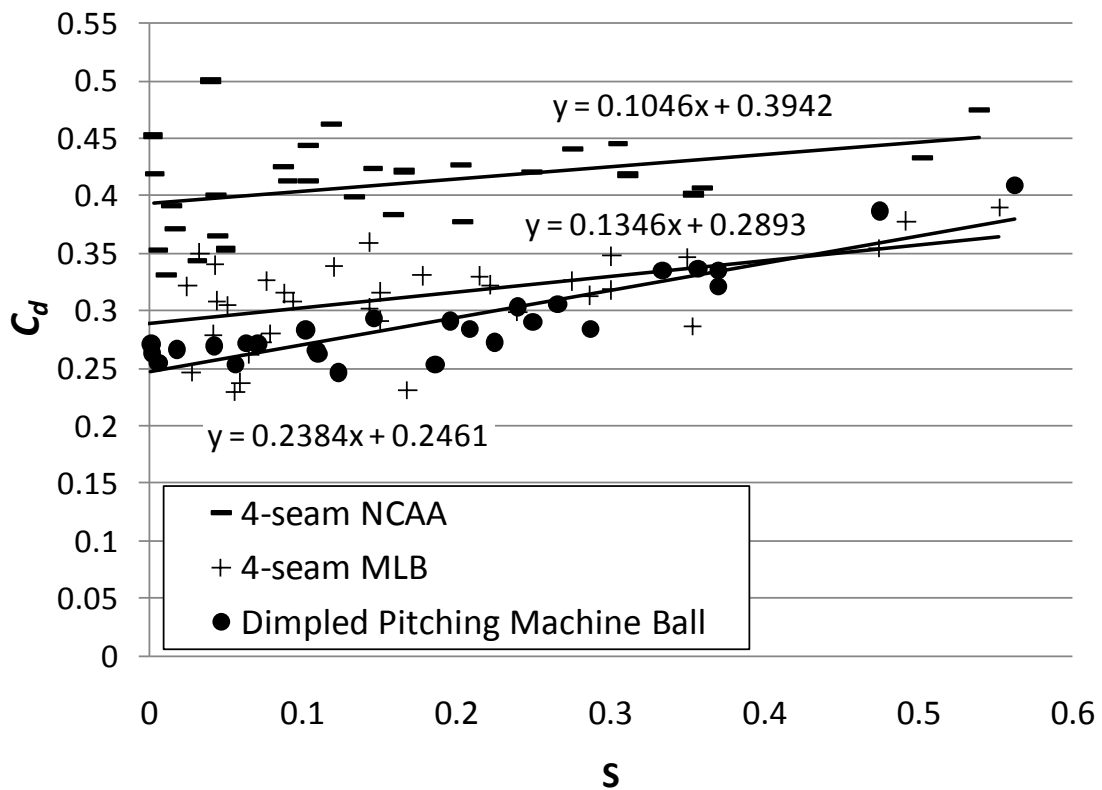
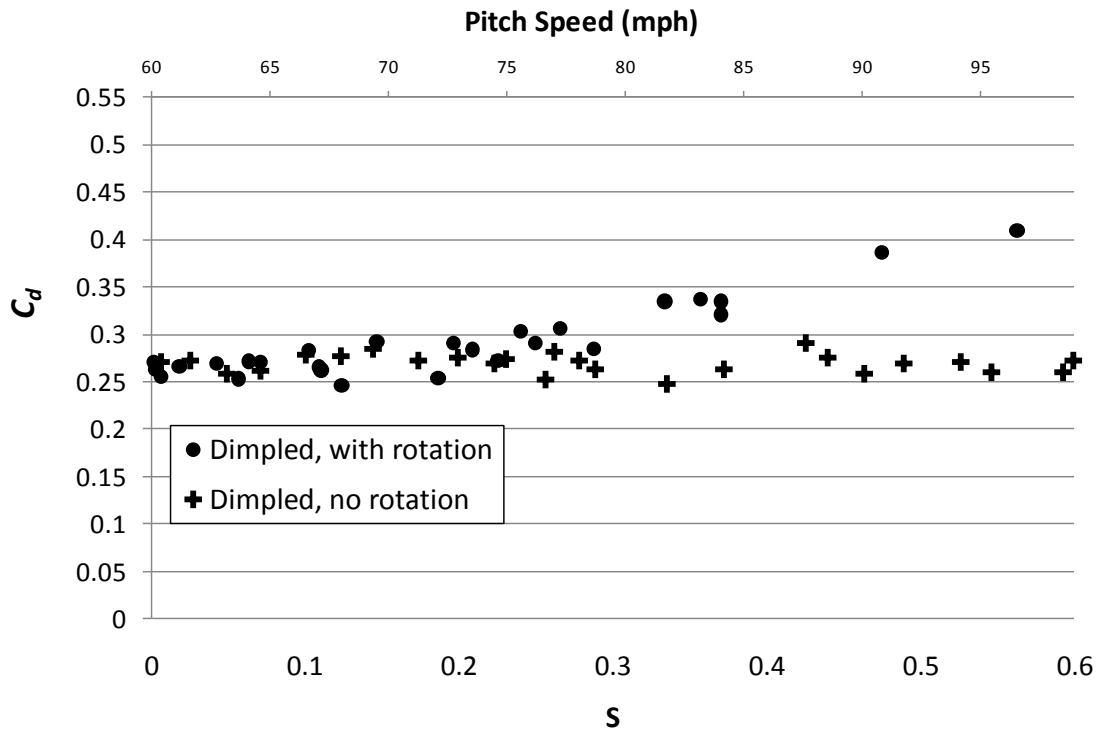


Figure 4.51 - Drag curve for rotating balls.



4.52 - Drag curve for a dimpled sphere with and without rotation.

Section 4.9 – Lift results

4.9.1 NCAA Baseball

Lift force was measured on the NCAA baseball in the normal and parallel orientations. The average C_L for the two different orientations of the NCAA baseball showed little difference (see Figure 4.53). However the data was scattered more in the normal orientation revealing sensitivity which may have been caused by the stitch pattern. At low rotational speed, when the ball rotates less than a quarter turn between the light boxes, the stitch pattern on the baseball affected separation on the ball. As seen previously, separation on the ball will behave differently depending on whether the stitches pass through the critical separation region on the ball. For example, if a ball was given backspin in the normal orientation and the stitches began on the stagnation point of

the ball, during a quarter turn the top stitch would move to the backside of the ball and the bottom stitch would move to the front of the ball. The stitch on the top no longer induces turbulence moving the separation to the backside of the ball and separation will occur at 80 degrees. The bottom stitch does induce turbulence and separation will occur at 120 degrees. Thus, the ball would have a force exerted downward instead of upward. This is similar to the concept of the reverse Magnus effect. Though results do not show a reverse in force, it does show a reduction in force. Since force was measured on the ball over a 16 foot flight distance, certain orientations along its flight could have produced a reverse Magnus effect.

Looking back at Watts and Sawyer, if a ball rotates less than 90 degrees, then the sum of lateral forces will be imbalanced. Therefore, depending on the stitch orientation at the beginning of the ball's path, the sum of lift force could have been positive or negative by the time it passed through both light gates.

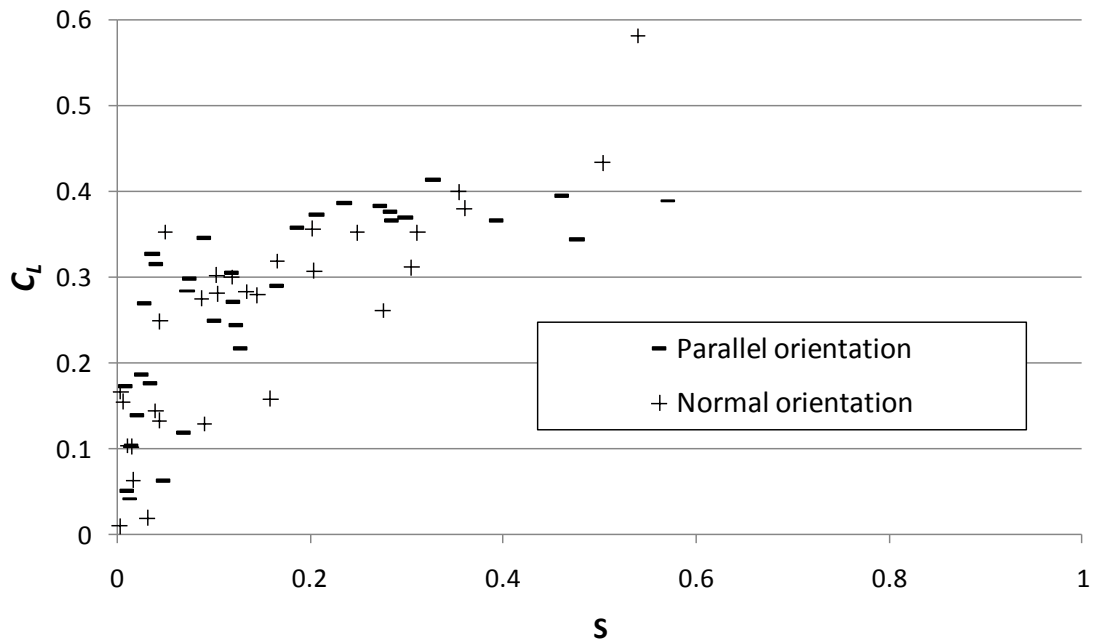


Figure 4.53 - Lift curve for NCAA in 2 seam and 4 seam orientations.

4.9.2 MLB Baseball

Data from the NCAA ball revealed little change in magnitude of lift between the two orientations, therefore only one orientation (parallel) of the MLB was tested. The MLB ball had less scatter and less lift than the NCAA ball (see Figure 4.54). This is due to the stitch height being flatter than the NCAA baseball.

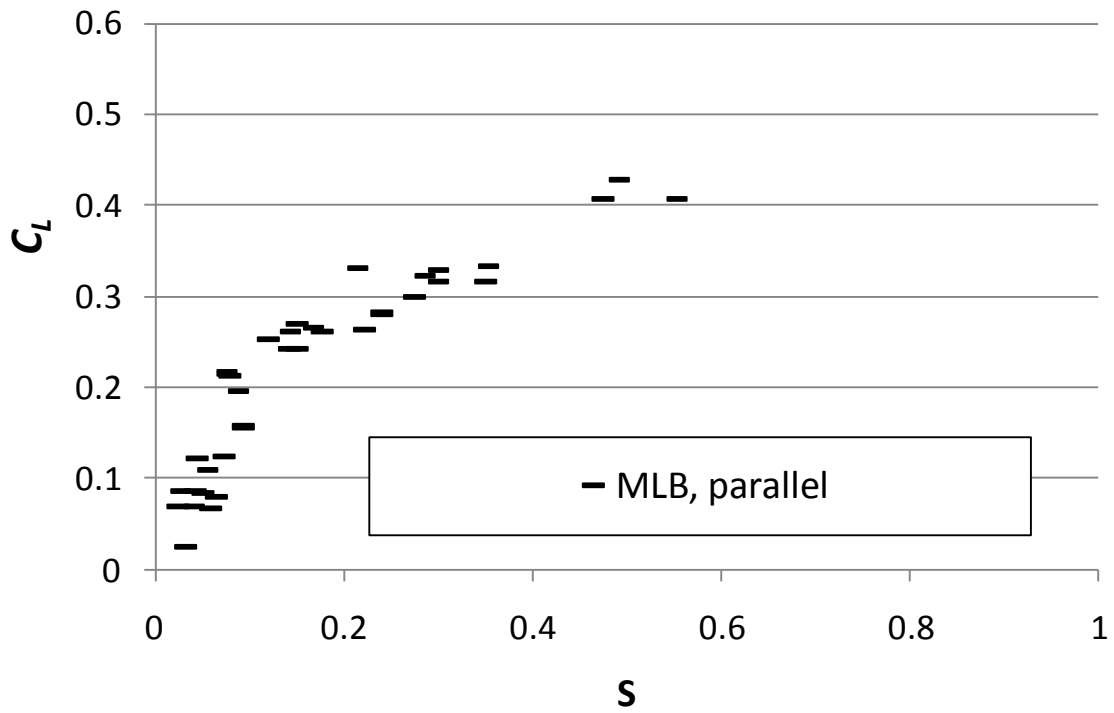


Figure 4.54 - Lift curve for MLB baseballs.

4.9.3 Dimpled pitching machine ball

The dimpled pitching machine ball was tested and a lift curve was obtained (see Figure 4.55). Results were similar to that of the MLB baseball. Variation in the data was minimal.

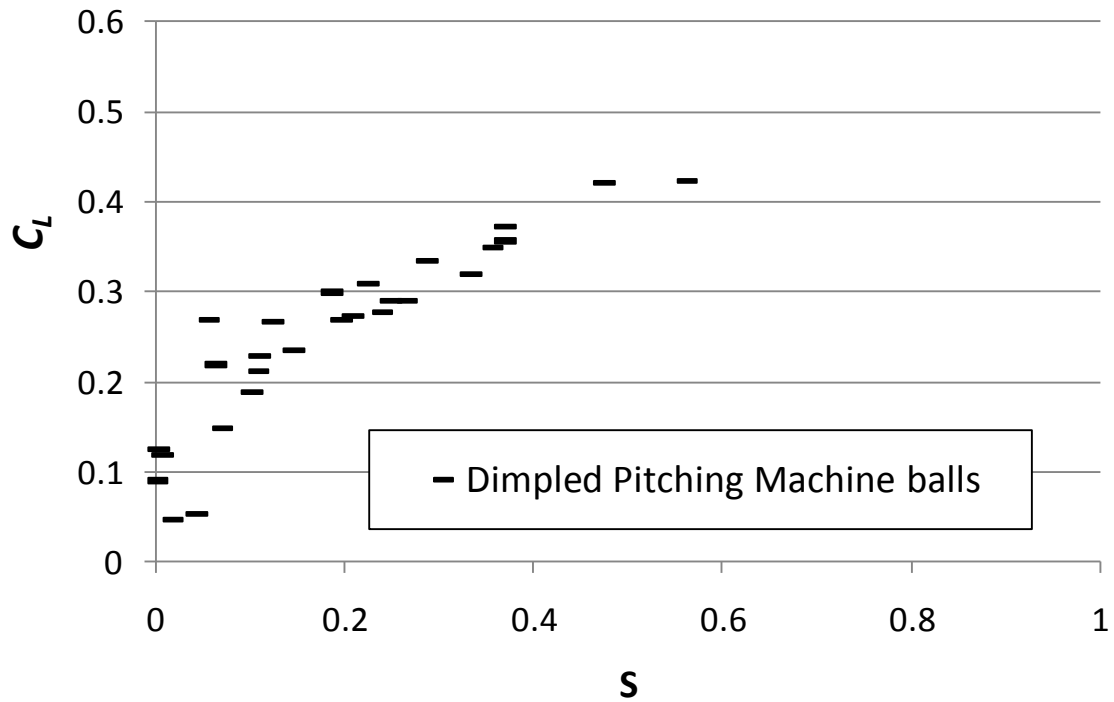


Figure 4.55 – Lift curve for dimpled pitching machine ball

4.9.4 Lift results discussion

Lift for three types of sports balls showed similar trends. The C_L for the NCAA baseball was 15%-25% higher at any given S value than both the MLB baseball and dimpled ball. The NCAA stitches are higher than the MLB ball which infers that balls with larger surface protrusions and surface roughness will have greater drag as well as lift.

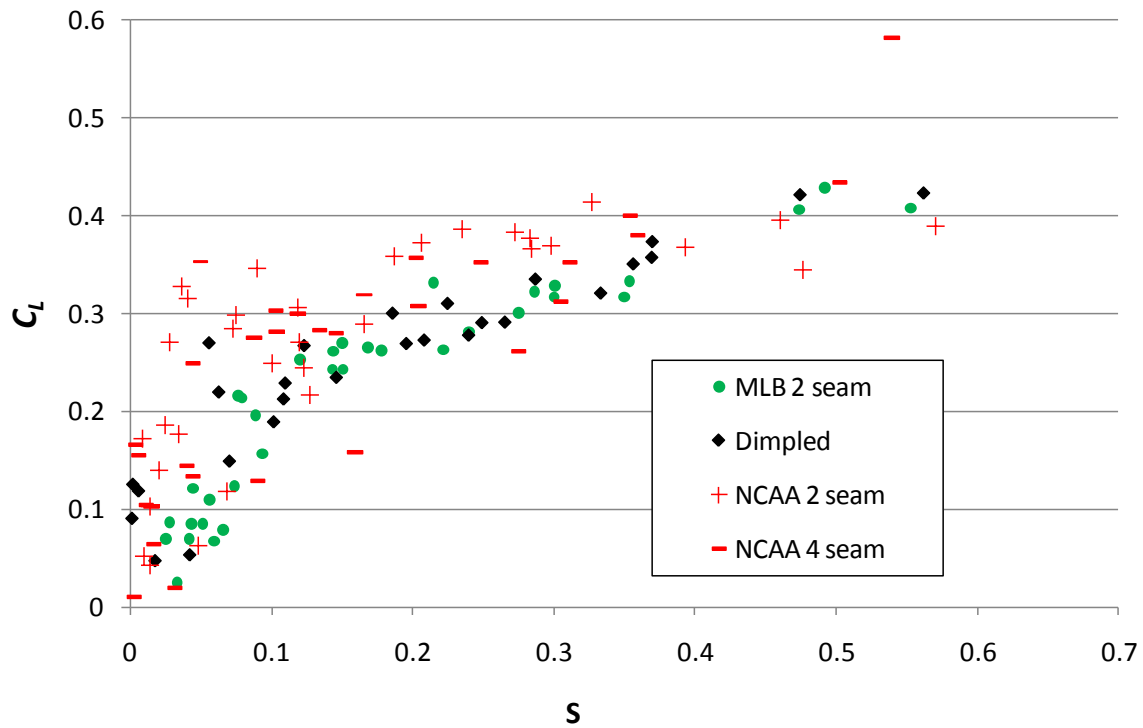


Figure 4.56 - Lift curves for all balls tested.

All the lift results are presented in Figure 4.56, which suggest a bilinear response. This is similar to a 2-D cylinder, but of less magnitude (4). The first range is from spin factor $0.0 < S < 0.15$ where the slope of the C_L is nearly twice that of the slope from $S > 0.15$. Other in flight lift research also revealed a similar trend. A parameterization from Sawicki and Hubbard (24) was plotted (see Figure 4.57) which is a bilinear best fit line consisting of Watts and Ferrer (18), Alaways and Hubbard (20), and unpublished work of Sikorsky and Lightfoot. Also plotted was Nathan's (23) and Jinji's (25) free flight lift data.

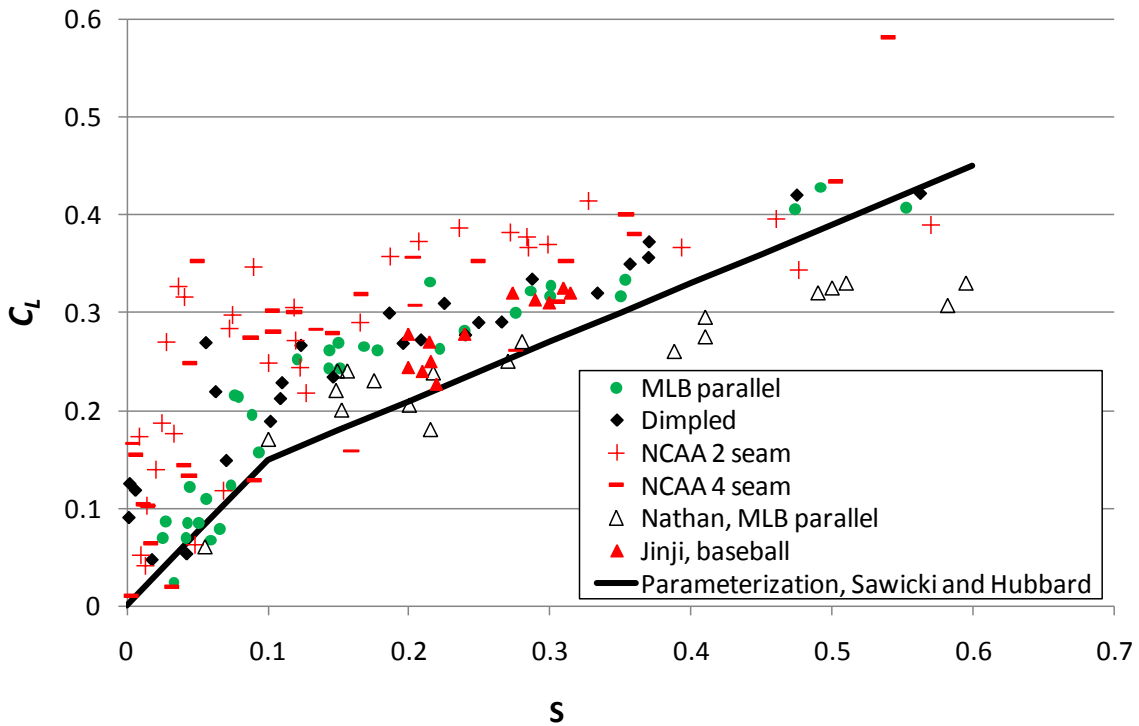


Figure 4.57 - Lift curves plotted against other experiments and research. Open triangles are from (21), closed triangles are from (23), and the solid line is the parameterization from (22).

Nathan and the present MLB data appear to be similar up to $S=0.2$. Then Nathan's data is lower in magnitude. Jinji's data agrees for higher values of S , though his data range is small and only goes from $0.2 < S < 0.32$. The MLB and dimpled data follows the same slope of the parameterization, but appears to be of higher magnitude. This could be due to experimental error.

4.9.5 Experimental Summary

Sports ball aerodynamic properties were measured in situ. Results show a pronounced drag crisis for a smoother sphere, dimpled golf ball, MLB Baseball and 12 inch circumference softball. A small drag crisis was observed for the NCAA baseball,

cricket ball, and 11 inch circumference softball. Orientation and height of stitches affected the magnitude of the drag crisis and the Reynolds number at which the crisis began. Rotation of the ball also increased drag and reduced the chance to have a drag crisis.

Lift was observed similar to that of previous experiments. The same bilinear trends were observed, but magnitudes were 50%-80% greater here. Lift was observed to be higher for balls with larger stitches, or greater surface roughness.

The results from lift and drag curves were applied to various batted baseballs and softballs to predict ball trajectories. Figure 4.58 and Figure 4.59 show optimized trajectories for two scenarios, A and B, comparing three types of balls. Trajectories were calculated by finding the instantaneous velocity, horizontal position, x , and vertical position, y , of the ball using Equations 4.4, 4.5, and 4.6.

All balls in scenario A were given the same batted ball speed (BBS) of 100 mph and initial angular velocity of 1200 rpm. Softball bats are certified for an average player to not exceed a 98 mph BBS (34) and the average college baseball player is said to achieve a BBS around 100 mph (35). The MLB ball traveled the farthest at a distance over 400 feet. The 12 inch softball was next and the NCAA ball traveled the shortest distance. The balls in scenario B were given a 120 mph BBS and a 400 rpm. This resembled a much faster hit with less lift. The MLB ball traveled the farthest, but the 12 inch softball traveled the shortest distance.

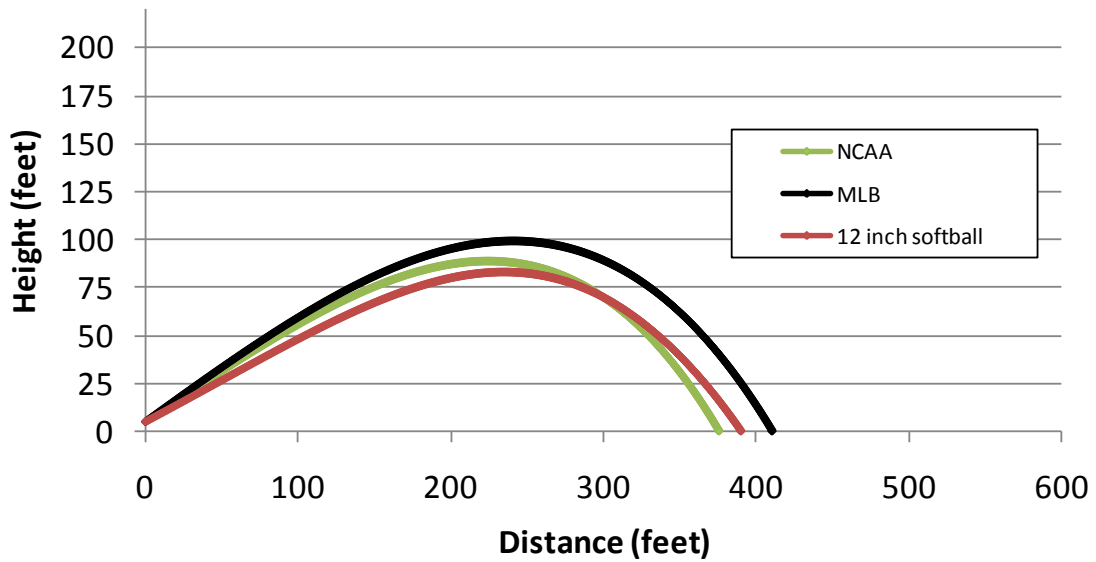


Figure 4.58 – Scenario A: optimized trajectory for an MLB, NCAA, and 12 inch softball at 1200 rpm, 100 mph BBS.

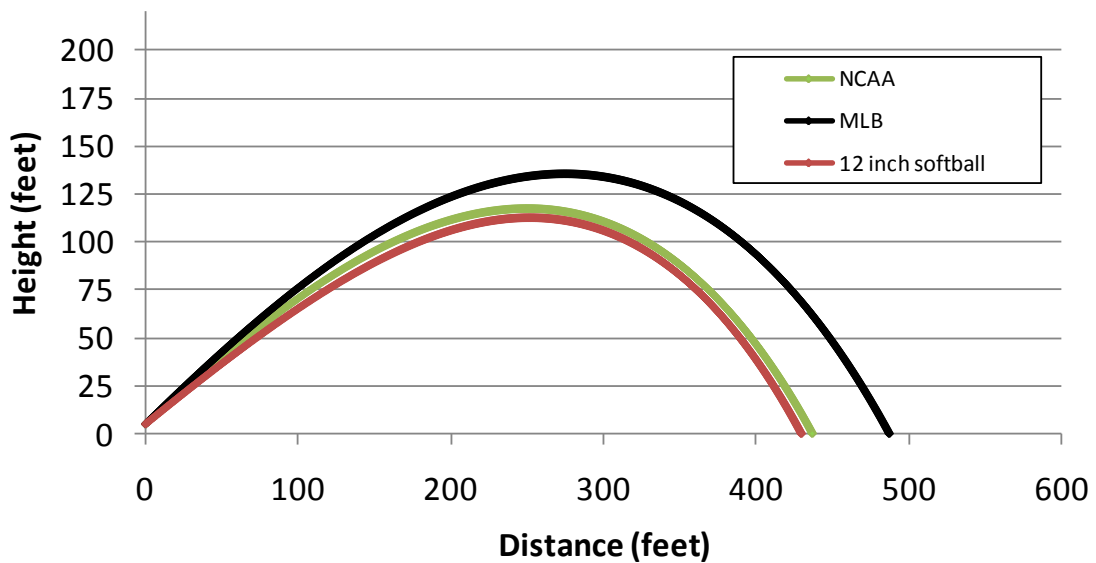


Figure 4.59 - Optimized trajectory for an MLB, NCAA, and 12 inch softball at 400 rpm, 120 mph BBS.

The results from lift and drag curves were applied to various pitched baseballs and softballs to predict lateral ball deflections of a curveball. Figure 4.60 and Figure 4.61 show an overhead view of pitch trajectories for two scenarios. Both scenarios assume the axis of rotation is parallel with gravity. Scenario A shows how a pitched ball will deflect if the pitcher did not angle his or her arm at the release. Scenario B shows how a pitched

trajectory will bend if the pitcher tries to get the ball to cross over home plate. Scenario A was initialized with a 100 mph pitch speed and 500 rpm of spin. The pitches showed a total deflection of 17.9 inches for the softball, and 9.6 inches for the MLB ball. Scenario B was initialized with an 80 mph pitch speed and 1000 rpm of spin. It showed a bend deflection of 6.2 inches for the MLB ball and 9.9 inches for the softball. Scenario B and shows a deflection of 6.2 inches for the MLB and 9.9 inches for the softball.

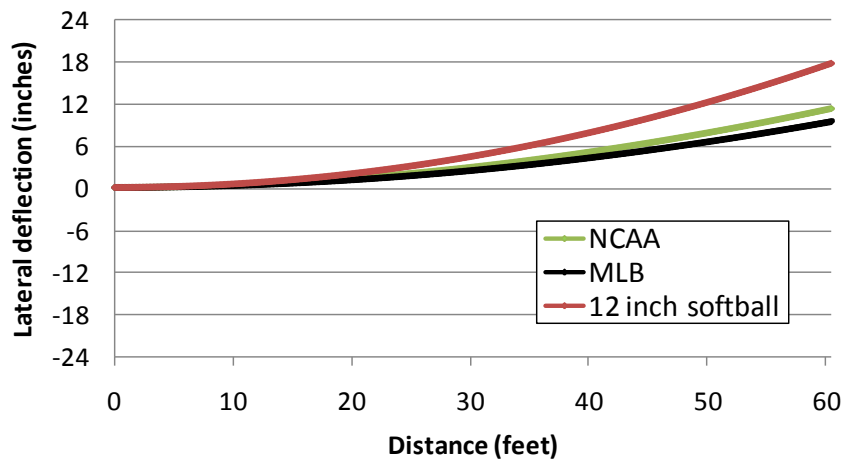


Figure 4.60 – Scenario A: Lateral ball deflections. Pitch speed was 100 mph. Angular velocity was 500 rpm. Release angle was 0 degrees.

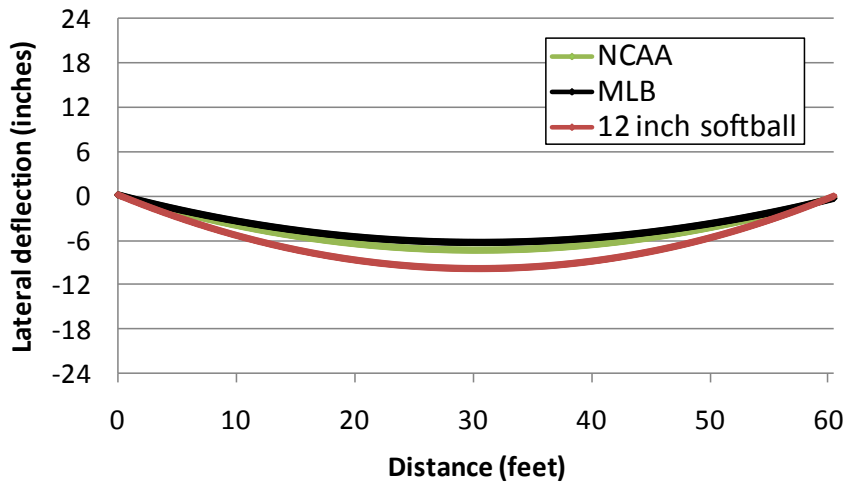


Figure 4.61 – Scenario B: Lateral pitched ball deflections. Pitch speed was 80 mph. Angular velocity was 500 rpm. Release angle was optimized such that each ball would cross home plate.

Chapter V – Summary

Section 5.1 – Summary

The research presented here explored the aerodynamic properties of sports balls in situ. A numerical model was attempted and showed little accuracy. Experimental results were successful for various sports balls including baseballs, softballs, cricket balls, and golf balls.

A large portion of the research was dependent on light gate accuracy. The light gates used here went through rigorous calibration and accuracy tests. After reviewing the calibration data, light gate speed error increased 190% going from the 16.5 inch spacing down to 8.25 inch spacing. At the 16.5 inch spacing, speed measurements from the light gates could be considered accurate to 0.1 mph with a precision error of 0.06 mph.

A numerical model of a smooth sphere and stitched NCAA baseball was modeled in Fluent. The geometry of the baseball was formed in SolidWorks and the smooth sphere in Gambit. Both were meshed using Gambit. Meshed geometry was imported into Fluent where a Realizable $k - \epsilon$ model was used to obtain lift and drag forces. The model was determined unsuccessful as solutions were inconsistent when flow velocities were changed.

Aerodynamic properties were measured on balls in flight under a laboratory setting. Unlike many experiments in the past, the balls were projected through static air instead of forcing air around them such as in a wind tunnel. This allowed the ball to be free of any restrictions and able to follow its natural flight path. Some ball types, for instance the smooth sphere, shows a lower C_d (0.05) in the lower Reynolds number than previous work.

Drag curves were found for eight different types of balls. Balls like the smooth sphere, golf ball, and MLB baseball showed the clearest drag crisis. As stitch height increased, drag increased. Orientation and rotation of the ball reduced the drag crisis. Balls, such as the NCAA and cricket, showed a clear drag crisis in only some stitch orientations. Other balls showed a muted drag crisis. Parallel orientations projected with no rotation of the NCAA, MLB, 12 inch softball, and cricket balls had minimum drag coefficients in the drag crisis of approximately 0.3, 0.26, 0.25, 0.26 respectively. These minimum drag coefficients occurred between 60 and 70 mph for the cricket ball and softball, and occurred between 80 - 90 mph for the baseballs.

Lift trends were similar among three types of baseballs with the greatest lift being on the balls with the highest stitches. Orientation and stitch height increased lift and scatter. Overall, higher lift was observed compared to previous work.

Scatter in both lift and drag was greater for stitched balls than smooth or dimpled balls. Lift and drag were shown to be sensitive to seam height and orientation which is difficult to control experimentally. This observed sensitivity may give explanation to the differences in lift and drag data found in literature.

Section 5.2 – Future work

To reveal how lift changes with surface roughness or surface protrusions, such as baseball stitches, different types of balls need to be tested such as the flat and raised seam softball and the smooth sphere. Comparing the raised seam balls to the smooth would reveal how the Magnus effect changes with surface roughness.

Experimental drag data presented here was conducted through the velocity range of 35 mph to 135 mph. Most ball drag crises occurred in this velocity range. However, it

was not clear that the drag crisis had reached its minimum value for the smooth sphere. Previous work show smooth spheres reaching the bottom of the drag crisis around $Re=300,000$, which correlates to approximately 175 mph for the smooth sphere used here. Projecting the smooth sphere at higher velocities is necessary to clearly find the minimum drag in the drag crisis.

Drag was measured on a rotating ball. It was clear that the dimpled pitching machine ball increased drag with increasing rotation. The baseball showed some scatter at low values of S mainly because in that range the ball is going through a drag crisis. In the future a plot of drag verses S with lines of constant velocity would be more convincing that drag increases with rotation. These plots could be compared to constant angular velocity plots to further prove drag does increase with rotation.

Finally, a more and accurate numerical model would be invaluable. Seam orientations and various sports ball flight scenarios could be tested without a cumbersome experiment. As discovered here, numerically modeling turbulence and flow separation is a challenge for expert CFD programs and engineers and improvements need to be made.

List of References

1. **Watson, Russell.** Evolution of Baseball Equipment and the Game . *Ezine @rticles* . [Online] March 31, 2009. [Cited: April 19, 2010.] <http://ezinearticles.com/?Evolution-of-Baseball-Equipment-and-the-Game&id=2164732>.
2. **Johnson, Ted.** The History of the Baseball. *Fogdog Sports*. [Online] [Cited: February 2, 2010.] <http://www.fogdog.com/fog-the-history-of-the-baseball--bg-527303.html#about>.
3. **Adair, Robert K.** *The Physics of Baseball*. New York : Harper Collins Pulishers Inc., 2002.
4. **Crowe, Clayton T., Elger, Donald F. and Roberson, John A.** *Engineering Fluid Mechanics*. Hoboken : Wiley & Sons, 2005.
5. **Prandtl, Ludwig.** *Essentials of fluid dynamics*. New York : Hafner Publishing Company, 1952.
6. **Fay, James A. and Sonwalker, Nishikant.** *Turbulent Flat Plate Boundary Layer*. s.l. : The MIT Press, 1996. 0262561034.
7. **Panton, R.L.** *Incompressible Flow 3rd ed*. Hoboken : John Wiley, 2005.
8. *On the Deviation of Projectiles; and on a remarkable Phenomenon of Rotating Bodies.* **Magnus, G.** Article VII, Berlin : Memoirs of the Royal Academy,, 1852, Vols. pp 210-31.
9. *Aerodynamics of a spinning sphere.* **Maccoll, J.** s.l. : Journal of the Royal Aeronautical Society, 1928, Vol. 32.
10. *The Aerodynamics of Golf Balls.* **Davies, John M.** 9, Akron : Journal of Applied Physics, 1949, Vol. 20.

11. *Effect of Spin and Speed on the Lateral Deflection (Curve) of a Baseball; and the Magnus Effect for Smooth Spheres.* **Briggs, L. J.** Washington D.C : Nationl Bureau of Standards, 1959.
12. *Experiments on the flow past spheres at very high Reynolds numbers.* **Achenbach, Elmar.** part 3, Julich : Journal of Fluid Mechanics, 1972, Vol. 54.
13. *Weitere Foststellungen uber die Besetze des Flussigkeits- und Luftwidersatandes.* **Wieselsberger, C.** s.l. : Phys. Z., 1922, Vol. 23.
14. *Experiments on the flow around a sphere at high reynolds numbers.* **Maxworthy, T.** Los Angeles : Journal of Applied Mechanics, 1969, Vol. 36.
15. *The effect of turbulence: An investigation of maximum lift coefficient and turbulence in wind tunnels and in flight.* **Millikan, C. B. and Klein, A. L.** 8, s.l. : Aircraft Engineering, 1933, Vol. 5.
16. *Aerodynamics of a knuckleball.* **Watts, Robert G. and Sawyer, Eric.** 11, New Orleans : American Journal of Physics, 1974, Vol. 43.
17. *Golf Ball Aeordynamics.* **Bearman, P. W. and Harvey, J. K.** s.l. : Aeronautical Quarterly, 1976, Vol. May.
18. *The lateral force on a spinning sphere: Aeordynamics of a curveball.* **Watts, Robert G. and Ferrer, Ricardo.** 1, New Orleans : American Journal of Physics, 1987, Vol. 55.
19. **Alaways, LeRoy W.** Aeordynamics of a Curve-ball: The Sikorsky/Lightfoot Lift Data. *The Engineering of Sport* 7. 7, 2008, Vol. 2.
20. *Identification of Release Conditions and Aerodynamic Foces in Pitched Baseball Trajectories.* **Alaways, L.W., Mish, S P and Hubbard, M.** s.l. : Journal of Applied Biomechanics, 2001, Vols. 17 pp 63-76.

21. **Alaways, L.W.** *Aerodynamics of the curve ball: An investigation of the effects of angular velocity on baseball trajectories.* . Davis : Unpublished doctoral thesis, 1998.
22. *Sports ball aerodynamics: Effects of velocity, spin, and surface roughness.* **Mehta, R. D. and Pallis, J. D.** Warrendale : Materials and Science in Sports, 2001.
23. *The effect of spin on the flight of a baseball.* **Nathan, A.M.** 2 pp 119-24, University of Illinois : American Journal of Physics, 2009, Vol. 76.
24. *How to hit home runs: Optimum baseball bat swing parameters for maximum range trajectories.* **Sawicki, Gregory S., Hubbard, Mont and Stronge, William J.** 11, Davis : American Journal of Physics, 2003, Vol. 71.
25. *Direction of spin axis and spin rate of the pitched baseball.* **Jinji, T. and Sakurai, S.** s.l. : Sports Biomechanics, 2006, Vol. 5.
26. **Nathan, Alan.** Analysis of PITCHf/x Pitched Baseball Trajectories. *The Physics of Baseball.* [Online] December 9, 2007. [Cited: September 1, 2009.]
<http://webusers.npl.illinois.edu/~a-nathan/pob/Analysis>.
27. **Nathan, Alan M.** The Sportvision Pitch Tracking System (PITCHf/x), How does it work? *Tracking Baseball Pitches Using Video Technology*:. [Online] August 3, 2007. [Cited: February 19, 2010.] <http://webusers.npl.illinois.edu/~a-nathan/pob/technology.htm>.
28. *Aeodynamic drag crisis and its possible effect on the flight of baseballs.* **Frohlich, Cliff.** 4, Austin : American Journal of Physics, 1983, Vol. 54.
29. *Numerical study of the movement of the knuckleball with rifle spin.* **Denbo, Kanako and Kawamura, Tetuya.** 2, s.l. : Natural Science Report, 2005, Vol. 56.

30. *Numerical investigations of flow over a sphere in the subcritical and supercritical regimes.* **Constantinescu, George and Squires, Kyle.** 5, Iowa City : Physics of Fluids, 2004, Vol. 16.
31. **Ansys.** Ansys Fluent 12.0 Theory Guide - 4.4.3 Realizable - Model.
www.fluentusers.com. [Online] Ansys, January 23, 2009. [Cited: April 9, 2010.]
<http://www.fluentusers.com/fluent/doc/ori/v121/fluent/fluent12.1/help/html/th/node60.htm>.
32. **Knight, R. D.** *Physics for Scientists and Engineers.* Boston : Pearson Education, 2007. Vol. Volume 1.
33. **Dickson, Paul.** *The Worth Book of Softball.* New York : Donnelley & Sons, Inc., 1994.
34. *Standard Test Method for Measuring Softball Bat Performance Factor.*
International, ASTM. West Conshohocken : Annual Book of ASTM Standards, 2003, Vol. 15.07.
35. *Standard Test Methods for Measuring High Speed Baseball Bat Performance Factor.*
International, ASTM. West Conshohocken : Annual Book of ASTM Standards, 1998, Vol. 15.07.
36. **Kays, William, Crawford, Michael and Weigand, Bernhard.** *Convective Heat and Mass Transfer, Fourth Edition.* New York : McGraw-Hill, 2005. 0-07-299073-2.
37. **Drury, J.** *The Hell It Don't Curve.* New York : Simon and Shuster, 1956.
38. *How to hit home runs: Optimum baseball bat swing parameters for maximum range trajectories.* **Sawicki, Gregory S., Hubbard, Mont and William, Stronge J.** 11, Cambridge : American Journal of Physics, 2003, Vol. 71.

Appendix One

Experimental procedure for taking samples with the pneumatic cannon was as follows:

- A LabVIEW program was used to run the light gates.
- At the beginning of each series of shots or projections, temperature and humidity were recorded.
- The relative height between the two light boxes and horizontal distance between them was entered into LabVIEW.
- The cannon and high speed camera were run on two separate computers. The light gasted used LabVIEW program called drag.vi and the cannon used a LabVIEW program called cannon.vi.
- The camera was set to automatically trigger once the cannon fired and captured 70 -100 frames of video. The camera would only record 2 ft of the ball's trajectory as the ball was leaving the end of the cannon.
- The ball was loaded into the sabot with a specific orientation and inserted into the breech of the cannon.
- The sabot and ball were fired and only the ball passed through the light boxes.
- The velocities and vertical displacements of the ball in the light gates were recorded to a text file automatically.

The procedure for taking samples with the three wheeled pitching machines was as follows:

- A LabVIEW program called Drag.vi (see Figure A1.1) was used to run the light gates.
- At the beginning of each series of shots or projections, temperature and humidity were recorded using a digital thermometer and humidistat.
- The relative height between the two light boxes and horizontal distance between them was entered into LabVIEW.
- The horizontal distance between the first light box and the exit point of the three wheeled pitching machine was recorded. This was done by fixing a ball in between the three wheels and measuring the horizontal distance between the ball and the first light gate.
- The vertical height of the ball in the pitching machine were recorded. This was done. This was obtained by fixing the ball in between the three wheels. Then a laser level was raised inside the first light box such that the laser beam shone on the center of the ball (see Figure A1.2). A scale was used to measure the height of this beam relative to the bottom of the light box.
- Once measurements were taken the machine was turned on. Rotational speeds of the wheels were adjusted by turning each wheel's potentiometer.
- A ball was placed in the correct orientation into the hopper and then released by removing the stop pin. The ball rolled five inches before being grabbed by the three wheels.
- The video was triggered manually. 7 – 10 frames were saved and used later in tracking software to obtain an angular velocity of the ball for each shot.

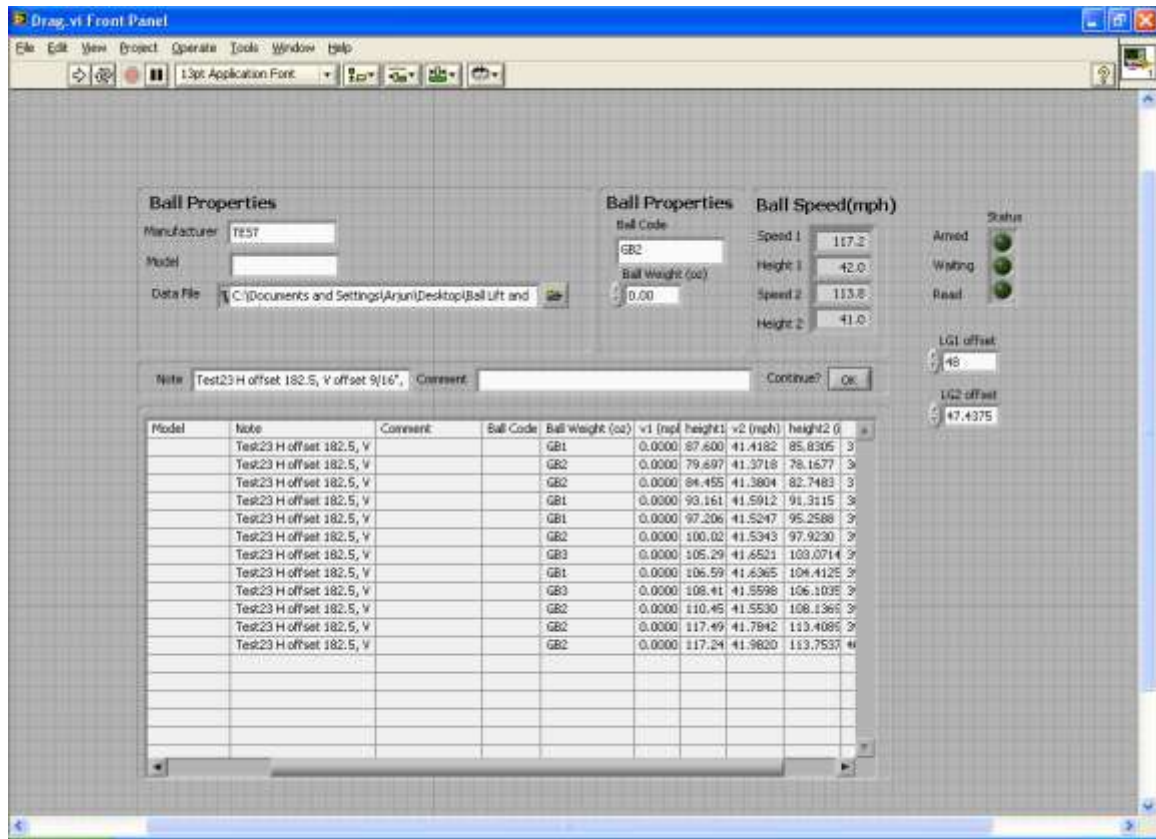


Figure A1.1 - Screen shot of Drag.vi



Figure A1.2 - Obtaining the relative vertical height between the first light box and the ball exit point of the pitching machine.